E-ISSN: 2687 – 6167
NUMBER 48
MARCH 2022

JSR A

JOURNAL OF SCIENTIFIC REPORTS A

JOURNAL OF SCIENTIFIC REPORTS A - MARCH 2022 - NUMBER 48

Kutahya Dumlupinar University Scientific Reports A
Evliya Celebi Campus Tavsanli Road 10 KM. 43270 Kutahya
Phone : 0274 443 18 12
E-mail : joursra@gmail.com
gsjsra.com

Dumlupinar University Press

gate of science

Kütahya Dumlupınar University
Institute of Graduate Studies

Journal of Scientific
Reports-A
E-ISSN: 2687-6167
Number 48, March 2022

Journal of Scientific Reports-A started its publication life in 2000 as name of Journal of Science and Technology of Dumlupınar University and is a national peer-reviewed journal published regularly twice a year in June and December. The language of the journal is English. Articles submitted to the journal are evaluated by at least two referees who are experts in the subject and selected by the editorial board. All articles submitted to the journal are evaluated by the double-blind method. Articles submitted to our journal for review should not be previously published, accepted for publication and in the process of being evaluated for publication in another journal. All responsibility for the articles published in the journal belongs to the author(s).

The journal aims to share scientific studies carried out in the fields of science and engineering at national and international level with scientists and the public. Original research articles, review articles and short notes in science and engineering disciplines are accepted for the journal. Original research articles are expected to contain theoretical and experimental results and should not be published in other journals. In the review articles, it is expected that scientific, technological and current developments on a specific subject are reflected by using an extensive bibliography and made a satisfying evaluation of these. Short notes should be brief writings prepared to announce the first findings of an original study.

Editorial Policy

The journal is open access and the article evaluation period is between 1-2 months.

Correspondence Address: Kütahya Dumlupınar Üniversitesi Evliya Çelebi Yerleşkesi Fen Bilimleri Enstitüsü 43270 KÜTAHYA
Phone: 0 274 443 19 42 **Fax:** 0 274 265 20 60
E-mail: joursra@gmail.com **Webpage:** gsjsra.com

JSR A
Journal of Scientific Reports

JSR A
Journal of Scientific Reports

JSR A
Journal of Scientific Reports

JOURNAL OF SCIENTIFIC REPORTS-A
E-ISSN: 2687-6167

CONTENTS

RESEARCH ARTICLES

REWIEV ARTICLES

Kütahya Dumlupınar University
Institute of Graduate Studies

Journal of Scientific
Reports-A
E-ISSN: 2687-6167
Number 48, March 2022

RESEARCH ARTICLE

MIXTURES of PHARMACEUTICALS and PERSONAL CARE PRODUCTS (PPCPs) EFFECT PLANT STRESS MARKERS and NUTRIENT UPTAKE in WHEAT and BARLEY

Müjgan ELVEREN[1*], Etem OSMA[2]

[1]Erzincan Binali Yıldırım University, Vocational School of Health Services, Medical Services and Techniques, mujgan.elveren@erzincan.edu.tr, ORCID: 0000-0002-6110-8088
[2]Erzincan Binali Yıldırım University, Faculty of Science and Arts, Department of Biology, eosma@erzincan.edu.tr, ORCID: 0000-0002-5250-8194

Received Date:06.01.2021 *Accepted Date:02.03.2022*

ABSTRACT

Common drug active substances (gemfibrozil, β-estradiol, caffeine, and ciprofloxacin) were combined in simple mixtures and applied to soil containing wheat or barley. Mixtures in water (50 µg/mL) were applied twice during the growing period. Harvested plant samples were extracted and antioxidant enzyme activities, as indicated by CAT, POD, and SOD were compared in exposed and control plants. Lipid peroxidation markers were also determined. Finally, mineral element uptake in exposed and control plants was determined. The data indicated differences in several, if not all, of the plant biomarkers between control plants and those treated with simple mixtures of pharmaceutical substances; many were directly related to oxidative damage. It was determined that there were statistically significant differences in the element intake of 8 nutrients (magnesium, potassium, phosphorus, calcium, zinc, mangan, copper, and iron) in control plants compared with plants treated with PPCPs; we observed both increases and decreases in plant nutrients depending on the particular nutrient, pharmaceutical treatment, and plant species.

Kewwords: *Antioxidant Enzymes, Barley, Mineral Element, PPCPs, Wheat*

1. INTRODUCTION

Besides the numerous different chemicals produced today, an increase in population leads to increased consumption of chemicals such as pharmaceuticals and personal care products (PPCPs) [1,2]. It has been estimated that the consumption antibiotics is 100,000 – 200,000 tons on a global scale; almost 15,000 tons of antibiotics are released in Europe each year [3]. According to data from Turkey, pharmaceutical use increased 1.4 fold from 2010 to 2016 (1.62 billion units to 2.23 billion units). In addition, in 2016, about 440 new pharmaceuticals were released to the market worldwide [4]. Antibiotics, antimicrobials, painkillers, allergy medicines, caffeine etc. are just a few of the substances that make up PPCPs.

PPCPs have recently been shown to be among the most common contaminants in the environment [3]. The entry of pharmaceutical substances into an ecosystem can occur in many ways. PPCP waste, sewage sludge, pharmaceutical producers, food companies, and fish farms are some of the sources of PPCPs into the environment. The cycle begins with animal (including human) use, entrance into the

wastewater treatment system, discharge to surface water or water re-use, and eventually to compartments where exposure occurs. Research has shown that many PPCPs are excreted from humans without metabolism [1,2]. In addition, these micro-pollutants can often interfere with sewage treatment systems and be relatively resistant to degradation at wastewater treatment plants [2,5]. Pollution of the environment from PPCPs is an important problem and can have a negative impact on living organisms. Increased water shortages due to population growth, urbanization, and the climate change has brought about interest in the recycling of treated wastewater, particularly in many arid and semi-arid regions of the world. Today, in many countries, treated wastewater is applied to land for agricultural irrigation [6].

The potential impact of PPCPs in recycled water on soil processes and plants has not been fully described. The potential for biological degradation of these micro-pollutants or their interactions with each other is largely unknown. Studies conducted to date indicate that plants can uptake some PPCPs; the transport of PPCPs in the environment depends on their physical properties such as volatility, lipophilicity water solubility, and sorption potential. In addition, -properties of the soil are also important [7-10]. Several studies have shown that plants are affected by exposure to PPCPs; effects include impact on photosynthetic pigments, number and size of leaves, inhibition of root growth and development, and physiological functions. Any negative impact on plants may also have an effect on soil microorganisms, particularly those in the root zone or rhizosphere. This is a potential concern for the symbiotic relationship between plants and microorganisms and for nutrient cycling in the soil. Although not all PPCPs and plants have been evaluated, it appears that most PPCPs don't induce phytotoxic effects. PPCPs may be metabolized, detoxified, inactivated, and sequestered following uptake by plant roots. However, recent studies have shown that oxidative activities triggered by ROS overproduction are a potential adverse impact of PPCP exposure to plants; oxidative damage can be the phytotoxic response from prolonged exposure to pharmaceutical substances [11,12]. Generally, the potential effects of PPCPs on plants can be evaluated by monitoring ROS production and subsequent oxidative damage Osma et al. 2018 [13]; the responses of plants can vary according to plant species. Recent studies indicate that the impacts of individual PPCPs manifests at relatively high exposure concentrations. Plant responses can serve as a monitoring tool for evaluating the presence of PPCPs [3,14-17].

Data on the possible negative impacts to plants of PPCP mixtures are scarce. The types of interactions (additive, synergistic, or antagonistic) that PPCPs might have, even for relatively simple mixtures is in need of further evaluation. Our goal with this research was to determine the effects of simple (binary) mixtures of PPCPs on plant stress markers.

2. MATERIAL AND METHODS

In this study, simple mixtures of four medicinal active substances (gemfibrozil, β-estradiol, caffeine, and ciprofloxacin) were evaluated for impacts on wheat (*Triticum aestivum* L.) and barley (*Hordeum vulgare* L.). The cultivation process was carried out in the laboratory according to methods described by [13]. Briefly, for sowing, 5 g of barley and 7 g of wheat seeds were planted in 650 g of soil and covered with an additional 100 g of soil. Based on the field capacity, soil samples were moistened with deionized water. After germination of wheat and barley seeds, gemfibrozil and estradiol, gemfibrozil and caffeine, or gemfibrozil and ciprofloxacin mixtures (50 µg/mL) were applied twice during the experiment. Wheat was harvested at the end of 15 days growth; barley at the end of 11

days. Biomass of wheat and barley plants were determined gravimetrically. A portion of the plant samples was assigned for use in subsequent physiological and biochemical investigations.

Malondialdehyde is one of the peroxidation products of polyunsaturated fatty acids formed by the increase of free radicals. The amount of malondialdehyde (MDA) was measured using thiobarbituric acid (TBA) method with slight modifications [18]. Leaf samples were weighed approximately 0.5 g/each and homogenized by adding 5% trichloroacetic acid (TCA). The leaf homogenates were then centrifuged at 15,000 x g for 15 minute at 4 °C. To each 1 mL aliquot of the supernatant, 2 mL TBA reagent (0.5 % TBA in 20% TCA, w/v) was added. 1 mL of 0.1 % TCA and 2 mL TBA reagent were combined as a negative control. Test and negative control tubes were heated at 95 °C for 30 min and were then rapidly cooled in an ice bath. Chilled tubes were centrifuged at 15,000 xg for 15 minute at 4 °C. Following centrifugation the absorbance of the supernatant at 532 was determined. The absorbance of non-specific molecules is read at 600 nm and was subtracted from absorbance of samples. MDA amount was determined by its molar extinction coefficient at 532 nm (155 mmol/L^{-1}·cm^{-1}) [13].

First, 0.1 g of fresh plant sample harvested from plant leaves was put in each of 12 test tubes. 4 mL of distilled water was added into the tubes and kept at 4 °C for 24 h. Then, amounts of ions in distilled water from the samples collected to detect the damage to cells were measured by electrical conductivity meter [13, 19].

After 0.5 g tissue were weighed and put into the porcelain mortar, 5 mL of cold homogenate buffer was added to it (0.1 M KH_2PO_4 at pH 7.0 containing 1 % PVP and 1 mM EDTA). The mixture was transferred into a centrifuge tube and centrifuged at 15000 × g and at 4 °C for 15 min. Supernatant antioxidant obtained from centrifugation was used as a source for enzyme activity deaths [13]. Whether the plants were under stress physiologically was determined by measuring antioxidant enzyme (superoxide dismutase, catalase, peroxidase) activities through the increases in types of reactive oxygen species during watering and soil stress conditions. Chemicals and methods used for each antioxidant enzyme were different [13]. The method used for the specification of Catalase (CAT) activity was the method that of Havir and McHale (1987). Activity measurement with this method is based on the principle whereby a decrease in absorbance in a CAT activity measurement environment while H_2O_2 is converted into O_2 and H_2O is observed at 240 nm [13, 20]. In order to determine catalase activities in the extraction solution obtained from plant samples, 5 mM H_2O_2 solution was used. After 103.5 mM of KH_2PO_4 buffer and 40 mM of H_2O_2 substrate solution are mixed and put into 3 mL quartz vials, 20 µL of enzyme extract from leaves and 50 µL of enzyme extract from roots were added. After the vial was placed into the spectrophotometer, its absorbance against a blank was monitored at 240 nm for 3 min at 1 min intervals. Absorbance per minute from the point where absorbance decreased linearly was calculated. These average absorbance values were converted into µmol H_2O_2 through a standard curve. The amount of enzyme that decreased absorbance 1 µmol at 25 °C in 1 min was accepted as one enzyme unit, and the results are presented as enzyme units per gram of tissue (EU g^{-1} tissue) [13,20]. Plant leaves (0.5 g) were blended with 10 mM potassium phosphate buffer (pH = 7.0) which contains 4% (w/v) polyvinylpyrrolidone. The homogenized pulp was centrifuged at 12,000 x g for 30 minutes at 4° C. Then the extract was isolated to determine the type of enzyme. After adding the plant extract to 50 mM phosphate buffer (pH = 7.0) which contains 1 mM guaiacol and 0.5 mM H_2O_2, peroxidase (POX) was determined by monitoring the increase in absorbance at 470 nm. One unit of POX activity was defined as the amount of enzyme that caused an increase in absorbance of 0.01 per min [13,21].

Activity determination of superoxide dismutase (SOD) was performed using spectrophotometry based on the photochemical reduction of nitro blue tetrazolium (NBT) inhibition [13]. The composition of reaction mixture contained following concentrations: 50 mM sodium carbonate, 13 mM methionine, 2 µM riboflavin, 75 µM NBT, 50 mM phosphate buffer (pH = 7.8), 0.1 mM EDTA, and 0.1 mL of plant extract. The measurements for the mixture at 560 nm absorbance were realized thereafter preparation. As control and blank, a maximum color-producing reaction mixture having no enzyme and a non-irradiated complete reaction mixture were utilized, respectively. The activity as one unit in the tubes was measured in terms of reducing the absorbance by 50% compared to the tubes having no enzyme; hence, the determinations of the values were in EU g^{-1} tissue quantities [13].

At harvest, samples were collected by hand and packed into polyethylene bags. Only the shoots of each plant were analyzed. Plants were oven dried at 80 °C for 24 h. Plant samples were milled with a micro-hammer cutter, sieved through a 1.5-mm sieve, and transferred to a clean polyethylene bag. After each milling, the mortar was cleaned with ethyl alcohol and distilled water to prevent cross-contamination of samples [22,23]. The conditions for the samples subjected to digestion were as defined: the maximum power applied was 1200 W; the ramp setting was for 20 min.; the pressure used was 180 PSI; the temperature setting was 210° C; and the hold time applied was 10 min. Following digestion, the solutions were evaporated to near dryness in a beaker. After evaporation, the volume adjustments for the remaining material samples were done to 10 mL using 0.1 M HNO3. The Varian Inductively Coupled Plasma–Optical Emission Spectrometry (ICP–OES) was employed for the determinations of elements in the all samples [22,23].

Analysis of Variance (ANOVA) in SPSS 22 was used to determine treatment effects relative to control (untreated) plants. S-N-K ve Tukey's B were performed when significant treatment effects were observed. For all statistical analyses, a p value ≤ 0.05 was determined as being significant [23].

3. RESULTS AND DISCUSSION

The potential impacts of binary mixtures (gemfibrozil and estradiol, gemfibrozil and caffeine, and gemfibrozil and ciprofloxacin) on possible plant stress markers in wheat and barley were investigated. The data indicated differences in several, if not all, of the plant biomarkers between control plants and those treated with simple mixtures of pharmaceutical substances. Many of the plant biomarkers we evaluated were directly related to oxidative damage.

JSR A
Journal of Scientific Reports

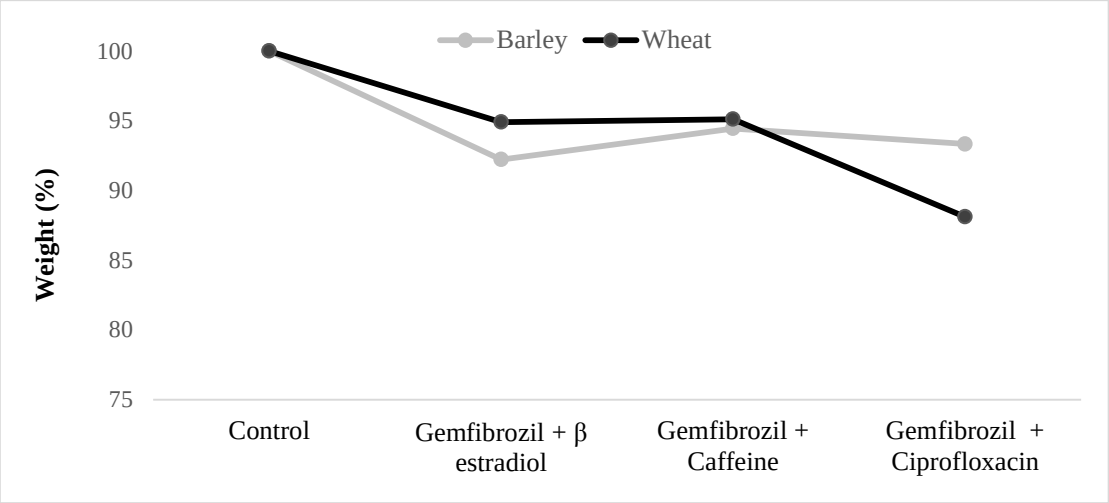

Figure 1. The leaf weights in wheat and barley treated with mixture PPCPs.

We observed slight decreases in plant biomass in both wheat and barley plants treated with the binary mixtures compared to control plants. However, the decrease in plant biomass was only significant for the gemfibrozil + ciprofloxacin treatment (Fig. 1).

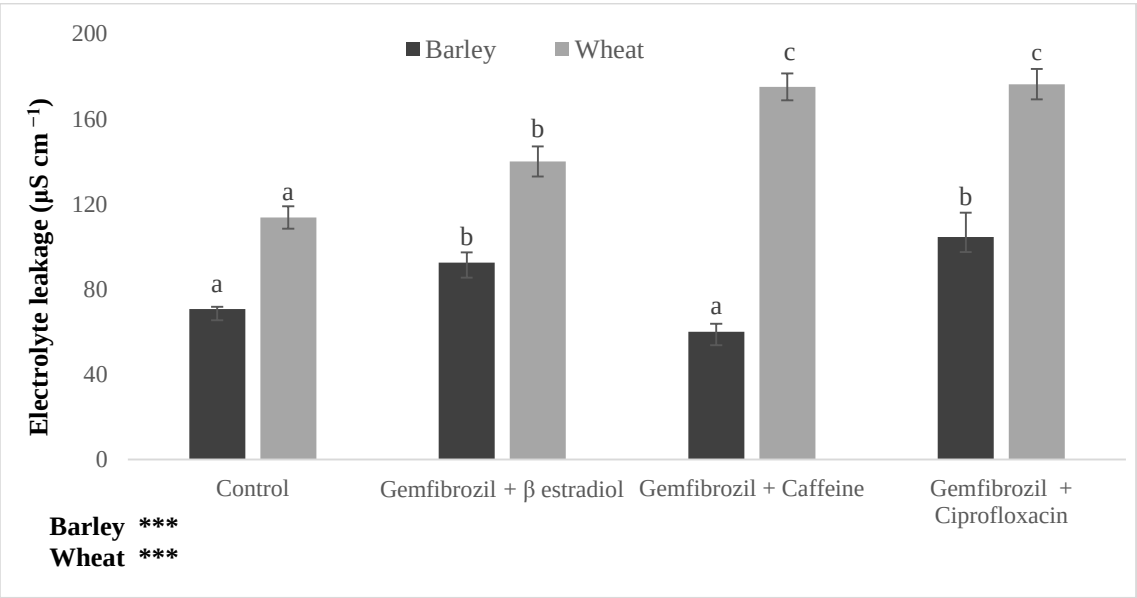

Figure 2. Electrolyte leakage concentrations in wheat and barley growth with mixture PPCPs. (*p<0,05; **p<0,01; ***p<0,001 significant).

JSR A
Journal of Scientific Reports

Average electrolyte leakage (mean ± standard error) was 71 ± 1.1 $\mu S \cdot cm^{-1}$ in control samples of barley. The highest electrolyte leakage in barley occurred in the gemfibrozil + ciprofloxacin treatment (104 ± 11 $\mu S \cdot cm^{-1}$). Control samples of wheat had an average electrolyte leakage of 114 ± 5.2 $\mu S \cdot cm^{-1}$ while gemfibrozil, in combination with either caffeine (175 ± 6.3 $\mu S \cdot cm^{-1}$) or ciprofloxacin (176 ± 5.2 $\mu S \cdot cm^{-1}$), produced the highest electrolyte leakage in wheat. Following statistical analysis of the electrolyte leakage data, it was concluded that there was a significant treatment effect of the binary mixtures in both barley and wheat (Figure 2).

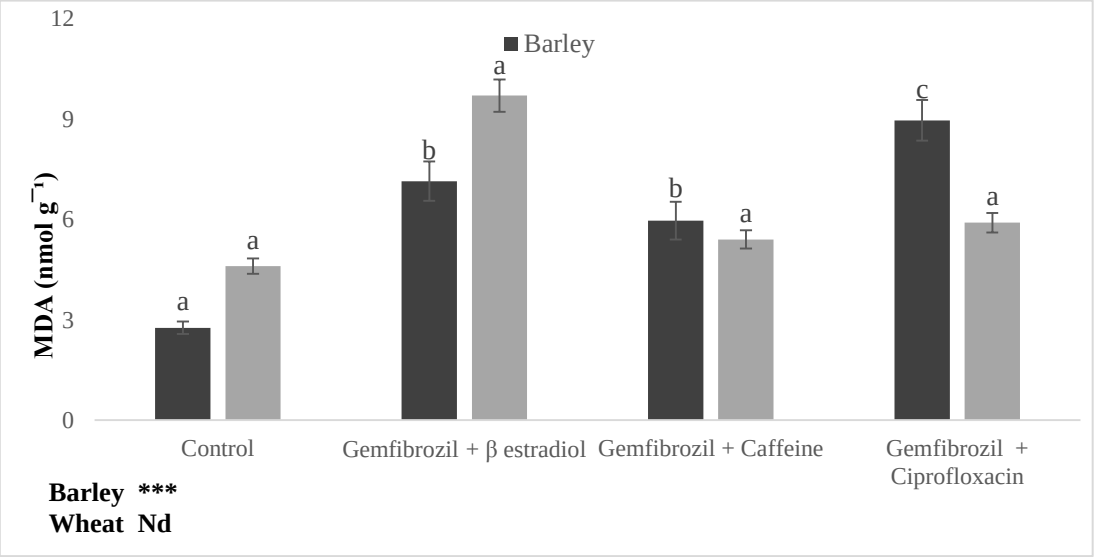

Figure 3. MDA concentrations in wheat and barley growth with mixture PPCPs.. (*p<0,05; **p<0,01; ***p<0,001 significant).

MDA levels were elevated in treated plants (both species), however, the treatment effect was only statistically significant for barley (Fig. 3). MDA was 2.8 ± 0.2 mmol/g in control samples of barley. The highest MDA levels in barley occurred in the gemfibrozil + ciprofloxacin treatment (9.0 ± 0.6 mmol/g). Control samples of wheat had an average MDA level of 4.6 ± 0.9 mmol/g, while the gemfibrozil + β-estradiol treatment produced the highest MDA levels in wheat (9.7 ± 2.0 mmol/g).

JSR A
Journal of Scientific Reports

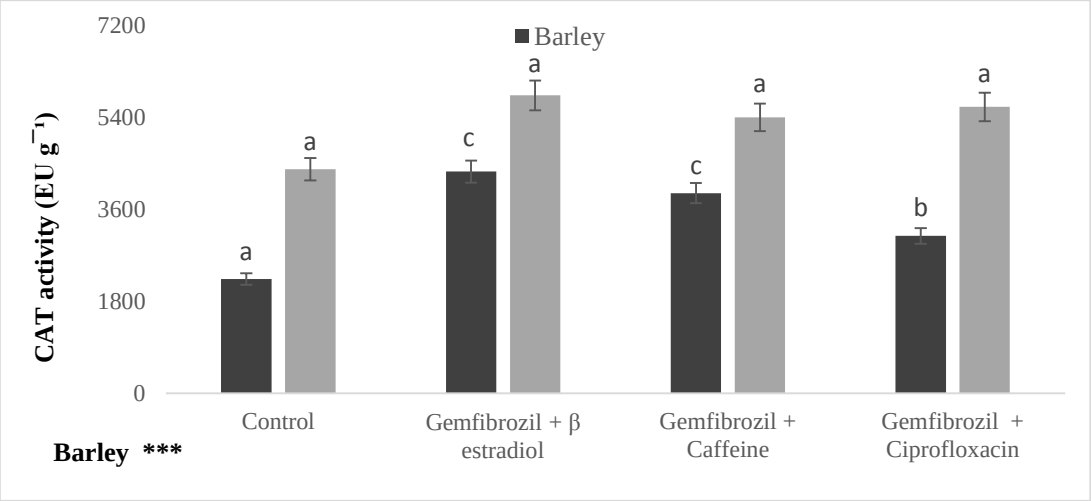

Figure 4. CAT activities in wheat and barley growth with mixture PPCPs. (*p<0,05; **p<0,01; ***p<0,001 significant).

When catalase (CAT) enzyme activity was examined in barley and wheat plants, there were significant treatment effects between the control samples and samples treated with pharmaceutical mixtures (Fig. 4). CAT activity in control barley plants was 2236 ± 145 EU/g, while treated plants had CAT activities ≥ 3082 EU/g. CAT activity in control wheat plants was 4397 ± 498 EU/g, while treated plants had CAT activities ≥ 5406 EU/g. For both plant species, the gemfibrozil + estradiol treatment produced the largest increase in CAT activity compared to control (untreated) plants.

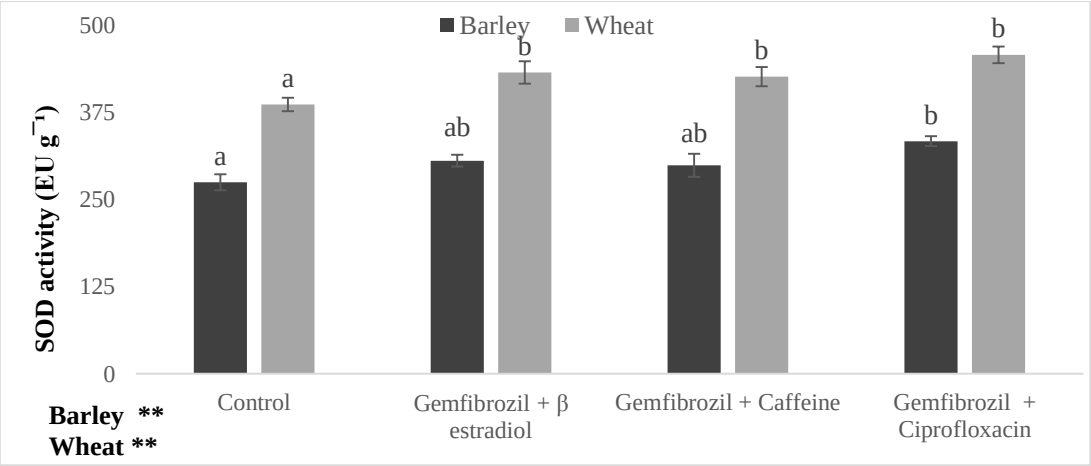

Figure 5. SOD activities in wheat and barley growth with mixture PPCPs. (*p<0,05; **p<0,01; ***p<0,001 significant).

When superoxide dismutase (SOD) enzyme activity was examined, a slight increase was observed in barley and wheat plants treated with pharmaceutical mixtures versus control (untreated) plants (Fig.

5). SOD enzyme activity was 275 ± 12 and 386 ± 9.7 EU/g in control barley and wheat samples, respectively. The treatment of gemfibrozil + ciprofloxacin produced the highest increase in SOD activity over controls for both plant species (333 ± 7.1 EU/g for barley and 458 ± 12 EU/g for wheat).

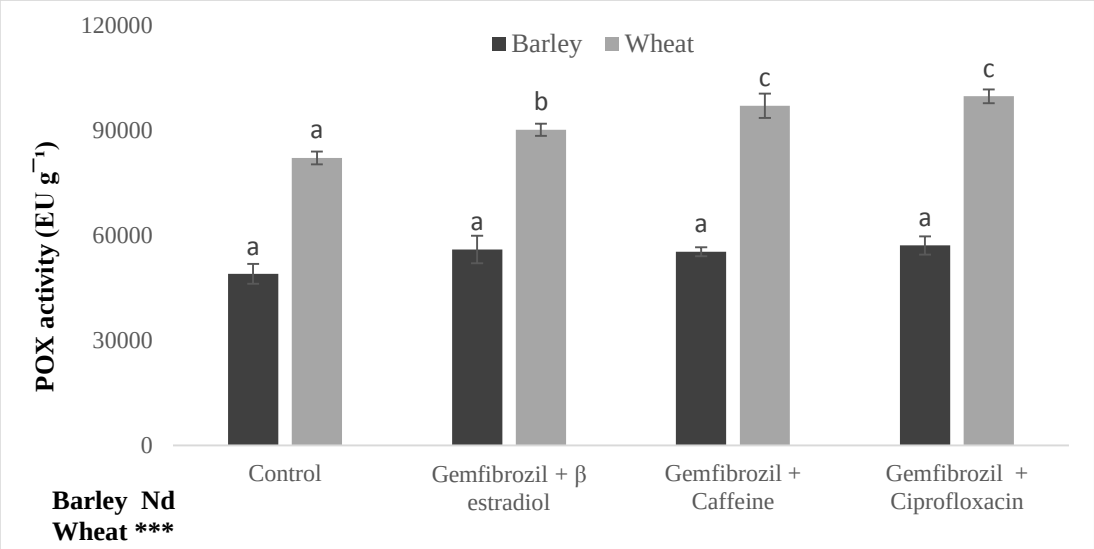

Figure 6. POX activities in wheat and barley growth with mixture PPCPs. (*p<0,05; **p<0,01; ***p<0,001 significant).

Peroxidase (POX) activity in barley was in the range of 48,936 ± 2824 EU/g (control) to 57,063 ± 2656 EU/g (gemfibrozil + ciprofloxacin). The gemfibrozil + ciprofloxacin had a similar effect on wheat (82,036 ± 1814 EU/g in controls and 100,750 + 1956 EU/g in treatment plants) (Fig. 6). When these differences were examined statistically, the slight increase in POX with treatment was not significant in barley, however, there was a treatment effect on POX for wheat plants.

Minerals are essential in the growth and development of all living organisms. Living organisms take up the elements necessary through the cycle of matter. It was determined that there were statistically significant differences in the element intake of 8 nutrients including Mg, K, P, Ca, Zn, Mn, Cu, and Fe in control plants compared with plants (both species) treated with pharmaceutical active substances (Table 1). We observed both increases and decreases in plant nutrients depending on the particular nutrient, pharmaceutical treatment, and plant species. Our data indicate that there are changes in electrolyte leakage and the activities of peroxidase, catalase and superoxide dismutase enzymes in both barley and wheat plants exposed to simple mixtures of pharmaceuticals. For both barley and wheat and for many of the plant biomarkers examined, exposure to gemfibrozil + ciprofloxacin produced the most dramatic and statistically significant effects on plants compared to control (untreated) plants.

There are many research reports that indicating that plants accumulate PPCPs [3,24-26]. However, research on the biochemical/physiological effects of PPCPs on plants is relatively new, especially mixtures of PPCPs. Dodgen et al. [27] applied individual PPCPs (bisphenol A, diclofenac, naproxen, nonylphenol) to cabbage and lettuce. They established that there was more accumulation in roots than

in leaves or stems. In addition, as the accumulation of PPCPs increased, the negative effects on plant development became more pronounced. An et al. [28] studied the ecotoxicologic effects of paracetamol on germination of wheat. They observed that the development of wheat seeds decreased in a concentration dependent manner. Paracetamol and diclofenac have also been shown to effect peroxidase activity, chlorophyll, and membrane activity of duckweed, *Lemna minor* [29] Chlorophyll and carotenoids in *Lemna gibba* were also negatively impacted by exposure to ibuprofen.[30] PPCP exposure to cucumbers produced a decrease in chlorophyll, but increased levels and activity of antioxidant enzymes in roots and leaves [12]. The authors speculated that the latter effect was a plant defense mechanism.

Our data indicate that there are changes in electrolyte leakage and the activities of peroxidase, catalase and superoxide dismutase enzymes in both barley and wheat plants exposed to simple mixtures of pharmaceuticals. For both barley and wheat and for many of the plant biomarkers examined, exposure to gemfibrozil + ciprofloxacin produced the most dramatic and statistically significant effects on plants compared to control (untreated) plants.

Table 1. Concentration of mineral elements in wheat and barley treated with mixture of PPCPs. (*p<0,05; **p<0,01; ***p<0,001 significant).

Element		**Wheat**			**Significant**	**Barley**			**Significant**
Mg	Control	2102,5	±	132,2		2623,5	±	196,4	
	Gemfibrozil + β estradiol	1863,8	±	53,5		1851,1	±	43,6	
	Gemfibrozil + Caffeine	2019,7	±	89,0		2087,0	±	10,4	
	Gemfibrozil + Ciprofloxacin	1721,6	±	50,0	*	1970,3	±	116,5	***
K	Control	57772,1	±	1011,8		42286,3	±	5361,4	
	Gemfibrozil + β estradiol	57434,8	±	1213,4		34367,9	±	481,0	
	Gemfibrozil + Caffeine	64124,1	±	1045,5		37165,7	±	208,1	
	Gemfibrozil + Ciprofloxacin	58105,0	±	1044,3	***	34423,2	±	1480,0	**nd**
Ca	Control	1154,9	±	128,1		1449,4	±	45,3	
	Gemfibrozil + β estradiol	980,3	±	26,8		894,2	±	16,2	
	Gemfibrozil + Caffeine	951,5	±	18,1		1030,4	±	15,5	
	Gemfibrozil + Ciprofloxacin	884,5	±	27,0	**nd**	926,2	±	42,9	***
P	Control	7662,4	±	267,3		7194,3	±	1090,8	
	Gemfibrozil + β estradiol	7363,6	±	179,2		4347,7	±	35,6	
	Gemfibrozil + Caffeine	8084,5	±	142,7		4616,5	±	17,3	
	Gemfibrozil + Ciprofloxacin	7054,3	±	151,4	*	4524,8	±	90,4	**
Zn	Control	33,8	±	1,0		47,5	±	2,9	
	Gemfibrozil + β estradiol	30,9	±	0,2		46,5	±	1,0	
	Gemfibrozil + Caffeine	29,9	±	0,1		51,2	±	0,6	
	Gemfibrozil + Ciprofloxacin	51,1	±	0,9	***	45,7	±	0,7	**nd**
Mn	Control	30,9	±	1,4		29,5	±	0,1	
	Gemfibrozil + β estradiol	27,3	±	0,5		26,3	±	0,6	
	Gemfibrozil + Caffeine	26,0	±	0,1		25,9	±	0,1	
	Gemfibrozil + Ciprofloxacin	25,1	±	0,3	***	24,5	±	0,4	***

Cu	Control	14,8	± 0,1		13,7	± 0,5	
	Gemfibrozil + β estradiol	14,9	± 0,5		17,1	± 0,2	
	Gemfibrozil + Caffeine	15,7	± 0,3		18,0	± 0,1	
	Gemfibrozil + Ciprofloxacin	15,2	± 0,1	**nd**	17,2	± 0,9	***
Fe	Control	69,1	± 5,2		236,4	± 58,2	
	Gemfibrozil + β estradiol	67,2	± 3,6		60,7	± 0,9	
	Gemfibrozil + Caffeine	69,6	± 1,4		80,4	± 2,2	
	Gemfibrozil + Ciprofloxacin	82,8	± 2,1	*	75,6	± 8,0	***

There are many research reports that indicating that plants accumulate PPCPs [3,24-26]. However, research on the biochemical/physiological effects of PPCPs on plants is relatively new, especially mixtures of PPCPs. Dodgen et al. [27] applied individual PPCPs (naproxen, bisphenol A, nonylphenol, diclofenac) to lettuce and cabbage. They established that there was more accumulation in roots than in leaves or stems. In addition, as the accumulation of PPCPs increased, the negative effects on plant development became more pronounced. An et al. [28] studied the ecotoxicologic effects of paracetamol on germination of wheat. They observed that the development of wheat seeds decreased in a concentration dependent manner. Paracetamol and diclofenac have also been shown to effect peroxidase activity, chlorophyll, and membrane activity of duckweed, *Lemna minor* [29] Chlorophyll and carotenoids in *Lemna gibba* were also negatively impacted by exposure to ibuprofen [30]. PPCPs exposure to cucumbers produced a decrease in chlorophyll, but increased levels and activity of antioxidant enzymes in roots and leaves [12]. The authors speculated that the latter effect was a plant defense mechanism. Christou et al. [31] studied the impact of diclofenac, sulfamethoxazole, trimethoprim, and 17α-ethinylestradiol to clover singly, and then as a mixture, on biochemical/physiological parameters; the mixture had a greater impact than individual PPCPs. A similar observation was made by Geiger et al [32] for algae exposed to a mixture of ibuprofen, ciprofloxacin and chlorophenols, although some of the negative effects of algal development likely came from the chlorophenols.

4. CONCLUSIONS

It appears that based on our data, pharmaceuticals and personal care products in mixtures can cause deleterious impacts to plants which could lead to agronomic costs. When we consider the number of potential combinations of PPCPs present in wastewater (even after treatment), additional consideration should be given to the potential impacts these PPCPs may have as treated wastewater is recycled and used for other purposes. The potential impact that PPCPs taken up by plants irrigated with recycled water could have on living things that feed on these plants is largely unknown. In order to minimize the effects of these substances, which have high polluting potential on the environment, importance should be emphasized to make legal arrangements related to the usage and disposal of drugs and to raise awareness of people as well.

ACKNOWLEDGMENT

This study was supported in part by Erzincan Binali Yıldırım University BAP, FBA-2017-404.

REFERENCES

[1] Daughton, C.G., Ternes, T.A., (1999), Pharmaceuticals and personal care products in the environment: agents of subtle change, Environmental Health Perspectives, 107, 907-938.

[2] Wang, J., Wang, S., (2016), Removal of pharmaceuticals and personal care products (PPCPs) from wastewater: a review, Journal of Environment Management, 182, 620-640.

[3] Bartrons, M, Peñuelas, J., (2017), Pharmaceuticals and personal-care products in plants, Trends in Plant Science, 22(3), 194-203.

[4] Anonymous,(2018), http://www.ieis.org.tr/ieis/assets/media/Raporlar/TR_Sektor_raporu_2016.pdf

[5] Verlicchi, P., Al Aukidy, M., Jelic, A., Petrović, M., Barceló, D., (2014), Comparison of measured and predicted concentrations of selected pharmaceuticals in wastewater and surface water: a case study of a catchment area in the Po Valley (Italy), Science Total Environment, 470-471, 844-854.

[6] Wu, X., Conkle, J.L., Gan, J., (2012), Multi-residue determination of pharmaceutical and personal care products in vegetables, Journal of Chromatography A., 1254, 78-86.

[7] Dolliver, H., Kumar, K., Gupta, S., (2007), Sulfamethazine uptake by plants from manure-amended soil, Journal of Environmental Quality, 36, 1224-1230.

[8] Chitescu, C.L., Nicolau, A.I., Stolker, A.A.M., (2013), Uptake of oxytetracycline, sulfamethoxazole and ketoconazole from fertilised soils by plants, Food Additives & Contaminants: Part A., 30, 1138-1146.

[9] Ahmed, M.B.M., Rajapaksha, A.U., Lim, J.E., Vu, N.T., Kim, I.S., Kang, H.M., Lee, S.S., Ok, Y.S., (2015), Distribution and accumulative pattern of tetracyclines and sulfonamides in edible vegetables of cucumber, tomato, and lettuce, Journal of Agricultural and Food Chemistry, 63, 398-405.

[10] Azanu, D., Mortey, C., Darko, G., Weisser, J.J., Styrishave, B., Abaidoo, R.C., (2016), Uptake of antibiotics from irrigation water by plants, Chemosphere, 157, 107-114.

[11] Mittler, R., (2002), Oxidative stress, antioxidants and stress tolerance, Trends in Plant Science, 7, 405-410.

[12] Sun, C., Dudley, S., Trumble, J., Gan, J., (2018), Pharmaceutical and personal care products-induced stress symptoms and detoxification mechanisms in cucumber plants, Environmental Pollution, 234, 39-47.

[13] Osma, E., Cigir, Y., Karnjanapiboonwong, A., Anderson, T.A., (2018), Evaluation of selected pharmaceuticals on plant stress markers in wheat, International Journal of Environmental Research, 12(2), 179-188.

[14] Winker, M., Clemens, J., Reich, M., Gulyas, H., Otterpohl, R., (2010), Ryegrass uptake of carbamazepine and ibuprofen applied by urine fertilization, Science Total Environment, 408, 1902-1908.

[15] Carvalho, P.N., Basto, M.C.P., Almeida, C.M.R., Brix, H., (2014), A review of plant–pharmaceutical interactions: from uptake and effects in crop plants to phytoremediation in constructed wetlands, Environmental Science and Pollution Research, 21, 11729-11763.

[16] Peñuelas, J., Terradas, J., (2014), The foliar microbiome, Trends in Plant Science, 19, 278-280.

[17] Peñuelas, J., Farré-Armengol, G., Llusia, J., Gargallo-Garriga, A., Rico, L., Sardans, J., Terradas, J., Filella, I., (2014), Removal of floral microbiota reduces floral terpene emissions, Scientific Reports, 4, 6727.

[18] Ananieva, E.A., Alexieva, V.S., Popova, LP., (2002), Treatment with salicylic acid decreases the effects of paraquat on photosynthesis, Journal of Plant Physiology, 159(7), 685-693.

[19] Griffith, M., Ala, P., Yang, D.S.C., Hon, W.C., Moffatt, B.A., (1992), Antifreeze protein produced endogenously in winter rye leaves, Plant Physiology, 100, 593-596.

[20] Türkoğlu, E., Osma, E., Elveren, M., (2019), Effects of acetaminophen (paracetamol) and gemfibrozil on seed development and antioxidant enzyme activities in different wheat varieties, Iranian Journal of Science and Technology, Transactions A: Science, 43, 2075–2082.

[21] Upadhyaya, A., Sankhla, D., Davis, N., Sankhla, N., Smith, B.N., (1985), Effect of paclobutrazol on the activities of some enzymes of activated oxygen metabolism and lipid peroxidation in senescing soybean leaves, Journal of Plant Physiology, 121, 453-461.

[22] Demirezen, D., Aksoy, A., (2006), Heavy metal levels in vegetables in Turkey is within safe limits for Cu, Zn, Ni and exceeded for Cd and Pb, Journal of Food Quality, 29, 252-265.

[23] Osma, E., İlhan, V., Yalçın, İ.E., (2014), Heavy metals accumulation causes toxicological effects in aquatic *Typha domingensis* Pers., Brazilian Journal of Botany, 37(4), 461-467.

[24] Tai, Y., Luo, X., Mo, C., Li, Y., Wu, X., Liu, X., (2011), Occurrence of quinolone and sulfonamide antibiotics in swine and cattle manures from large-scale feeding operations of Guangdong province, Huanjing Kexue, 32, 1188–1193.

[25] Awad, Y.M., Kim, S.C., Abd El-Azeem, S.A.M., Kim, K.H., Kim, K.R., Kim, K., Jeon, C., Lee, S.S., Ok, Y.S., (2014), Veterinary antibiotics contamination in water, sediment, and soil near a swine manure composting facility, Environmental Earth Sciences, 71, 1433–1440.

[26] Sura, S., Degenhardt, D., Cessna, A.J., Larney, F.J., Olson, A.F., McAllister, T.A., (2014), Dissipation of three veterinary antimicrobials in beef cattle feedlot manure stockpiled over winter, Journal of Environmental Quality, 43, 1061–1070.

[27] Dodgen, L.K., Li, J., Parker, D., Gan, J.J., (2013), Uptake and accumulation of four PPCP/EDCs in two leafy vegetables, Environmental Pollution, 182, 150-156.

[28] An, J., Zhoua, Q., Suna, F., Zhanga, L., (2009), Ecotoxicological effects of paracetamol on seed germination and seedling development of wheat (*Triticum aestivum* L.), Journal of Hazardous Materials, 169, 751–757.

[29] Kummerova M, Zezuka S, Babula P, Triska J., (2016), Possible ecologial risk of two pharmaceuticals diclofenac and paracetamol demonstrated on a model plant *Lemma minor*, Journal of Hazardous Materials, 302, 351–361.

[30] Pietrini, F., Baccioa, D.D., Acena,˜ J., Pérez, S., Barceló, D., Zacchini, M., (2015), Ibuprofen exposure in Lemna gibba L.: Evaluation of growth and phytotoxic indicators, detection of ibuprofen and identification of its metabolites in plant and in the medium, Journal of Hazardous Materials, 300, 189–193.

[31] Christou, A., Antoniou, C., Christodoulou, C., Hapeshi, E., Stavrou, J., Michael, C., Fatta-Kassinos, D., Fotopoulos, V., (2016), Stress-related phenomena and detoxification mechanisms induced bycommon pharmaceuticals in alfalfa (*Medicago sativa* L.) plants, Science Total Environment, 557–558, 652–664.

[32] Geiger, E., Hornek-Gausterer, R., Saçan, M.T., (2016), Single and mixture toxicity of pharmaceuticals and chlorophenols to fresh water algae *Chlorella vulgaris*, Ecotoxicology and Environmental Safety, 129, 189–198.

Kütahya Dumlupınar University
Institute of Graduate Studies

Journal of Scientific
Reports-A
E-ISSN: 2687-6167
Number 48, March 2022

RESEARCH ARTICLE

OPTIMIZATION of MICROBIAL CONSORTIA in the DEGRADATION of BIODIESEL EFFLUENT from *JATROPHA CURCUS*

Osarumwense, J. O.[1] and Okolafor, F. I[1,2*]

[1]Department of Science Laboratory Technology, Faculty of Life Sciences, University of Benin, Benin City, ORCID: 0000-0002-5542-7787
[2]Applied Environmental Bioscience and Public Health Research Group, Dept. of Microbiology, University of Benin, Nigeria, fidelis.okolafor@uniben.edu, ORCID: 0000-0002-5025-1698

Received Date:04.06.2021 *Accepted Date:28.12.2021*

ABSTRACT

The utilization of biodiesel produced from *Jatropha curcus* as renewable energy is relatively new area of research. The waste generated during biodiesel production may cause serious impact on the soil. The present study was aimed at optimizing microbial consortia in the degradation of biodiesel effluent (BDE). A portion of land (loamy soil) measuring 1.5 m by 1.5 m was polluted with BDE for 28 days. Standard microbiological and chemical methods were used to determine BDE utilizing organisms and physicochemical properties of the soil. The result of the total heterotrophic microbial counts from BDE polluted site at 0 to 28 days revealed significance $p<0.0001$, $p<0.001$ and $p<0.01$ for bacterial, fungal and yeast counts. Percentage occurrence of bacterial isolates from BDE polluted soil showed high values for *Bacillus subtilis* (28.95%), *Pseudomonas aeruginosa* (21.05%), *Staphylococcus epidermidis* (18.42%), *Staphylococcus aureus* (15.79%). *Aspergillus niger* (20.63%) and *Saccharomyces kluyveri* (14.29%) also recorded highest occurrence for fungi and yeast isolates respectively. Performance level for the growth rate of bacterial isolates in BDE showed highest against *Staphylococcus epidermidis* (OD 1.6 at day 4), *Bacillus subtilis* (OD 1.5 at day 6) and *Pseudomonas aeruginosa* (OD 1.4 at day 4). The result from this study revealed the effect of depth in the degradation capacity of consortia microorganisms in BDE polluted soil.

Keywords: *Jatropha curcus*, biodiesel effluent (BDE), microbial consortia, optimization, degradation

1. INTRODUCTION

The world is shifting to renewable source of energy due to green-house gas emission into the atmosphere**.** Biodiesel from *Jatropha curcas* (JC) has widely been explored by researchers as alternative source of bioenergy. Biodiesel from JC provides an alternative to petroleum energy balance, which burns with less harmful emission, low sulphur and carbon dioxide, biodegradable, nontoxic, and environmentally beneficial in terms of cost and efficiency [1]. Large amount of waste are generated during the process of

biodiesel production [2], which in turn pollute the receiving soil where biodiesel plants are situated in the form of effluent. These wastes may pose serious environmental impact to the ecosystem.

Wastewater from alkali-catalyzed biodiesel production process is alkaline in nature with a high content of oil and grease, and low content of nitrogen and phosporus [2]. Biodiesel effluent (BDE) are reported to contain high biochemical oxygen demand (BOD), chemical oxygen demand (COD), total dissolve solute (TDS), glycerol and residual fat, oil and grease [3].

Studies on BDE treatment revealed several approaches which include electrochemical coagulation [4, 5], advanced oxidation process [3], dissolved air flotation [6], and integrated treatment process [7]. These methods used so far were characterized with one disadvantage or another. Electrochemical coagulation generates metal hydroxide in solution which further pollutes the wastewater; advanced oxidation method leads to formation of intermediate compounds that may be more harmful and difficult to degrade. The biological methods used involve the utilization of already established pure culture of microorganisms for the treatment of BDE [8, 9]. Information on the degradation potential of BDE using native microorganisms in the soil is relatively scarce. Given the enormous environmental impact BDE has on the environment, this study is aimed at optimizing microbial consortia in the soil for the degradation of BDE.

2. MATERIALS AND METHODS

2.1. Preparation of Contaminated Site.

A portion of land (Loamy Soil) measuring 1.5 m by 1.5 m was marked out for contamination with BDE. The site was polluted with 20 dm^3 of biodiesel effluent and allowed to stay for seven (7) days. Prior to pollution, soil samples from the marked portion of land was analysed to ascertain the indigenous soil microflorals (control). After contamination, soil samples were collected at depth 0-10 cm, 10-20 cm and 20-30 cm for 28 days in an interval of 7 days.

2.2. Characterization of Soil Samples

The characterization of soil such as moisture content, clay, sand, and silt content, organic matter, soil pH, exchangeable capacity, micro and macro nutrient were determined following the method according to Cresswell and Hamilton [10].

2.3. Enumeration and Isolation of Microbial Isolates (pre and post contamination).

Serial dilution was carried out according to the method of Ishak *et al*. [11]. A 1 cm^3 aliquot from 10^{-4} dilution factor was plated in triplicates for bacteria (Nutrient agar), fungal (Potato dextrose agar) and yeast (Yeats extract agar). 0.5 g chloramphenicol was introduced to potato dextrose and yeast extract agar to inhibit bacteria growth. Colony forming unit per gram (cfu/g) was calculated following the methods of Onifade and Abubakar [12].

2.4. Characterization of Microbial Isolates

Phenotypic characterization of all the microbial isolates was carried out to identify the soil microflorals [13, 14] . The percentage occurrence of the identified isolates was obtained according to the method by Okechi *et al*. [15].

JSR A
Journal of Scientific Reports

2.5 Microbial optimization for growth rate of isolates

Microbial growth rate determination was carried out following the methods described by Lapinskiene *et al*. [16] and Obayori *et al.* [17]. Replicate conical flasks containing 50 cm^3 of biodiesel effluent with 10 cm^3 of mineral salt medium (MSM) were prepared. The flasks were autoclaved for 15 minutes, and after cooling, 1cm^3 of inoculated broth of each microorganism was added to the different flasks and incubated at room temperature for a period of 14 days. Flasks containing the wastewater and MSM only (un-inoculated) served as controls. The increase in cell density was determined by measuring the optical density (OD) at 600 nm using a UV/Vis spectrophotometer (Model T70). The microbial isolates that showed appreciable growth were selected and used for the biodegradation of biodiesel wastewater.

Table 1. Physiochemical properties of polluted and unpolluted soil samples.

Parameters	**Before Pollution**			**After Pollution**		
	0-10cm	**10-20cm**	**20-30cm**	**0-10cm**	**10-20cm**	**20-30cm**
pH	5.96	5.83	6.33	6.12	7.98	7.92
EC (µs/cm)	138	175	117	152	206	144
BD (g/cm^3)	1.21	1.22	1.27	1.21	1.21	1.28
MC (%)	20.85	23.10	23.09	27.31	24.64	23.85
E.A (meq/100g)	0.20	0.24	0.21	0.18	0.22	0.20
E.B (meq/100g)	5.03	4.24	3.38	7.58	6.41	5.34
CEC (meq/100g)	5.58	5.64	4.58	5.16	5.93	5.81
OC (%)	0.92	1.14	0.96	0.91	1.11	0.97
OM (%)	1.59	1.97	1.66	1.57	1.92	1.68
Clay (%)	17.16	23.10	15.16	17.16	23.10	15.16
Silt (%)	4.27	4.36	3.24	4.27	4.36	3.24
Sand (%)	78.57	72.54	81.60	78.57	72.54	81.60

JSR A
Journal of Scientific Reports

Table 2. Macro-element in the polluted and unpolluted soil samples.

Soil Sample	**Depth (cm)**	**Total-nitrogen (mg/100g)**	**Total-phosphorus (mg/100g)**	**Total-potassium (meq/100g)**
Before Pollution	0-10	1.68	3.17	0.22
	10-20	1.12	2.56	0.18
	20-30	1.68	3.80	0.18
After Pollution	0-10	1.68	3.06	1.23
	10-20	1.14	2.36	0.11
	20-30	1.14	2.71	0.15

Table 3. Total heterotrophic microbial count from Biodiesel effluent polluted soil at different depths.

Sampling Period (Day)	**Depths of soil (cm)**	**Bacterial Counts (cfu/g) x 10^4**	**Fungal Count (cfu/g) x 10^4**	**Yeast Count (cfu/g) x 10^5**
Control (unpolluted Soil)	0 - 10	2.30±0.72	9.70±0.80	1.60±0.15
	10 - 20	2.40±0.54	8.80±0.82	1.70±0.10
	20 - 30	1.20±0.61	1.19±1.36	0.32±0.02
1 – 7	0 - 10	6.0±0.59	0.32±0.05	0.35±0.02
	10 - 20	6.9±0.40	0.26±0.03	1.18±0.18
	20 - 30	2.6±0.91	0.42±0.04	4.00±0.05
8 – 14	0 - 10	12.5±0.90	0.30±0.05	0.80±0.04
	10 - 20	8.30±0.21	0.40±0.05	0.20±0.15
	20 - 30	7.00±0.25	0.34±0.02	0.12±0.01

15 – 21	0 - 10	5.50±0.21	9.00±0.49	0.96±0.02
	10 - 20	4.00±1.57	8.50±0.50	0.90±0.12
	20 - 30	2.10±0.45	7.50±0.31	0.15±0.15
22 – 28	0 - 10	3.70±0.66	6.30±0.64	0.07±0.01
	10 - 20	4.10±2.21	4.50±0.76	0.06±0.02
	20 - 30	1.80±0.61	6.80±0.41	0.01±0.03
p-values		0.000	0.001	0.01

Values in triplicate, Mean±Standard Deviation

Table 4. Frequency of occurrence of bacterial isolates.

Sampling Period (Day)	***Pseudomonas aeruginosa***	***Staphylococcus aureus***	***Staphylococcus epidermidis***	***Bacillus Subtilis***	***Micrococcus letus***	***Proteus mirabilis***	**% Occurrence of total isolates**
Control (unpolluted Soil)	2	1	1	1	1	1	18.42
7	2	1	1	3	1	1	23.68
14	1	2	2	3	2	0	26.32
21	1	2	2	2	0	0	18.42
28	2	0	1	2	0	0	13.16
% occurrence of each isolates	21.05	15.79	18.42	28.95	10.53	5.26	100

Table 5. Percentage frequency of occurrence of fungal/yeast isolates.

Sampling Period (Day)	**Fungi**					**Yeast**			
	Aspergillus niger	***Mucor* spp.**	***Aepergillus tamarii***	***Pennicillium notatum***	***Aspergilllus flavus***	***Saccharomyces kluyveri***	***Saccharomyces exiguus***	***Saccharomyces unisporus***	**% Occurrence of total isolates**
Control (unpolluted Soil)	3	2	3	2	1	2	2	1	25.40
7	2	2	2	1	1	2	1	2	20.63
14	3	2	2	1	2	2	1	1	22.22
21	3	1	0	1	1	2	2	2	19.05
28	2	1	1	0	0	1	1	2	12.70
% occurrence of each isolates	20.63	12.70	12.70	7.94	7.94	14.29	11.10	12.70	100

JSR A
Journal of Scientific Reports

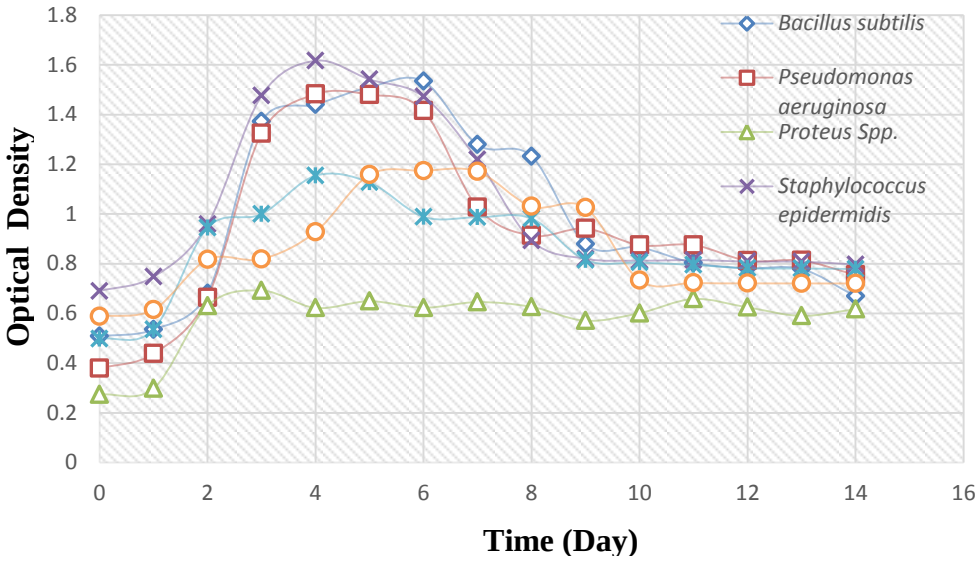

Figure 1. Growth curve of bacterial isolates in BDF wastewater.

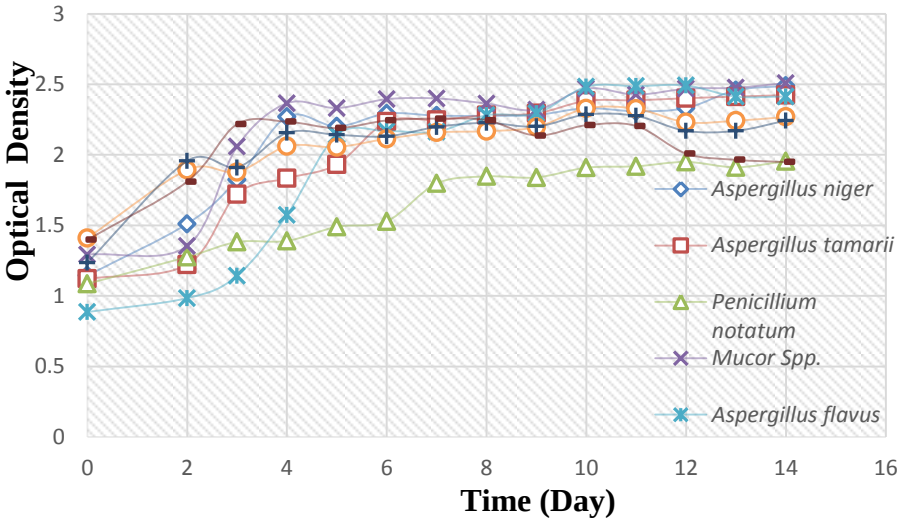

Figure 2. Growth curve of fungal isolates in BDF wastewater

3.RESULTS AND DISCUSSION

3.1. Physicochemical Properties of Polluted and Unpolluted Soil Samples

The physicochemical properties of the polluted and unpolluted soil samples were investigated (Table 1) to determine effect of physicochemical properties for the effective degradation of BDE. The pH, EC, BD, MC values increased as the depth of soil increased. The result of mid-pH values after pollution with BDE is in agreement with the reports of Siles *et al*. [18], who averred that acidification phase of BDE may be attributed to coagulation/flocculation process. There were no significant changes in the E.A, E.B and CEC values of soil with increased depth profile. There was low reduction recorded in OC (%), OM (%), Clay (%), Silt (%) values, with progressive increase in sand (%). The result of the physicochemical studies support the claim that depth of soil and physicochemical properties affect population and metabolic activity of soil microflora as revealed in this study. Progressive decrease in soil macro-elements, total N, total P and total K was recorded.

3.2. Microbial Counts of Biodiesel Effluent Polluted Soil at Different Depths

The total heterotrophic microbial count from biodiesel effluent polluted soil at different depths recorded varied counts for bacterial, fungal and yeast with the sampling period under review. Depth of soil 0 to 10 cm recorded high population counts for bacterial, fungal and yeast, followed by 10 to 20 cm depth, while 20 to 30 cm recorded low microbial counts. As the depth of the soil increased, the population counts of the soil microflora decreased. There was significant reduction in population count for the fungal and yeast after pollution with BDE. The result of the total heterotrophic microbial counts from BDE polluted site at 0 to 28 days recorded significance $p<0.0001$, $p<0.001$ and $p<0.01$ for bacterial, fungal and yeast counts respectively.

Several study have reported soil microbiome in degradation of BDE [19, 16] after first week of pollution. Frequency of occurrence of bacterial isolates recorded high occurrence against *Bacillus Subtilis* (28.95 %), and low occurrence against *Proteus mirabilis* (5.26 %). For occurrence of fungal isolate *Aspergillus niger* (20.63 %) recorded the highest and *Pennicillium notatum* (7.94 %) lowest; yeast isolates recorded highest against *Saccharomyces kluyveri* (14.29 %) and lowest against *Saccharomyces unisporus* (12.70%). The result of this study revealed high bacterial presence compared to fungal and yeast. The presence of the bacterial in high percentage may be attributed to the ubiquitous nature of bacteria population.

3.3. Biodegradation Potential of Microbial Consortia from Soil Polluted with BDE

The degradation of biodiesel result in the production of mineral diesel that are easily absorbed by soil microflora's [20, 21, 16, 22]. Growth curve of bacterial isolates in BDE wastewater (Figure 1) revealed highest population density against *Staphylococcus epidermidis* (OD 1.6 at day 4), *Bacillus Subtilis* (OD 1.5 at day 6) and *Pseudomonas aeruginosa* (OD 1.4 at day 4). Lowest population density was confirmed against *Proteus* sp. and *Micrococcus letus.* Notable exponential growth rate was recorded between day 2 and day 7, while progressive decrease occurred between days 8 to 16. This study showed that active biodegradation of BDE occurs between days 0 to day 7.

The growth rate curve of fungal isolates in BDE wastewater (Figure 2) recorded lag phased between day 0 and day 4 for all the fungal isolates under review. Constant progressive exponential growth rate was

recorded against *Aspergillus niger*, *Aspergillus tamari*, *Mucor* sp. *Aspergillus flavus* and *Saccharomyces exiguus* at OD 1 to 1.5. *Penicillum notatum* recorded lowest exponential growth at OD 1.5 (day 4 and day 14). Unlike the bacterial species, fungal specials requires longer period for successive biodegradation.

4. CONCLUSION

The utilization of biodiesel produced from *Jatropha curcus* as renewable energy may cause significant impact to the receiving soil owing to the waste generated during this process. This study showed the effect of depth on the degradation capacity of consortia microorganisms such as *Staphylococcus epidermidis*, *Bacillus subtilis* and *Pseudomonas aeruginosa*. Bacterial isolates recorded shortest time of degradation compared to fungal isolates with up to 14 days degradation. In order to obtain successive degradation of BDE, optimization of consortia microorganisms is required to achieve better results.

5. STATISTICAL ANALYSIS

Descriptive statistics and one-way analysis of variance (ANOVA) was employed in this study using statistical package SPSS version 22.0.

ACKNOWLEDGEMENT

The authors declare that there was no conflict of interest in the course of this study.

REFERENCES

[1] Ma, F., Clements, L. D., and Hanna, M. A., (1999), The effect of mixing on transesterification of beef tallow. Bioresource Technology, 69, 289–93.

[2] Srirangsan, A., Ongwandee, M. and Chavalparit, O., (2009), Treatment of Biodiesel wastewater by electro-coagulation process. Environmental Asia, 2**,** 15-19.

[3] Ramirez, X. M. V. Mejía, G. M. H., PatiñoLópez, K. V., Vásquez G. R. and Sepúlveda, J. M. M., (2012), Wastewater treatment from biodiesel production via a coupled photo-fenton–aerobic sequential batch reactor (SBR) system. Water Science and Technology, 66(4), 824-830.

[4] Jaruwat, P., Kongjao, S. and Hunsom, M., (2010), Management of biodiesel wastewater by the combined process of chemical recovery and electrochemical treatment. Energy Conversion and Management, 51, 531-537.

[5] Ngamlerdpokin, K., Kumjadpai, S., Chatanon, P., Tungmanee, U., Chuenchuanchom, S., Jaruwat, P., Lertsathitphongs, P. and Hunsom, M., (2011), Remediation of biodiesel wastewater by chemical and electro-coagulation: A comparative study. Journal of Environmental Management, 92, 2454-2460.

[6] Rattanapan, C., Sawam, A., Suksaroj, T. and Suksaroj, C., (2011), Enhanced efficiency of dissolved air flotation for biodiesel wastewater treatment by acidification and coagulation processes. Desalination, 280, 370-377.

[7] De-Gisi, S., Galasso, M. and De-Foe. G., (2012). Full scale treatment of wastewater from biodiesel fuel production plant with alkali-catalyzed trans-esterification. Environmental Technology, 1-26.

[8] Suehara, K., Kwamoto, Y., Fujii, E. Khoda, J. and Yano, T., (2005), Biological treatment of wastewater discharged from biodiesel fuel production plant with alkali-catalyzed transesterification. Journal of Bioscience and Bioengineering 100(4), 437-442.

[9] Siles, J. A., Marthin, M. A., Chice, A. F. and Martins, A., (2010), Anaerobic co-digestion of glycerol and wastewater derived from biodiesel manufacturing. Bioresource Technology, 101, 6315-6321.

[10] Cresswell, H. P. and Hamilton, H., (2002), Particle Size Analysis: In soil physical measurement and interpretation from land evaluation, CSIRO publisher, Collingwood, Victoria 239p.

[11] Ishak, W., Jamek, S., Jalanni, N. A. and Jamaludin, N. M., (2011), Isolation and identification of bacteria from activated sludge and compost for municipal solid waste treatment system. International Conference on Biology, Environment and Chemistry, 24, 450-453.

[12] Onifade, A. K. and Abubakar, F. A., (2007), Characterization of hydrocarbon-degrading Microorganisms isolated from crude oil contaminated soil and remediation of the soil by enhanced natural attenuation. Research Journal of Microbiology, 2, 149-155.

[13] Gerhardt, P., Murray, E. G. R., Wood, A. W. and Krieg, R. N., (1994), Methods for General and Molecular Bacteriology. ASM press, Washinton D.C. 971pp.

[14] Ekhaise, F. O. and Meyer, O. (2011). Biodegradation of 2 - methoxyethanol by a new bacterium isolate *Pseudomonas* sp. strain VB under aerobic conditions. Journal of Applied Science and Environmental Management, 15(1), 51-55.

[15] Okechi, R. N, Oparaugo, J. U., Azuwike, C. O., Nnokwe, J. C., Chiegboka, N. and Ezenekwe, F. N. (2014). A survey on Microbial contaminants of snuff sold in local markets in Imo State, Nigeria . International Journal of Current Microbiology and Applied Science 3(9), 366-373.

[16] Lapinskiene, A., Martinkus, P. and Rebzdaite, V., (2006), Eco-toxicological studies of diesel and biodiesel fuels in aerated soil. Environmental Pollution, 142, 432-437.

[17] Obayori, O. S., Salam, L. B. and Ogunwum, O. S. (2014). Biodegradation of fresh and used engine oils by *Pseudomonas aeruginosa* LP5. Journal of Bioremediation and Biodegradation, 5, 1-7.

[18] Siles, J. A., Gutiérrez, M.C. Martín, M. A. and Martín, A, (2011), Physical–chemical and biomethanization treatments of wastewater from biodiesel manufacturing. Bioresource Technology, 102, 6348–6351.

[19] Hawrot-Paw, M. and Izwikow, M., (2015), Microbiome of soil contaminated by fuels. Folia Pomeranae Universitatis Technologiae Stetinensis, 322, 57–66.

[20] Makareviciene, V. and Janulis, P., (2003), Environmental effect of rapeseed oil ethyl ester. Renewable Energy, 28, 2395-2403.

[21] Pasqualino, J. C., Montané, D. and Salvadó, J., (2006), Synergic effects of biodiesel in the biodegradability of fossil-derived fuels. Biomass Bioenergy, 30, 874-879.

[22] Mariano, A. P., Tomasella, R. C., Oliveira, L. M., Contiero, J. and Angelis, D. F. (2008). Biodegradability of diesel and biodiesel blends. African Journal Biotechnology **7**: 1323-1328.

Kütahya Dumlupınar University
Institute of Graduate Studies

Journal of Scientific
Reports-A
E-ISSN: 2687-6167
Number 48, March 2022

RESEARCH ARTICLE

NEW SCHIFF BASES DERIVED from 3,4-DIAMINO-1*H*-1,2,4-TRIAZOLE-5(*4H*)-THIONE: SYNTHESIS and CHARACTERIZATION

Bülent BÜYÜKKIDAN[1], Nurgün BÜYÜKKIDAN [2], Aslı ATAR[3]

[1]Kütahya Dumlupınar University Arts and Science Faculty, Chemistry Department, bulent.buyukkidan@dpu.edu.tr, ORCID:0000-0001-9619-3246
[2]Kütahaya Dumlupınar University Arts and Science Faculty, Chemistry Department, nurgun.buyukkidan@dpu.edu.tr, ORCID:0000-0001-6879-9355
[3]Kütahya Dumlupınar University Arts and Science Faculty, Chemistry Department, asliatar@hotmail.com, ORCID:0000-0003-0708-8845

Received Date:30.10.2021 *Accepted Date:12.01.2022*

ABSTRACT

A new synthetic approach has been applied to obtain a compound 3,4-diamino-1*H*-1,2,4-triazole-5(*4H*)-thione (**2**) by using 5-amino-1,3,4-thiadiazole-2-sulfonamide (**1**) and hydrazine hydrate as starting materials. New Schiff bases (**3a-d**) are obtained by the reaction of the compound 3,4-diamino-1*H*-1,2,4-triazole-5(4*H*)-thione (**2**) and varied aldehydes. The structures of the new compounds were characterized by spectral (IR, ^{1}H and ^{13}C NMR) and elemental analysis.

Keywords: *Thione, Schiff base, Sulfonamide, Triazole, Hydrazine hydrate.*

1. INTRODUCTION

Due to the development of resistance to existing antibiotics, there is increasing interest in the synthesis of new and effective antibacterial agents [1-3]. 1,2,4-Triazoles have interested of the medicinal chemists because of their strong biological activity in a wide range of areas such as antimicrobial [4,5], antibacterial [6,7], antifungal [8], anticancer [9-11], antitubercular [12], antioxidant [13], anticonvulsant [14], antiviral [15, 16], antitubulin [17,18] and inflammatory [19]. 1,2,4-triazole and derivatives have biological properties as well as environmental, [20] industrial [21, 22] and agricultural [23] activities. In order to increase the therapeutic effect of the 1,2,4-Triazole compound, its derivatives were obtained by incorporating it into different compounds [24-26]. Nitrogen-containing heterocyclic molecules, which are a part of many natural products and drugs that are vital for improving the quality of life, constitute a very large part of chemical substances [24]. Schiff bases containing imine groups are formed as a result of condensation of primary amines with aldehydes or ketones [27, 28]. Schiff bases formed from aromatic aldehydes are more stable than those of aliphatic aldehydes [29]. Schiff bases of 1,2,4-triazoles have been found to have extensive biological properties and a variety of applications [30]. Derivatives of 4-amino-4*H*-1,2,4-triazole-3-thiones have been synthesized in different synthetic ways [31-38].

To our knowledge, no example of 1,2,4-triazole yielded from 5-amino-1,3,4-thiadiazole-2-sulfonamide (**1**) was reported. In this study, we synthesized the known 3,4-diamino-1*H*-1,2,4-triazole-

JSR A
Journal of Scientific Reports

5(4*H*)-thione (**2**) compound from **1** and hydrazine hydrate with a different approach from the literature [39, 40]. In addition, the new Schiff bases **3a-d** were obtained from the condensation of compound **2** with benzaldehyde and substituted benzaldehyde. The structures of the **2** and new Schiff bases **3a-d** were characterized by IR and NMR (^{1}H and ^{13}C) spectra and elemental analysis.

2. EXPERIMENTAL

2.1. General Methods and Materials

The chemicals used in the reactions were used without further purification. The compound **1** was synthesized as in the literature [41]. A Leco CHNS-932 instrument was used for elemental analysis Bruker Avance DPX-400 MHz spectroscopic instrument for ^{1}H and ^{13}C NMR spectra, and Bruker Optics vertex 70 device for IR spectra taken with ATR.

2.2. Synthesis of 3,4-diamino-1H-1,2,4-triazole-5(4H)-thione (2)

To a solution of **1** (554 mmol) in ethanol/xylene (10/5 ml) hydrazine hydrate (554 mmol) was added. The resulting solution was refluxed for 3 days. The volatile component was vaporized using vacuum and then the crude product was crystallized from water to give colorless crystals of **2**. Suggested mechanism for this synthetic approach is given in Figure 1.

Crystals (85 %.), melting point 231-233˚C. ^{1}H-NMR (d_6-DMSO) δ/ppm: 12.42 (s, 1H, NH), 5.23 (s, 2H, H_2N-C), 5.95 (s, 2H, H_2N-N). ^{13}C-NMR (d_6-DMSO) δ/ppm: 163.87 (C=S), 152.75 (C=N). IR (cm^{-1}): 3385, 3297/3182 (NH_2/NH), 1651 ν(C=N)$_{triazole}$, 1269 (C=S). Anal. Calcd. %, for $C_2H_5N_5S$ (M_r = 131.16): C 18.31, H 3.84, N 53.40, S 24.45; found: C 18.47, H, 3.88, N 53.90, S 24.50.

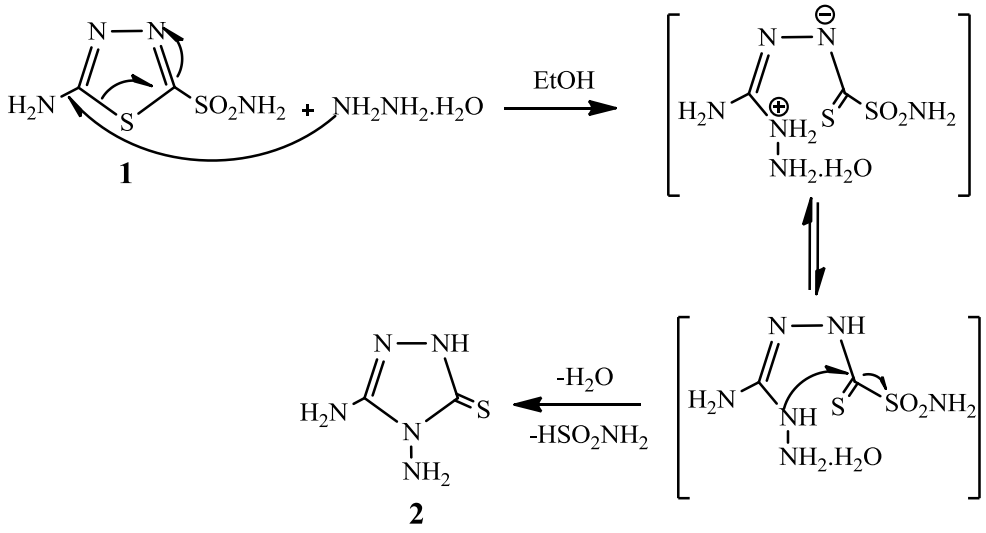

Figure 1. Synthesis of **2**.

2.3. General Procedure for the Preparation of the Schiff Bases (3a-D)

The mixture of **2** (0.40 mmol) in water (10 mL) and benzaldehydes (benzaldehyde, 3,4-dimethoxybenzaldehyde, 4-*N*,*N*'-dimethylbenzaldehyde, 2-hydroxybenzaldehyde) (0.36 mmol) in EtOH (10 mL) with the addition of a few drops of CH_3COOH was stirred for two days. The solid was

JSR A
Journal of Scientific Reports

filtered, washed with water and dried in air. Ethanol was used for the recrystallization of the obtained compounds (**3a-d**) (Figure 2). All prepared compounds are soluble in DMSO solvent and stable in air.

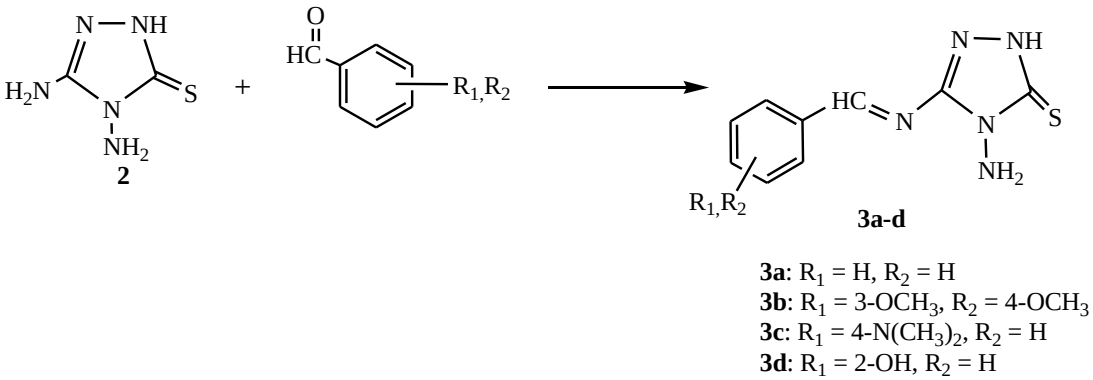

Figure 2. Syntheses of Schiff bases **3a-d**

2.3.1. (E)-4-amino-3-(benzylideneamino)-1*H*-1,2,4-triazole-5(4*H*)-thione (3a)
Light green crystals (68 %), melting point 212-214˚C. ^{1}H-NMR (d_6-DMSO) δ/ppm: 13.73 (s, 1H, NH), 8.05 (s, 1H, CH=N)$_{imine}$, 7.63-7.53 (m, 5H, C-H)$_{ar}$, 5.80 (s, 2H, NH_2). ^{13}C-NMR (d_6-DMSO) δ/ppm: 178.02 (C=S), 160.00 (CH=N)$_{imine}$, 152.10 (C=N)$_{triazole}$, 133.70 (C=C)$_{ar}$, 132.54 (C=C)$_{ar}$, 129.51 (C=C)$_{ar}$, 128.37 (C=C)$_{ar}$. IR (cm^{-1}): 3394, 3281/3191 (NH_2/NH), 3137 (C-H)$_{ar}$, 1654 ν(CH=N)$_{imine}$, 1636 ν(C=N)$_{triazole}$, 1602-1461 (C=C)$_{ar}$, 1268 (C=S). Anal. Calcd. %, for $C_9H_9N_5S$ (M_r = 219.27): C 49.30, H 4.14, N 31.94, S 14.62; found: C 49.37, H 4.18, N 31.98, S 14.70.

2.3.2. (E)-4-amino-3-((3,4-dimethoxybenzylidene)amino)-1*H*-1,2,4-triazole-5(4*H*)-thione (3b)
Light green crystals (75 %), melting point 252-254˚C. ^{1}H-NMR (d_6-DMSO) δ/ppm: 13.85 (s, 1H, NH), 8.10 (s, 1H, CH=N)$_{imine}$, 7.46-7.23 (m, 3H, C-H)$_{ar}$, 5.82 (s, 2H, NH_2), 3.90 (s, 3H, OCH_3), 3.85 (s, 3H, OCH_3). ^{13}C-NMR (d_6-DMSO) δ/ppm: 187.23 (C=S), 163.32 (CH=N)$_{imine}$, 151.32, (C-OCH_3), 150.67 (C-OCH_3), 148.42 (C=N), 129.98 (C=C)$_{ar}$, 125.79 (C=C)$_{ar}$, 119.07 (C=C)$_{ar}$, 118.34 (C=C)$_{ar}$, 117.63 (C=C)$_{ar}$, 58.24 (OCH_3). IR (cm^{-1}): 3392, 3259/3189 (NH_2/NH), 3103 (C-H)$_{ar}$, 2953 (C-H)$_{aliph}$, 1651 ν(CH=N)$_{imine}$, 1601 ν(C=N)$_{triazole}$, 1572-1462 (C=C)$_{ar}$, 1269 (C=S). Anal. Calcd. %, for $C_{11}H_{13}N_5O_2S$ (M_r = 279.32): C 47.30, H 4.69, N 25.07, S 11.48; found: C 47.53, H, 4.76, N 25.14, S 11.70.

2.3.3. (E)-4-amino-3-((4-(dimethylamino)benzylidene)amino)-1*H*-1,2,4-triazole-5(4*H*)-thione (3c)
Yellow crystals (80 %), melting point 226-228˚C. ^{1}H-NMR (d_6-DMSO) δ/ppm: 8.12 (s, 1H, CH=N)$_{imine}$, 7.25 (d, 2H, J = 7.60 Hz, C-H)$_{ar}$, 6.85 (d, 2H, J = 7.60 Hz, C-H)$_{ar}$, 5.85 (s, 2H, NH_2), 3.15 (s, 6H, CH_3). ^{13}C-NMR (d_6-DMSO) δ/ppm: 190.16 (C=S), 165.23 (CH=N)$_{imine}$, 155.33 (C=N)$_{triazole}$, 153.48 (C-NCH_3), 133.15 (C=C)$_{ar}$, 125.38 (C=C)$_{ar}$, 111.42 (C=C)$_{ar}$, 40.24 ($N(CH_3)_2$). IR (cm^{-1}): 3112, 3061 (C-H)$_{ar}$, 2845 (C-H)$_{aliph}$, 1660 ν(CH=N)$_{imine}$, 1642 ν(C=N)$_{triazole}$, 1618-1458 (C=C)$_{ar}$, 1271 (C=S). Anal. Calcd. %, for $C_{11}H_{14}N_6S$ (M_r = 262.33): C 50.36, H 5.38, N 32.04, S 12.22; found: C 50.45, H, 5.42, N 32.13, S 12.38.

JSR A
Journal of Scientific Reports

2.3.4. (E)-4-amino-3-((2-hydroxybenzylidene)amino)-1*H*-1,2,4-triazole-5(4*H*)-thione (3d)
Colourless crystals (78 %), melting point 230-232˚C. ^{1}H-NMR (d_6-DMSO) δ/ppm: 12.98 (1H, NH), 9.10 (s, 1H, OH), 8.50 (s, 1H, CH=N)$_{imine}$, 7.46 (d, 1H, J = 7.51 Hz, C-H)$_{ar}$, 7.33 (t, 1H, J = 7.52 Hz, C-H$_{ar}$), 6.95 (t, 1H, J = 7.52 Hz, C-H)$_{ar}$, 6.02 (d,1H, J = 7.52 Hz, C-H)$_{ar}$, 5.62 (s, 2H, NH_2). ^{13}C-NMR (d_6-DMSO) δ/ppm: 185.00 (C=S), 165.32 (CH=N)$_{imine}$, 163.18 (C-OH), 152.76 (C=N)$_{triazole}$, 131.01 (C=C)$_{ar}$, 130.00 (C=C)$_{ar}$, 120.00 (C=C)$_{ar}$, 118.03 (C=C)$_{ar}$, 117.68 (C=C)$_{ar}$. IR (cm^{-1}): 3454(s) (OH), 3385, 326373171 (NH_2/NH), 3069 (C-H)$_{ar}$, 1637 ν(CH=N)$_{imine}$, 1617 ν(C=N)$_{triazole}$, 1566-1472 (C=C)$_{ar}$, 1244 (C=S). Anal. Calcd. %, for $C_9H_9N_5OS$ (M_r = 235.27): C 45.95, H 3.86, N 29.77, S 13.63; found: C 45.98, H 3.90, N 29.73, S 13.70.

3. RESULTS AND DISCUSSION

3.1. FT–IR Measurements of 2 and 3a-d

The IR spectroscopy data are given in Table 1 for **2** and **3a-d** (Figures A1-A5). The band of ν(OH) stretching vibration in the aromatic ring was observed at 3454 cm^{-1} and a band showing extensive H-bond interaction was also observed at 2974 cm^{-1} in the same region for **3d**. The NH_2 group gives two N-H vibration absorption bands, asymmetrical and symmetrical. Asymmetrical stretching vibration is observed at higher frequency than the symmetrical one. Asymmetrical (ν_{as}) and symmetrical (ν_s) stretching vibrations of NH_2 group were found to be 3385 and 3297 cm^{-1} for **2**. These bands were located in the range of 3394-3385 and 3281-3259 cm^{-1}, respectively in the IR spectra of compounds **3a-d**. It has been reported in the literature that N-H asymmetrical and symmetrical vibrations of the triazole-based compound are observed at 3331 and 3253 cm^{-1} [42]. The N-H vibration band of 1,2,4-triazole was found as 3182 cm^{-1} for **2**, 3191 cm^{-1} for **3a,** 3189 cm^{-1} for **3b** and 3171 cm^{-1} for **3d**. This band was not observed in compound **3c** due to the very rapid thione-thiol tautomerism exchange. Aromatic ν(C-H) stretching vibration bands were observed at 3137 cm^{-1} for **3a**, 3103 cm^{-1} for **3b**, 3112 and 3061 cm^{-1} for **3c** and 3069 cm^{-1} for **3d**. Sharp absorption bands belonging to imine groups ν(CH=N) of compounds **3a-d** showing Schiff base formation were observed in the range of 1660-1637 cm^{-1}.

Table 1. Some selected IR[a] frequencies (cm^{-1}) of the prepared compounds **2** and **3a-d**.

Comp	O-H	NH_2/ NH	$(C-H)_{ar}$	$(C-H)_{aliph}$	CH=N	C=N	C=C	C=S
2		3385(w) 3297(w) 3182(w)				1651(s)		1269(m)
3a		3394(w)) 3281(w) 3191(w)	3137(w)		1654(s)	1636(s)	1602-1461(s)	1268(m)
3b		3392(w) 3259(w) 3189(w)	3103(w)	2974(w)	1652(s)	1636(s)	1620-1457(s)	1277(m)
3c			3112(w) 3061(w)	2845(w)	1660(s)	1642(s)	1618-1458(s)	1271(m)
3d	3454(s)	3385(w) 3263(w) 3171(w)	3069(w)		1637(s)	1617(s)	1566-1472(s)	1244(m)

JSR A
Journal of Scientific Reports

[a] ATR technique.
w: weak, m: medium, s: sharp.

IR spectroscopy is of great importance in the structure analysis of triazoles. Stretching vibration bands observed at 1572 and 1562 cm^{-1} for C=N group are characteristic bands for the triazole ring [43, 44]. The stretching vibration bands of ν(C=N) for compound **2** and **3a-d** were observed at 1651 cm^{-1} and 1642-1617 cm^{-1}, respectively. The aromatic vibration bands of ν(C=C) were exhibited in the range of 1602-1461 cm^{-1} for **3a**, 1620-1457 cm^{-1} for **3b**, 1618-1458 cm^{-1} **3c** and 1566-1472 cm^{-1} for **3d**. The IR spectrum is also important in elucidating the thione-thiol tautomeric structures of **2** and **3a-d** compounds (Figure 3).

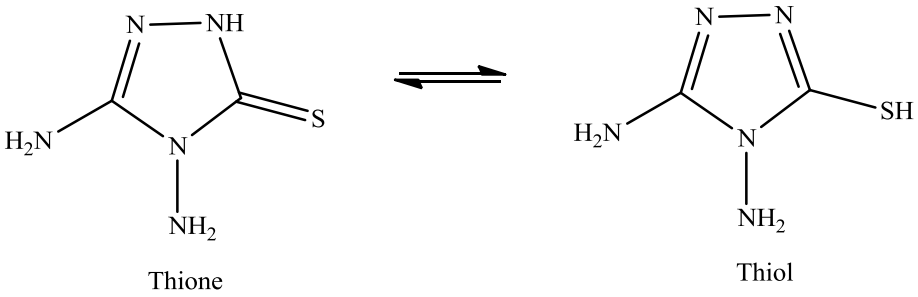

Figure 3. Tautomeric forms of **2**.

Stretching vibration band of C=S group gives characteristic band for thione at 1258 cm^{-1} [45], 1189 cm^{-1} [46] and 1166 cm^{-1} [47] cm^{-1}. The indicator of the synthesized **2** and **3a-d** compounds in the form of thione is the formation of a sharp C=S vibration band at 1269 cm^{-1}.and in the range of 1271-1244 cm^{-1}, respectively. Because the C=S bond is weaker than the C=N bond and is observed at lower frequency [48, 49]. The examinations on the thione-thiol tautomer have shown that the predominant form in the gas phase and solution is the thione tautomer [**Hata! Yer işareti tanımlanmamış.**].

3.2. ^{1}H-NMR and ^{13}C-NMR spectra of 2 and 3a-d.

NMR (^{1}H and ^{13}C) spectra of compounds **2** and **3a-d** (Figures A1-A5) were taken in DMSO-d_6 solvent at 25 °C and TMS was used as internal standard. NMR (^{1}H and ^{13}C) assignments were given in Table 2 and 3 for compounds **2** and **3a-d**. Compound **2** can exist in two tautomeric forms, 4,5-diamino-4*H*-1,2,4-triazole-3-thiol and 3,4-diamino-1*H*-1,2,4-triazole-5(4*H*)-thione. The spectral analysis of compound **2** exhibits that it exists in the second form. It was determined that the peak observed at δ 12.42 ppm in the ^{1}H-NMR spectrum belonged only to NH instead of SH. Confirmation of this comes from the absence of the ν(S-H) absorption band, which should be observed at 2500 cm^{-1} in the IR spectrum. The ^{1}H NMR spectrum of **2** also displayed two singlets with intensity of 2H for two NH_2 group protons at δ 5.23 (C-NH_2) and δ 5.95 ppm (N-NH_2). The NMR spectra of **3a, 3b** and **3d** exhibited downfield signal with 1H intensity appearing at δ 13.73, 13.85 and 12.98 ppm, respectively were attributed to the NH proton. This peak was not observed in compound **3c** because of the rapid exchange of thione-thiol tautomerism. The peak observed at 5.23 ppm in the starting material (**2**) for NH_2 protons attached to a carbon atom of triazole ring was not observed in the new **3a-d**. In addition, the observation of a new peak of CH=N proton in **3a-d** indicates the formation of Schiff Bases. The CH=N proton in the **3a-d** compounds appeared in the range of 8.50-8.05 ppm.

JSR A
Journal of Scientific Reports

These data are in good agreement with the values (8.62 and 9.69 ppm) of similar compounds [50, 51]. If the formation of Schiff base was with the NH_2 group attached to the nitrogen atom in the 1,2,4-triazole ring, the CH=N proton should have been observed in the lower field due to the disshielding of C=S group [**Hata! Yer işareti tanımlanmamış.**, 52]. It was understood that a singlet with 1H intensity observed at δ 9.10 ppm in the NMR spectrum of **3d** belonged to the OH proton of the aromatic ring. The differently substituted aromatic rings protons in compounds **3a-d** were observed in the range δ 7.63-6.02 ppm. On the other hand NH_2 moieties on 1,2,4-triazole rings of Schiff bases **3a-d** were shifted downfield (δ 5.95-5.62 ppm) when compared to the chemical shift of NH_2 group in compound **2** (δ 5.23 ppm). The protons of NH_2 and OH groups were observed at 5.78 and 10.21 ppm, respectively in similar compounds [**Hata! Yer işareti tanımlanmamış.**, 50]. Two singlets for two OCH_3 protons with 3H intensity each have been seen at 3.90 and 3.85 ppm for compound **3b**. A singlet for $N(CH_3)_2$ protons with 6H intensity was observed at 3.15 ppm for compound **3c**.

Table 2. ^{1}HNMR chemical shifts (ppm) with coupling constants and assignments for compounds **2** and **3a-d**.

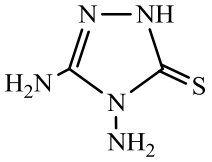

2

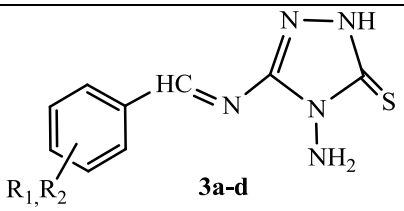

3a-d

Comp	NH	OH	$(CH=N)_{imine}$	$(C-H)_{ar}$	$C-NH_2$	$N-NH_2$	OCH_3 or $N(CH_3)_2$
2	12.42 (s, 1H)				5.23 (s, 2H)	5.95 (s, 2H)	
3a	13.73 (s, 1H)		8.05 (s, 1H)	7.63-7.53 (m, 5H)		5.80 (s, 2H)	
3b	13.85 (s, 1H)		8.10 (s, 1H)	7.46-7.23 (m, 3H)		5.82 (s, 2H)	3.90 (s, 3H) 3.85 (s, 3H)
3c			8.12 (s, 1H)	7.25 (d, 2H ^3J= 7.60 Hz) 6.85 d, 2H ^3J= 7.60 Hz)		5.85 (s, 2H)	3.15 (s, 6H)
3d	12.98 (s, 1H)	9.10 (s, 1H)	8.50 (s, 1H)	7.46 (d, 1H, ^3J= 7.51 Hz) 7.33 (t, 1H, ^3J= 7.52 Hz) 6.95 (t, 1H, ^3J= 7.52 Hz) 6.02 (d,1H, ^3J= 7.52 Hz)		5.62 (s, 2H)	

JSR A
Journal of Scientific Reports

Thiol and thione tautomers can also be characterized by the ^{13}C NMR spectra. In the ^{13}C NMR spectra of the compounds, the peak of the C=S carbon atom was observed at 163.87 ppm for **2**, 178.02 ppm for **3a**, 187.23 ppm for **3b**, 190.16 ppm for **3c** and 185.00 ppm for **3d**. Carbon atoms of CH=N and C=N groups also showed down field signals in the ranges of 165.32-160.00 and 155.33-148.42 ppm, respectively for **3a-d**. Substituted carbons resonated at 151.32 and 150.67 ppm for **3b**, at 153.48 ppm for **3c** and at 163.18 ppm for **3d**. Compound **2** shows a signal at 152.75 ppm for C=N group carbon of triazole ring. This band was observed in the range of aromatic ring carbons (C=C) were observed in the aromatic region for the Schiff bases in the range 133.70-128.37 ppm for **3a**, 129.98-117.63 ppm for **3b**, 133.15-111.42 ppm for **3c** and 131.01-117.68 ppm for **3d**. A peak has been seen at 58.24 ppm for OCH_3 carbons in the ^{13}C NMR spectrum of **3b**. ^{13}C NMR spectrum of **3c** showed a peak at 40.24 ppm for two CH_3 carbons.

Table 3. ^{13}C NMR chemical shifts (ppm) and assignments for compound **2** and **3a-d**.

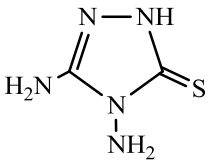

2

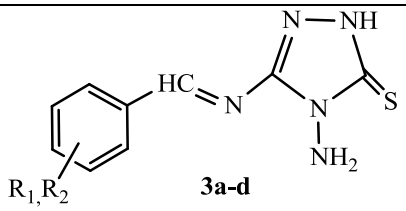

3a-d

Comp	C=S	$(CH=N)_{imine}$	C-OCH_3 C-$N(CH_3)_2$ C-OH	$(C=N)_{triazole}$	$(C=C)_{ar}$	OCH_3 or CH_3
2	163.87			152.75		
3a	178.02	160.00		152.10	133.70-128.37	
3b	187.23	163.32	151.32 and 150.67	148.42	129.98-117.63	58.24
3c	190.16	165.23	153.48	155.33	133.15-111.42	40.24
3d	185.00	165.32	163.18	152.76	131.01-117.68	

4. CONCLUSIONS

In conclusion, we have synthesized **2** from the starting materials **1** and hydrazine hydrate. New Schiff bases of **2** with various aromatic aldehydes have also been prepared. All of the synthesized compounds were characterized by spectral (IR, ^1H and ^{13}C NMR), and elemental analysis. The results obtained from the analyzes are compatible with the proposed structure of **2** and newly synthesized compounds **3a-d** as shown in Figures 1 and 2.

ACKNOWLEDGEMENTS

This study was supported by Kütahya Dumlupınar University (Grant No: 2008-1).

JSR A
Journal of Scientific Reports

REFERENCES

[1] Klimeˇsova, V., Zahajka, L., Waisser, K., Kaustova, J., M¨ollmann, U., (2004), Synthesis and antimycobacterial activity of 1,2,4-triazole 3-benzylsulfanyl derivatives, Il Farmaco, 59, 279–288.

[2] Zani, F., Vicini, P., Incerti, M., (2004), Synthesis and antimicrobial properties of 2-(benzylidene-amino)-benzo[d]isothiazol-3-ones, Eur. J. Med. Chem. 39, 135–40.

[3] Tehranchian, S., Akbarzadeh, T., Fazeli, M. R., Jamalifar, H., Shafiee, A., (2005), Synthesis and antibacterial activity of 1-[1,2,4-triazol-3-yl] and 1-[1,3,4-thiadiazol-2-yl]-3-methylthio-6,7-dihydrobenzo[c]thiophen-4(5H)ones, Bioorg. Med. Chem. Lett. 15, 1023–1025.

[4] Sahoo, S., Patwari, P. K., Kumar, M. C. B., Setty, C. M., (2013), Synthesis and Biological Activity of Certain Mannich Bases Derivatives from 1,2,4-Triazoles, Iranian J. Pharma. Sci., 9(4), 51–60.

[5] Al-Khuzaie, M. G. A., Al-Majidi, S. M. H., (2014), Synthesis, Characterization and Evaluation Antimicrobial Activity of Some New substituted 2-Mercapto-3-Phenyl-4(3H)- Quinazolinone, Iraqi J. Sci., 55(2B), 582–593..

[6] Mahmoud, M. R., Abou-Elmagd, W. S. I., . El-Shahawi, M. M., Hekal, M. H., (2014), Novel Fused and Spiro Heterocyclic Compounds Derived from 4-(4-Amino-5-mercapto-4H1,2,4-triazol-3-yl)phthalazin-1(2H)-one, Eur. Chem. Bull., 3(7), 723–728.

[7] Hanif, M., Saleem, M., Hussain, M. T., Rama, N. H., Zaib, S., Aslam, M. A. M., Jones, P. G., Iqbal, J., (2012), Synthesis, Urease Inhibition, Antioxidant and Antibacterial Studies of Some 4-Amino-5-aryl-3H-1,2,4-triazole-3- thiones and Their 3,6-Disubstituted 1,2,4-Triazolo[3,4-b]1,3,4-thiadiazole Derivatives, J. Braz. Chem. Soc., 23(5), 854–860.

[8] Hope, W. W., Lewis, R., Smith, J. A., (2010), Clinical Primer: Potential Hepatic Complications with Triazole Therapy, USA: University of Wisconsin-Madison School of Medicine and Public Health, School of Pharmacy, and School of Nursing and Fallon Medica LLC.

[9] Boraei, A. T. A., Singh, P. K., Sechi, M., Satta, S., (2019), Discovery of novel functionalized 1,2,4-triazoles as PARP-1 inhibitors in breast cancer: Design, synthesis and antitumor activity evaluation. Eur. J. Med. Chem., 182, 111621.

[10] Arul, K., Smith, A. A., (2014), In-Silico Design, Synthesis and in vitro Anticancer Evaluation of Some Novel 1,2,4- Triazole Derivatives, The Experiment, 21(1), 1439–1452.

[11] El-Sherief, H. A. M., Youssif, B. G. M., Abbas Bukhari, S. N., Abdelazeem, A. H., Abdel-Aziz, M., Abdel-Rahman, H. M., (2018), Synthesis, anticancer activity and molecular modeling studies of 1,2,4-triazole derivatives as EGFR inhibitors. Eur. J. Med. Chem., 156, 774–789.

[12] Meenaxi, M. M., Ainapure, R. Patil, P. B., Bhat, A. R., (2011), Triazolone and Their Derivatives for Anti-Tubercular Activities, Asian J. Res. Chem., 4(7), 1050–1054.

[13] Abdul Hameed, A., Hassan, F., (2014), Synthesis, Characterization and Antioxidant Activity of Some 4- Amino-5-phenyl-4H-1,2,4-triazole-3-thiol Derivatives, Int. J. App. Sci. Tech., 4 (2), 202–211.

[14] Jess, S., Kildea, S., Moody, A., Rennick, G., Murchie, A. K., Cooke, L. R., (2014), European Union policy on pesticides: implications for agriculture in Ireland. Pest Management Science, 70(11), 1646–1654.

[15] Abdullah, H. M., Jassim, I. K., Safi, M. N., (2012), Synthesis and Characterization of New Heterocyclic Compounds with Studying Its Biological Activity, Kerbala J. Pharm. Sci., 4, 115-135.

[16] Pandey, V. K., Tusi, Z., Tusi, S., Joshi, M., (2012), Synthesis and Biological Evaluation of Some Novel 5-[(3-Aralkyl amido/imidoalkyl)phenyl]-1,2,4-triazolo [3,4-b]-1,3,4- thiadiazines as Antiviral Agents, ISRN Org. Chem., 1-7.

[17] Mustafa, M., Anwar, S., Elgamal, F., Ahmed, E. R., Aly, O. M., (2019), Potent combretastatin A-4 analogs containing 1,2,4-triazole: Synthesis, antiproliferative, anti-tubulin activity, and docking study. Eur. J. Med. Chem., 183, 111697.

[18] Mustafa, M., Abdelhamid, D., Abdelhafez, E. S. M. N., Ibrahim, M. A. A., Gamal-Eldeen, A. M., Aly, O. M., (2017), Synthesis, antiproliferative, anti-tubulin activity, and docking study of new 1,2,4-triazoles as potential combretastatin analogues Eur. J. Med. Chem., 141, 293–305.

[19] Mousa, M. N., Al-jadaan, S. A. N.,(2012), Evaluation of the Anti-Inflammatory Activity and Ulcerogenic Liability of 5-(3-Chloro-1-benzothien-2-yl)-4-phenyl-4H-1,2,4- triazole-3-thiol, Bas. J. Vet. Res., 11(1), 122-127.

[20] Kavakli, C., Kavakli, P. A., Güven, O., (2014), Preparation and Characterization of Glycidyl Methylacrylate Grafted 4- Amino-1,2,4-triazole Modified Nonwoven Fiber Absorbent for Environmental Application, Rad. Phys. Chem., 94, 111-114.

[21] Hassan, F. A., Younus, K. W., (2012), Biological Evaluation of Some Azole Derivatives in Cooling Fluids (Lubricant Oils), Res. J. Bio. Sci., 7(1), 48-51.

[22] Sripriya1, S., Subha, C., Selvaraj, A., (2013), The Inhibition Chemistry of 2-Amino, 5-Phenyl 1, 3, 4-Triazole for Aluminium in Hydrochloric Acid Solution, IOSRJAC, 6(2), 25-29.

[23] Shukla, P. K., Soni, N., Verma, A., Jha, A. K., (2014), Synthesis, Characterization and in vitro Biological Evaluation of A Series of 1,2,4-Triazoles Derivatives & Triazole Based Schiff Bases, Der Pharma Chemica, 6 (3), 153- 160.

[24] Sun, S., Lou, H., Gao, Y., Fan, P., Ma, B., Ge, W., Wang, X., (2004), Liquid chromatography–tandem mass spectrometric method for the analysis of fluconazole and evaluation of the impact of phenolic compounds on the concentration of fluconazole in Candida albicans. J. Pharmöl and Biomed Anal., 34(5), 1117–1124.

[25] Clemons, M., Coleman, R., Verma, S., (2004), Aromatase inhibitors in the adjuvant setting: bringing the gold to a standard?, Cancer Treatment Reviews, 30(4), 325–332.

[26] Johnston, G., (2002), Medicinal Chemistry and Molecular Pharmacology of GABA-C Receptors. Curr. Top. Med.. Chem., 2(8), 903–913.

[27] Grivani, G., Tahmasebi, V., Eskandari, K., Khalaji, A. D., Bruno, G., & Rudbari, H. A. (2013). Synthesis, characterization, crystal structure determination and computational study of the two new bidentate O, N Schiff bases derived from bromosalicylaldehyde and amines containing alkyl halide pendant groups. J. Mol. Struct., 1054-1055, 100–106.

[28] Przybylski, P., Huczynski, A., Pyta, K., Brzezinski, B., Bartl, F., (2009), Biological Properties of Schiff Bases and Azo Derivatives of Phenols. Curr. Org. Chem., 13(2), 124–148.

[29] Wu, S., Zhang, W., Qi, L., Ren, Y., Ma, H., (2019), Investigation on 4-amino-5-substituent-1,2,4-triazole-3-thione Schiff bases an antifungal drug by characterization (spectroscopic, XRD), biological activities, molecular docking studies and electrostatic potential (ESP). J. Mol. Struct., 1197, 171-182.

[30] Bekircan, O., Bektas, H., (2006), Synthesis of New Bis-1,2,4-Triazole Derivatives. Molecules, 11(6), 469–477.

[31] Potts, K. T., Huseby, R. M., (1966), 1,2,4-Triazoles. XVI. Derivatives of the s-Triazolo[3,4-b][1,3,4]thiadiazole Ring System1. J. Org. Chem., 31(11), 3528–3531.

[32] Eweiss, N. F., Bahajaj, A. A., Elsherbini, E. A., (1986). Synthesis of heterocycles. PartVI. Synthesis and antimicrobial activity of some 4-amino-5-aryl-1,2,4-triazole-3-thiones and their derivatives. J. Heterocyclic. Chem., 23(5), 1451–1458.

[33] George, T., Mehta, D. V., Tahilramani, R., David, J., Talwalker, P. K., (1971), Synthesis of some s-triazoles with potential analgesic and antiinflammatory activities. J. Med. Chem., 14(4), 335–338.

[34] Bhalerao, U. T., Muralikrishna, C., Rani, B. R., (1994), Laccase enzyme catalysed efficient synthesis of 3-Substituted-1,2,4-triazoto(4,3-b)(4,1,2)benzothiadiazine-8-ones. Tetrahedron, 50(13), 4019–4024.

[35] Invidiata, F. P., Furná, G., Lampronti, I., Simoni, D., (1997), 1,2,4-Triazoles. Improved synthesis of 5-substituted 4-amino-3-mer-cato-(4H)-1,2,4-triazoles and a facile route to 3,6-disubstituted 1,2,4-triazolo[3,4-b][1,3,4]thiadiazoles. J. Heterocyclic Chem., 34(4), 1255–1258.

[36] Cartwright, D. D. J., Clark, B. A. J., McNab, H., (2001), Gas-phase pyrolysis of 4-amino-3-allylthio-1,2,4-triazoles: a new route to [1,3]thiazolo[3,2-b][1,2,4]triazoles, J. Chem. Soc. Perkin Trans, **1,** 424.

[37] Vainilavicius, P., Smicius, R., Jakubkiene, V., Tumkevicius, S., (2001), Synthesis of 5-(6-Methyl-2,4-dioxo-1,2,3,4-tetrahydro-3-pyrimidinyl)-methyl-4-amino-1,2,4-triazole-3-thione and

its Reactions with Polyfunctional Electrophiles. Monatshefte Fuer Chemie/Chemical Monthly, 132(7), 825–831.

[38] Shaker, R. M., & Aly, A. A. (2006). Recent Trends in the Chemistry of 4-Amino-1,2,4-triazole-3-thiones. Phosphorus, Sulfur, Silicon Relat Elem., 181(11), 2577–2613.

[39] Hoggarth, E. J. Chem. Soc. 1952, 4817.

[40] Ali, T. E.-S. (2009). Utility of thiocarbohydrazide in heterocyclic synthesis. J. Sulfur Chem., 30(6), 611-647.

[41] Bülbül, M., Kasimoğullari, R., Küfrevioğlu, Ö. I., (2008), Amide derivatives with pyrazole carboxylic acids of 5-amino-1,3,4-thiadiazole 2-sulfonamide as new carbonic anhydrase inhibitors: Synthesis and investigation of inhibitory effects. J. Enzyme. Inhib. Med. Chem., 23(6), 895–900.

[42] Kumar, M. S., Kumar, S. L. A., Sreekanth, A., Anticorrosion Potential of 4-Amino-3-methyl-1,2,4-triazole-5-thione Derivatives (SAMTT and DBAMTT) on Mild Steel in Hydrochloric Acid Solution. Ind. Engineer. Chem. Res, 51(15), 5408–5418, (2012).

[43] Shneine, J. K, Alaraji, Y. H, (2014), Chemistry of 1, 2, 4-Triazole: A Review Article, Int. J. Sci. Res., 5: 1411-1423..

[44] Subashchandrabose, S., Krishnan, A. R., Saleem, H., Thanikachalam, V., Manikandan, G., Erdogdu, Y., (2010), FT-IR, FT-Raman, NMR spectral analysis and theoretical NBO, HOMO–LUMO analysis of bis(4-amino-5-mercapto-1,2,4-triazol-3-yl)ethane by ab initio HF and DFT methods. J. Mol. Struct., 981(1-3), 59–70.

[45] Krishnakumar, V., Xavier, R. J., (2004), FT Raman and FT–IR spectral studies of 3-mercapto-1,2,4-triazole. Spectrochim. Acta A Mol. Biomol. Spectrosc., 60(3), 709–714.

[46] Bahgat, K., Fraihat, S., (2015), Normal coordinate analysis, molecular structure, vibrational, electronic spectra and NMR investigation of 4-Amino-3-phenyl-1H-1,2,4-triazole-5(4H)-thione by ab initio HF and DFT method. Spectrochim. Acta A Mol. Biomol. Spectrosc., 135, 1145–1155.

[47] Snehalatha, M., Ravikumar, C., Hubert Joe, I., Sekar, N., Jayakumar, V. S., (2009), Spectroscopic analysis and DFT calculations of a food additive Carmoisine. Spectrochim. Acta A Mol. Biomol. Spectrosc., 72(3), 654–662.

[48] Zamani, K., Faghihi, K., Sangi, M. R., Zolgharnein, (2003), Synthesis of Some New Substituted 1,2,4-Triazole and 1,3,4-Thiadiazole and Their Derivatives, Turk. J. Chem. 27, 119-126.

[49] Mohamed, G. G., Omar, M. M., Hindy, A. M. M., (2005), Synthesis, characterization and biological activity of some transition metals with Schiff base derived from 2-thiophene

carboxaldehyde and aminobenzoic acid. Spectrochim. Acta A Mol. Biomol. Spectrosc., 62(4-5), 1140–1150.

[50] Bagihallia, G.B., Patila, S.A., Badamib, P.S., (2009), Synthesis, Physicochemical Investigation and Biological Studies of Zinc(II) Complexes with 1,2,4-Triazole Schiff Bases, J. Iran. Chem. Soc., 6(2), 259-270.

[51] Joshi, R., Kumari, A., Singh, K., Mishra, H., & Pokharia, S. (2020). Triorganotin(IV) complexes of Schiff base derived from 1,2,4-triazole moiety: Synthesis, spectroscopic investigation, DFT studies, antifungal activity and molecular docking studies. Journal of Molecular Structure, 127639.

[52] Rafiq, M., Saleem, M., Hanif, M., Kang, S. K., Seo, S.-Y., Lee, K. H., (2015), Synthesis, structural elucidation and bioevaluation of 4-amino-1,2,4-triazole-3-thione's Schiff base derivatives. Arch. Pharm. Res., 39(2), 161–171.

APPENDICES

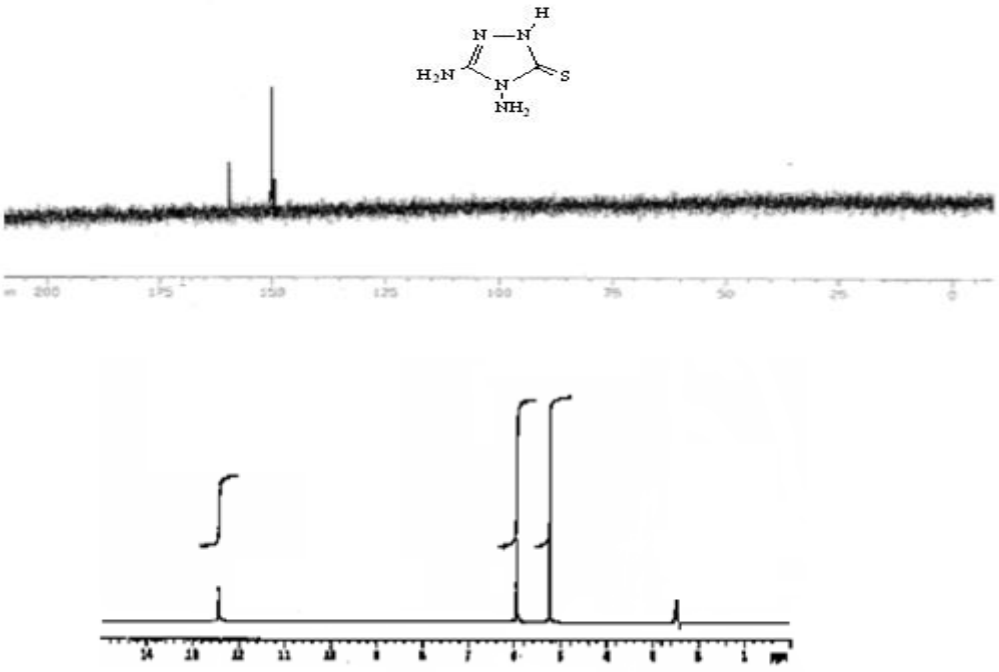

JSR A
Journal of Scientific Reports

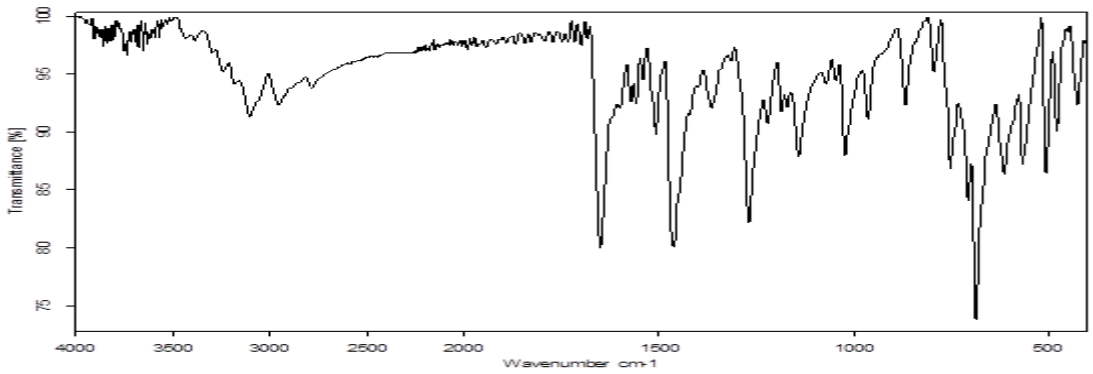

Figure A1. ^{1}H and ^{13}C NMR and IR spectra of **2**.

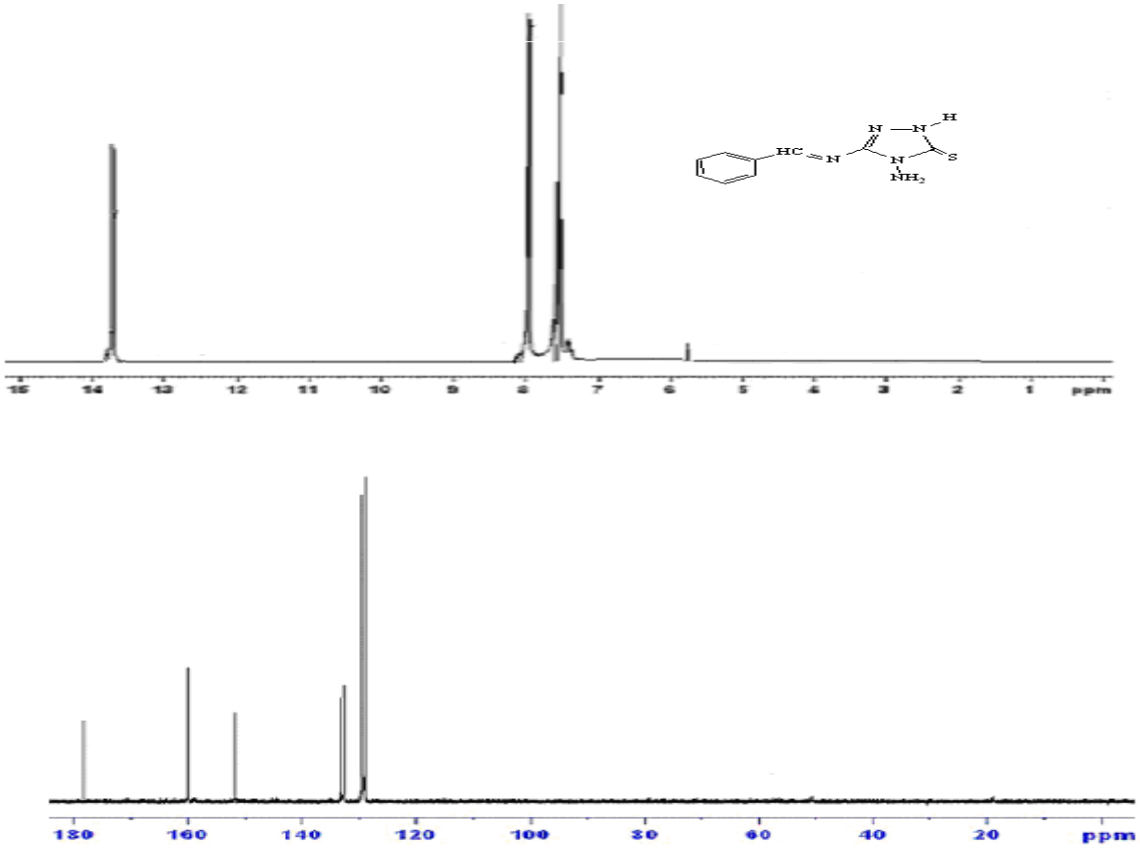

JSR A
Journal of Scientific Reports

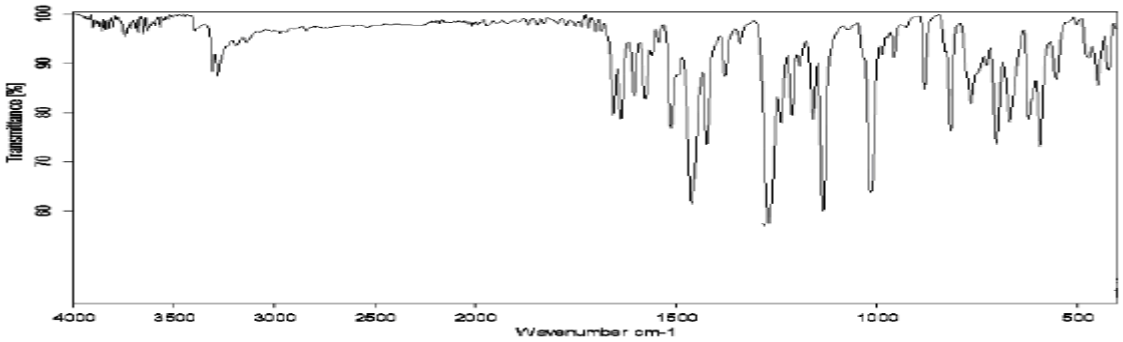

Figure A2. ^{1}H and ^{13}C NMR and IR spectra of **3a**.

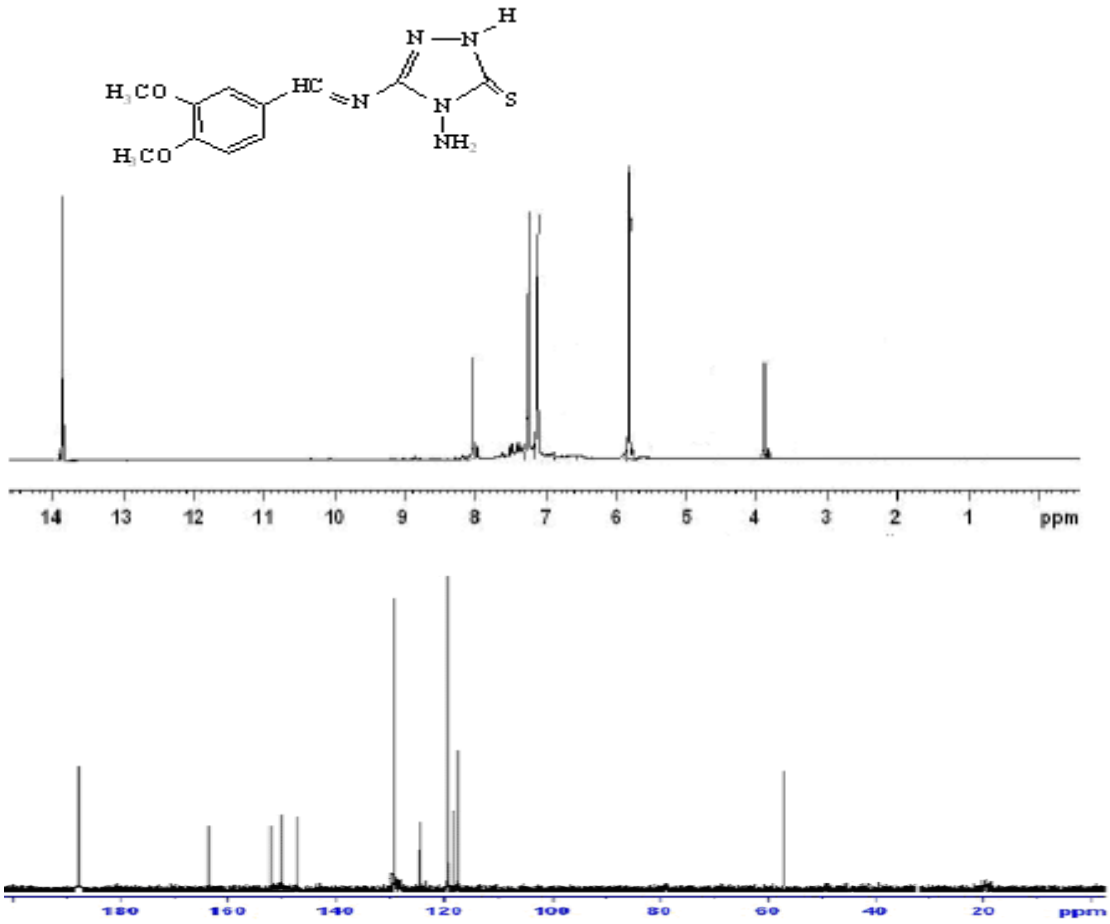

JSR A
Journal of Scientific Reports

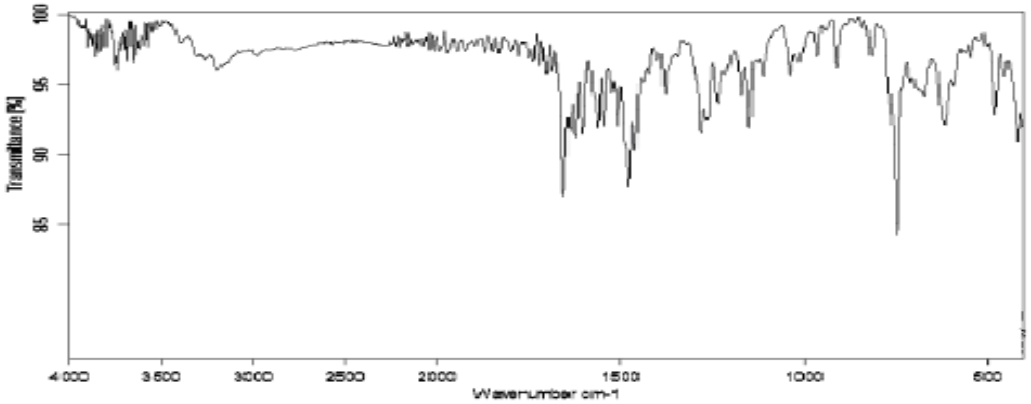

Figure A3. ^{1}H and ^{13}C NMR and IR spectra of **3b**.

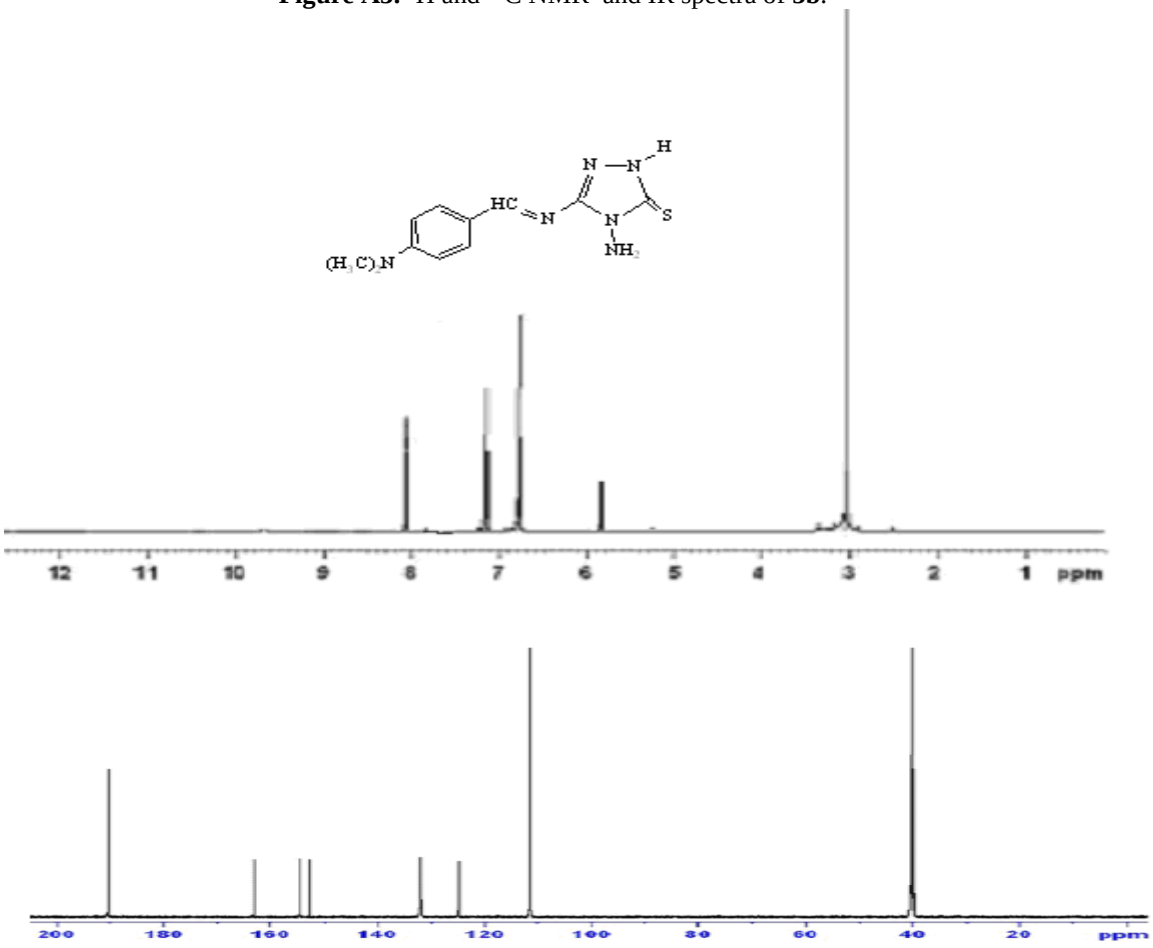

JSR A
Journal of Scientific Reports

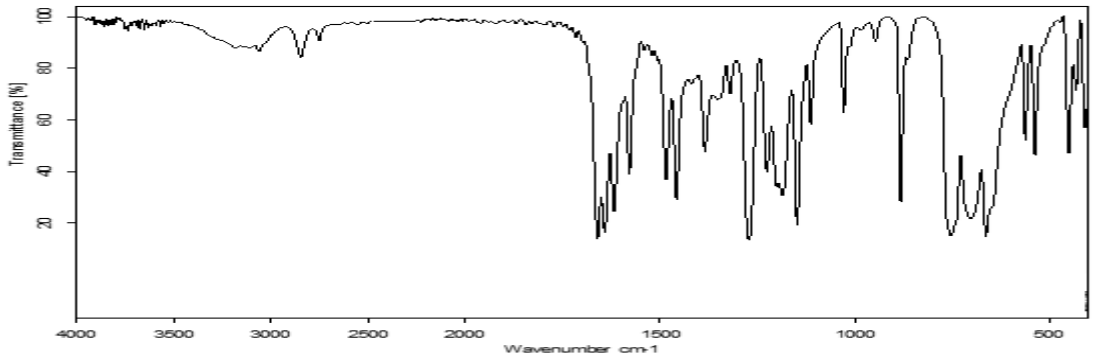

Figure A4. ^{1}H and ^{13}C NMR and IR spectra of **3c**.

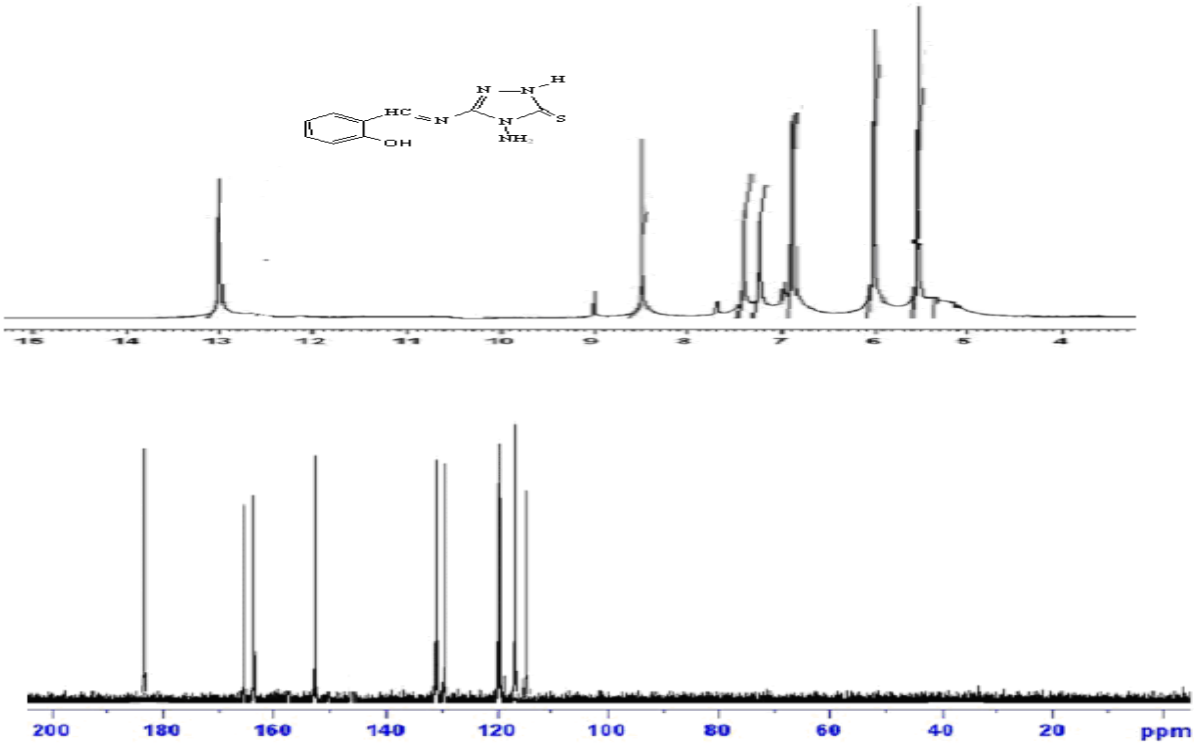

JSR A
Journal of Scientific Reports

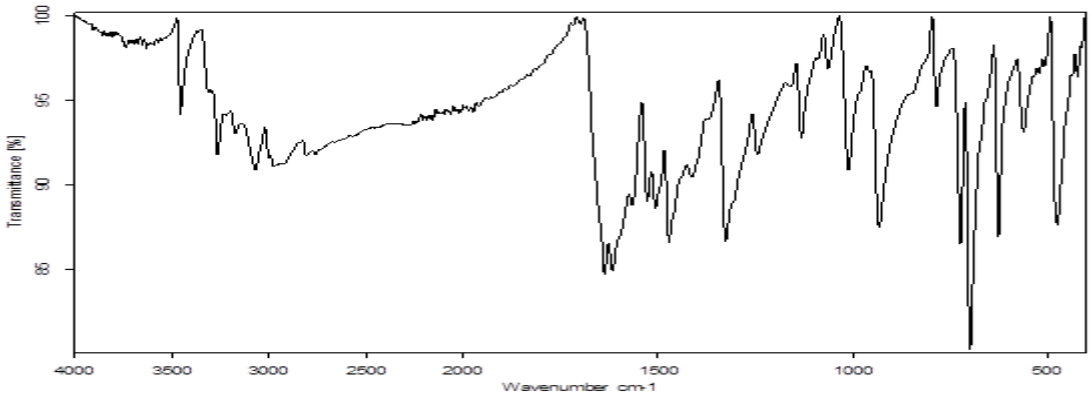

Figure A5. ^{1}H and ^{13}C NMR and IR spectra of **3d**.

Kütahya Dumlupınar University
Institute of Graduate Studies

Journal of Scientific
Reports-A
E-ISSN: 2687-6167
Number 48, March 2022

RESEARCH ARTICLE

CLASSIFICATION of CELLS INFECTED with the MALARIA PARASITE with RESNET ARCHITECTURES

İsmail AKGÜL[1,*], Volkan KAYA[2]

[1]Erzincan Binali Yıldırım University, Faculty of Engineering and Architecture, Department of Computer Engineering, iakgul@erzincan.edu.tr, ORCID: 0000-0003-2689-8675
[2]Erzincan Binali Yıldırım University, Faculty of Engineering and Architecture, Department of Computer Engineering, vkaya@erzincan.edu.tr, ORCID: 0000-0001-6940-3260

Received Date:03.02.2022 *Accepted Date:21.03.2022*

ABSTRACT

Malaria is a disease that causes a parasite called plasmodium to be transmitted to humans as a result of the bite of female anopheles' mosquitoes. Malaria is detected by examining the blood sample taken from the patient as a result of a microbiological examination under a microscope by specialist physicians. Although microscopy is widely used, its efficiency is low because it is time-consuming and depends on the interpretation of the specialist physician. In recent years, deep learning methods used in the field of computer vision increase the efficiency of specialist physicians by making a significant contribution to the decision-making process in solving real-life problems. In this study, ResNet architectures were preferred to quickly classify the malaria parasite using deep learning methods. For the training and testing of ResNet architectures, a dataset consisting of a total of 27558 red blood cell images containing 13779 parasitized and 13779 uninfected were used. Using this dataset, ResNet architectures were compared. As a result of the comparison, the best success accuracy (94.09%) was obtained with the ResNet-50 v2 model.

Keywords: *Deep learning, Convolutional neural network, ResNet, Malaria parasite classification*

1. INTRODUCTION

Malaria is a serious health problem that affects many people around the world. Malaria is a disease that causes a parasite called plasmodium to be transmitted to humans as a result of the bite of female anopheles mosquitoes [1,2]. People infected with the malaria parasite have a high fever, chills, headache, nausea and vomiting, cough, muscle pain and fatigue, sweating, chest and abdominal pain. While malaria is rare in temperate climates, it is common in tropical and subtropical climates [3,4]. Many drugs are used to treat malaria. However, the malaria parasite is highly resistant to these drugs. In long-term malaria cases, jaundice, anemia, respiratory complaints, and pneumonia may develop. Diagnosis of malaria may be difficult due to clinical deficiencies, long incubation period, or acquired immunity. Clinical diagnosis, microscopic diagnosis, molecular diagnosis, serology, antigen test, drug resistance test methods are used in the diagnosis of malaria [5]. The most widely used method among these methods is the microscopic diagnosis method [6,7]. In the microscopic diagnosis method, the only way to diagnose malaria in a person who has malaria is to have the patient's blood tests done [8].

Therefore, Malaria is detected by examining the blood sample taken from the patient under a microscope by specialist physicians as a result of a microbiological examination [9,10]. Although the microscopic diagnosis method is widely used, its efficiency is low because it takes more time and depends on the interpretation of the specialist physician. [11]. Deep learning algorithms, which have been used in the field of computer vision recently, increase the efficiency of specialist physicians by making a significant contribution to the decision-making process in solving real-life problems. [12,13].

Many deep learning-based methods have been used in the literature on the detection and classification of the malaria parasite. In the study of detecting the malaria parasite using microscopic images, a new deep neural network model has been proposed to detect the malaria parasite falciparum. In this proposed model, the VGG model network and the support vector machine (SVM) were combined using transfer learning and a success accuracy of 93.13% was obtained [1].

In a deep learning-based automated malaria parasite detection study, a new model for diagnosing malaria using microscopic smear images is proposed. The proposed model detected the malaria parasite with an accuracy of 99.23%. In addition, both web-based and mobile-based applications have been developed to validate the model efficiency [14]. In the study of Masud et al., the performance of a special convolutional neural network model was evaluated using a cyclic stochastic gradient descent with an automatic learning rate finder to detect malaria. As a result of the evaluation, 97.30% accuracy was obtained from the best performing model [15].

In the study of Pattanaik et al., a computer aided diagnosis (CAD) system is recommended to identify the malaria parasite. The proposed CAD system was evaluated using the malaria parasite dataset and achieved 89.10% detection accuracy. In addition, 93.90% sensitivity and 83.10% specificity rates were obtained with this system [16]. Sriporn et al., used the Xception deep learning model to analyze malaria. Comparing this model with ResNet-50, Inception-V3, VGG-16, NasNetMobile and AlexNet models, 98.86% success accuracy was achieved [17].

In a different study, an image classification model using convolutional neural networks was developed to detect malaria parasites and an accuracy of 95% was achieved [18]. In another study detecting malaria parasite, the performances of single shot multiple box detector (SSD), faster regional convolutional neural network (Faster R-CNN) and RetinaNet models were evaluated and compared. As a result of the comparison, it was observed that the Faster R-CNN model achieved the best success accuracy, despite the longer training time compared to other models [19].

Sinha et al., a convolutional neural network model was proposed to reduce the time complexity in describing malaria. Sequential and ResNet deep learning algorithms are compared in this study, which uses the same data set as the proposed model. As a result of the comparison, the Sequential model achieved 98% success accuracy using training data, 96% success accuracy using validation data, and 96% success accuracy using test data. The ResNet model, on the other hand, achieved success accuracy of 96.50% using training data, 96.78% using validation data, and 97% using test data [20].

In this study, ResNet architectures were compared using a dataset with a total of 27558 red blood cell images from the National Library of Medicine [21] containing 13799 parasitized and 13799 uninfected to quickly classify the malaria parasite. As a result of the comparison, the best classification accuracy was obtained with ResNet-50 v2. The use of ResNet models with this data set

and especially the comparison of the ResNet model versions by applying them together makes an important contribution to the literature.

2. MATERIALS AND METHODS

2.1. Dataset and Preprocessing

In this study, a dataset with a total of 27558 red blood cell images containing 13779 parasitized and 13779 uninfected from the National Library of Medicine was used to classify the malaria parasite [21]. All images in the data set were re-labeled in the same class after they were converted to 96×96 pixels in gray color format. 90% of the total number of images in the data set was used for training and testing the models and 10% for validation. Of the total 24802 images allocated for training and testing the models, 80% were reserved for training and 20% for testing. The images of malaria parasitized and uninfected data in the data set are shown in Figure 1.

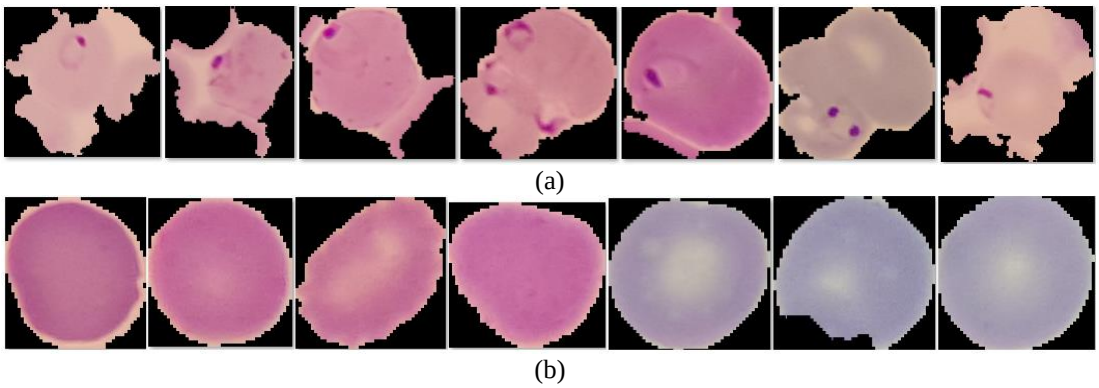

(a)

(b)

Figure 1. Dataset images (a) parasitized (b) uninfected.

2.2. ResNet Neural Network Models

ResNet is a classic neural network model introduced in 2015 to facilitate the training of deeper networks [22]. In the ResNet architecture, there are different model structures and versions. In this study, malaria parasite classification was performed using two different versions of the ResNet-50, ResNet-101, and ResNet-152 model structures. The diagram of ResNet models used in the classification of the malaria parasite is given in Figure 2. In addition, the traditional block structures used in the ResNet-50, ResNet-101, and ResNet-152 model structures are given in Table 1.

JSR A
Journal of Scientific Reports

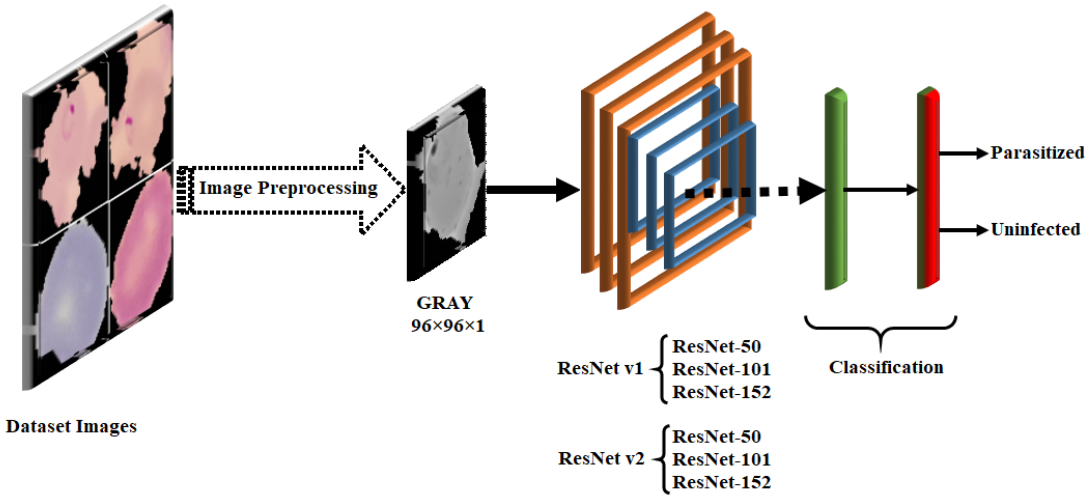

Figure 2. Model diagram used in the classification of malaria parasite.

Table 1. Traditional block structures used in ResNet model structures.

Layer Name	Output Size	ResNet-50	ResNet-101	ResNet-152
Conv1	96×96	7×7, 64, stride 2		
		3×3 max pool, stride 2		
Conv2	48×48	$\begin{bmatrix} 1\times1, 64 \\ 3\times3, 64 \\ 1\times1, 256 \end{bmatrix}\times3$	$\begin{bmatrix} 1\times1, 64 \\ 3\times3, 64 \\ 1\times1, 256 \end{bmatrix}\times3$	$\begin{bmatrix} 1\times1, 64 \\ 3\times3, 64 \\ 1\times1, 256 \end{bmatrix}\times3$
Conv3	24×24	$\begin{bmatrix} 1\times1, 128 \\ 3\times3, 128 \\ 1\times1, 512 \end{bmatrix}\times4$	$\begin{bmatrix} 1\times1, 128 \\ 3\times3, 128 \\ 1\times1, 512 \end{bmatrix}\times4$	$\begin{bmatrix} 1\times1, 128 \\ 3\times3, 128 \\ 1\times1, 512 \end{bmatrix}\times8$
Conv4	12×12	$\begin{bmatrix} 1\times1, 256 \\ 3\times3, 256 \\ 1\times1, 1024 \end{bmatrix}\times6$	$\begin{bmatrix} 1\times1, 256 \\ 3\times3, 256 \\ 1\times1, 1024 \end{bmatrix}\times23$	$\begin{bmatrix} 1\times1, 256 \\ 3\times3, 256 \\ 1\times1, 1024 \end{bmatrix}\times36$
Conv5	6×6	$\begin{bmatrix} 1\times1, 512 \\ 3\times3, 512 \\ 1\times1, 2048 \end{bmatrix}\times3$	$\begin{bmatrix} 1\times1, 512 \\ 3\times3, 512 \\ 1\times1, 2048 \end{bmatrix}\times3$	$\begin{bmatrix} 1\times1, 512 \\ 3\times3, 512 \\ 1\times1, 2048 \end{bmatrix}\times3$
	1×1	average pool, 2-d fc, sigmoid		

Except for Conv1 convolution block used in ResNet-50, ResNet-101 and ResNet-152 models, other convolution blocks consist of building blocks with 3 convolution layers as shown in Eq. 1.

$$\begin{bmatrix} 1 \times 1, 64 \\ 3 \times 3, 64 \\ 1 \times 1, 256 \end{bmatrix} \quad (1)$$

Therefore, the building block given in Eq. 2 is,

$$\begin{bmatrix} 1 \times 1, 64 \\ 3 \times 3, 64 \\ 1 \times 1, 256 \end{bmatrix} \times 3 \quad (2)$$

It consists of 3×3=9 convolution layers. Similarly, other convolution building blocks also include this convolution model [23].

ResNet architectures used in malaria parasite classification take the input image in gray color format and 96×96 pixels, and then a convolution layer with 64 2-step 7×7 filters is applied in the first convolution block (Conv1), which contains only one convolution layer. Then, a maximum pooling layer is applied with a 2-step and 3×3 pixel size filter and given as input to the second convolution block (Conv2), and it is followed by the third convolution block (Conv3), the fourth convolution block (Conv4), and the fifth convolution block (Conv5), respectively. Then, malaria parasite classification accuracy is obtained by using the sigmoid classification layer, which classifies as much as the number of classes specified in the data set from the features obtained from the average pooling and fully connected layer.

2.3. Model Training and Testing

5 K-Fold cross-validation was used to train the ResNet model structures used in the study. 19842 images are used for model training and 4960 images are used for model testing. In addition, after the training of the models, the model was validated with 2756 images separated from the data set to test the performance of the model structures. It is a difficult problem to process all the datasets to be used in training ResNet model structures at the same time. Therefore, the data set is divided into smaller groups using the Mini Batch Size parameter and the model networks are trained. However, during the training of the model networks, the epoch parameter is used to return all the data to the neural network. Adamax optimization algorithm is used to minimize the error of the model networks and increase their performance. Binary crossentropy loss function is used to determine the performance and error rates of the models. In addition, the sigmoid activation function is used to estimate the output from the model networks. The parameters and values used for training ResNet model structures are given in Table 2.

Table 2. Parameters used in ResNet model structures.

Parameters	**Values**
K-Fold	5
Mini Batch Size	64
Epoch	15
Optimizer	Adamax
Loss Function	Binary Crossentropy
Classifier Activation	Sigmoid

3. RESULTS AND DISCUSSION

In the study, malaria parasite was classified using versions of traditional ResNet models (ResNet-50 v1, ResNet-101 v1, ResNet-152 v1, ResNet-50 v2, ResNet-101 v2 and ResNet-152 v2). 5 K-Fold cross-validation was used to determine the validity and performance of model structures in malaria parasite classification. In Table 3, the loss values and accuracy rates obtained as a result of 5 K-Fold cross-validations of the models are given. In addition, the training-test accuracy graphs obtained as a result of training the ResNet models with the best performance are given in Figure 3 and the loss graphs are given in Figure 4.

Table 3. Loss values and accuracy rates obtained as a result of 5 K-Fold cross-validations of ResNet models.

Version	Models	Loss/Acc	Model 1	Model 2	Model 3	Model 4	Model 5
v1	ResNet-50	Loss	1.7374	2.2477	0.6678	5.6796	**0.2476**
		Acc (%)	56.42	53.22	78.41	50.00	**93.19**
	ResNet-101	Loss	**0.2004**	0.6429	0.2499	5.5997	1.6313
		Acc (%)	**93.73**	87.28	91.87	50.02	64.31
	ResNet-152	Loss	0.2755	0.7025	0.5807	0.2881	**0.2301**
		Acc (%)	90.04	74.66	79.70	91.23	**91.79**
v2	ResNet-50	Loss	1.2799	0.2701	**0.2623**	0.4078	0.3315
		Acc (%)	65.87	93.89	**93.23**	94.03	94.13
	ResNet-101	Loss	1.8249	0.3592	**0.3199**	1.1886	3.2701
		Acc (%)	65.77	92.40	**90.38**	73.45	54.03
	ResNet-152	Loss	0.3638	3.7516	**0.3132**	1.7687	0.5809
		Acc (%)	86.47	50.45	**92.40**	62.90	77.92

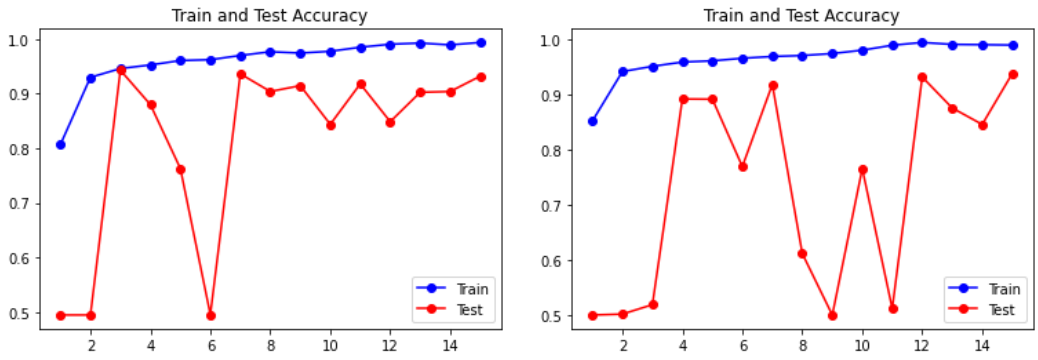

(a)

JSR A
Journal of Scientific Reports

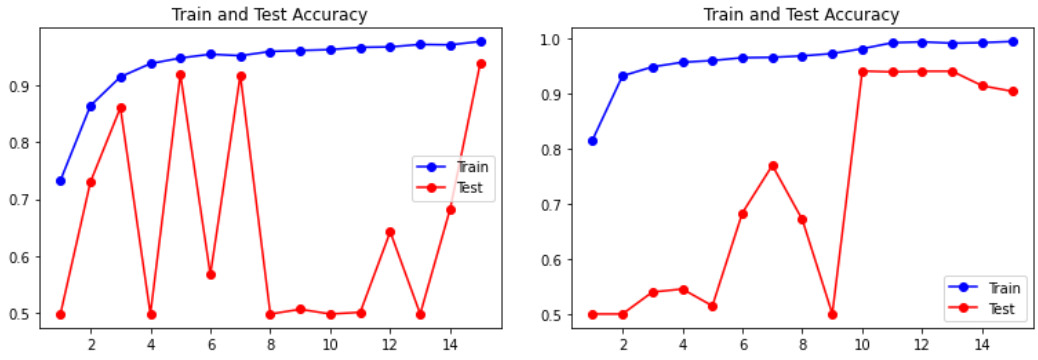

(b)

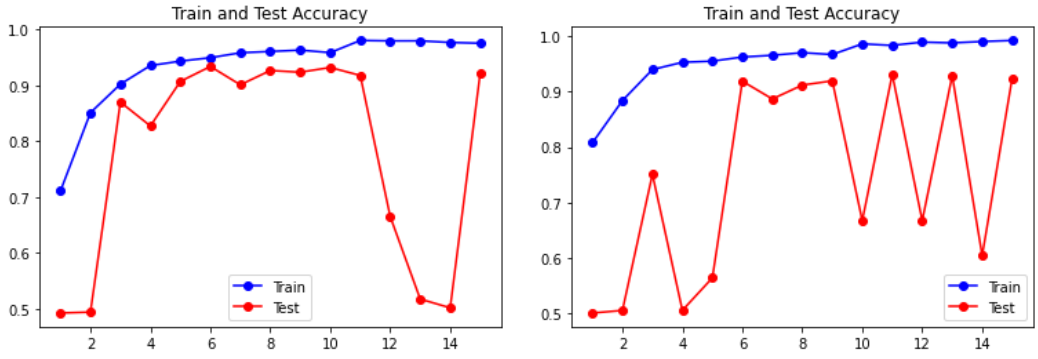

(c)

Figure 3. Training-test accuracy graphs of ResNet model structures (a) ResNet-50 v1 (left) – ResNet-50 v2 (right), (b) ResNet-101 v1 (left) – ResNet-101 v2 (right), (c) ResNet-152 v1 (left) – ResNet-152 v2 (right).

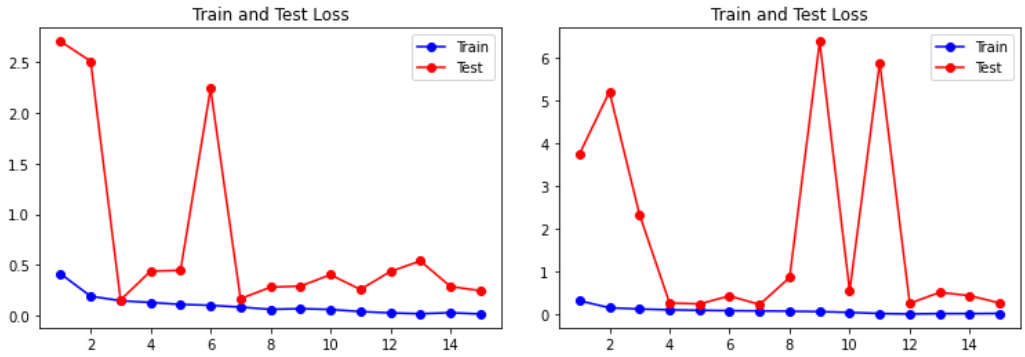

(a)

JSR A
Journal of Scientific Reports

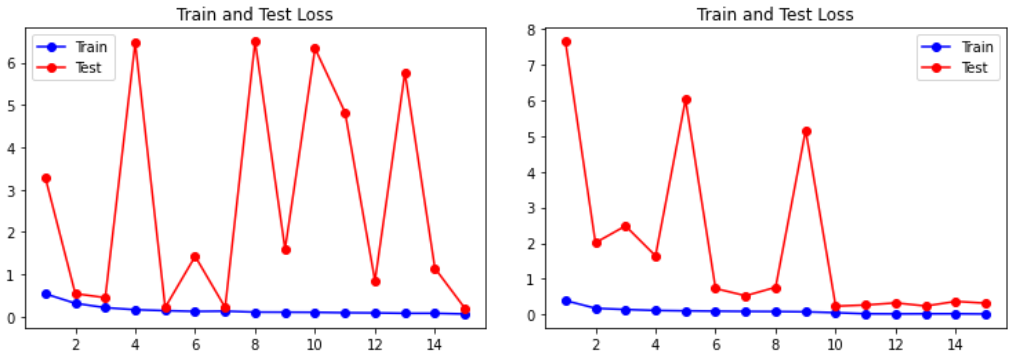

(b)

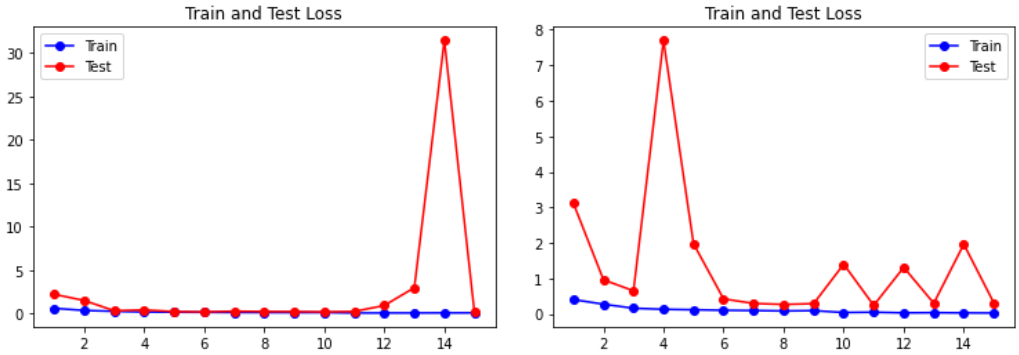

(c)

Figure 4. Training-test loss graphs of ResNet model structures (a) ResNet-50 v1 (left) – ResNet-50 v2 (right), (b) ResNet-101 v1 (left) – ResNet-101 v2 (right), (c) ResNet-152 v1 (left) – ResNet-152 v2 (right).

When Table 3, Figure 3, and Figure 4 were examined, it was seen that ResNet-101 v1 and ResNet-50 v2 were the models with the best training-test success in classifying the malaria parasite in ResNet model structures. The model with the worst training-test success was found to be ResNet-101 v2 and ResNet-152 v1.

Considering the rates in Table 3, the performance of the models was tested by choosing the best models with the lowest loss value as a result of the training of the models, and the results are given in Table 4.

To test the validity of the ResNet models that showed the best success as a result of the 5-K Fold, the model was validated using 2756 images separated in the dataset. The final test accuracy rates and loss values obtained for these models are given in Table 5 and the confusion matrix graphics are given in Figure 5.

Table 4. Performance measures of the models with the lowest loss value obtained as a result of 5 K-Fold cross-validations of ResNet models.

Version	Models	Class	Precision	Recall	F1-Score	Support
v1	ResNet-50	Parasitized	0.94	0.93	0.93	1407
		Uninfected	0.93	0.93	0.93	1349
	ResNet-101	Parasitized	0.95	0.93	0.94	1407
		Uninfected	0.93	0.94	0.94	1349
	ResNet-152	Parasitized	0.89	0.96	0.92	1407
		Uninfected	0.95	0.88	0.91	1349
v2	ResNet-50	Parasitized	0.95	0.94	0.94	1407
		Uninfected	0.93	0.95	0.94	1349
	ResNet-101	Parasitized	0.88	0.94	0.91	1407
		Uninfected	0.94	0.87	0.90	1349
	ResNet-152	Parasitized	0.93	0.92	0.93	1407
		Uninfected	0.92	0.93	0.92	1349

Table 5. The accuracy rates and loss values obtained using the validation dataset in the best.

Version	Models	Accuracy (%)	Loss
v1	ResNet-50	93.07	0.2568
	ResNet-101	93.83	0.2001
	ResNet-152	91.91	0.2338
v2	ResNet-50	94.09	0.2333
	ResNet-101	90.75	0.2999
	ResNet-152	92.53	0.2915

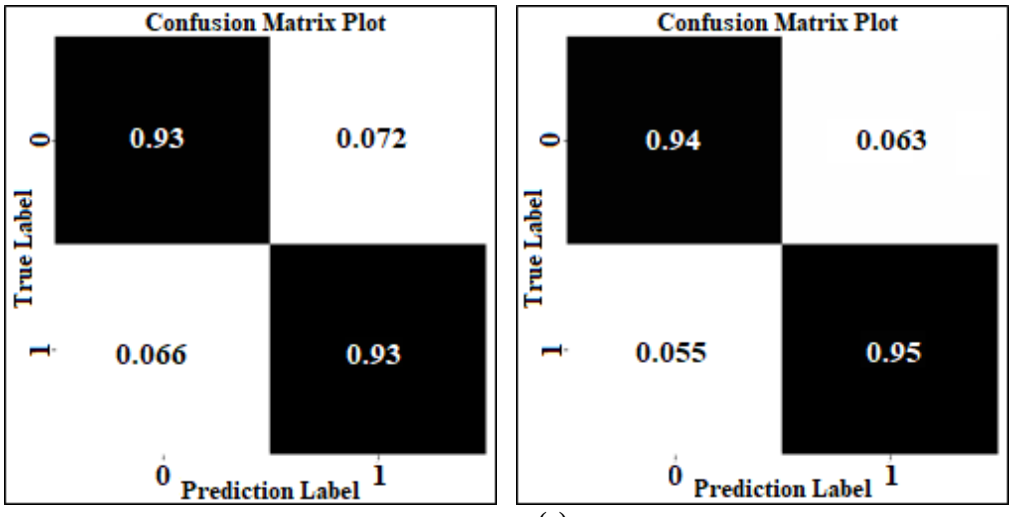

(a)

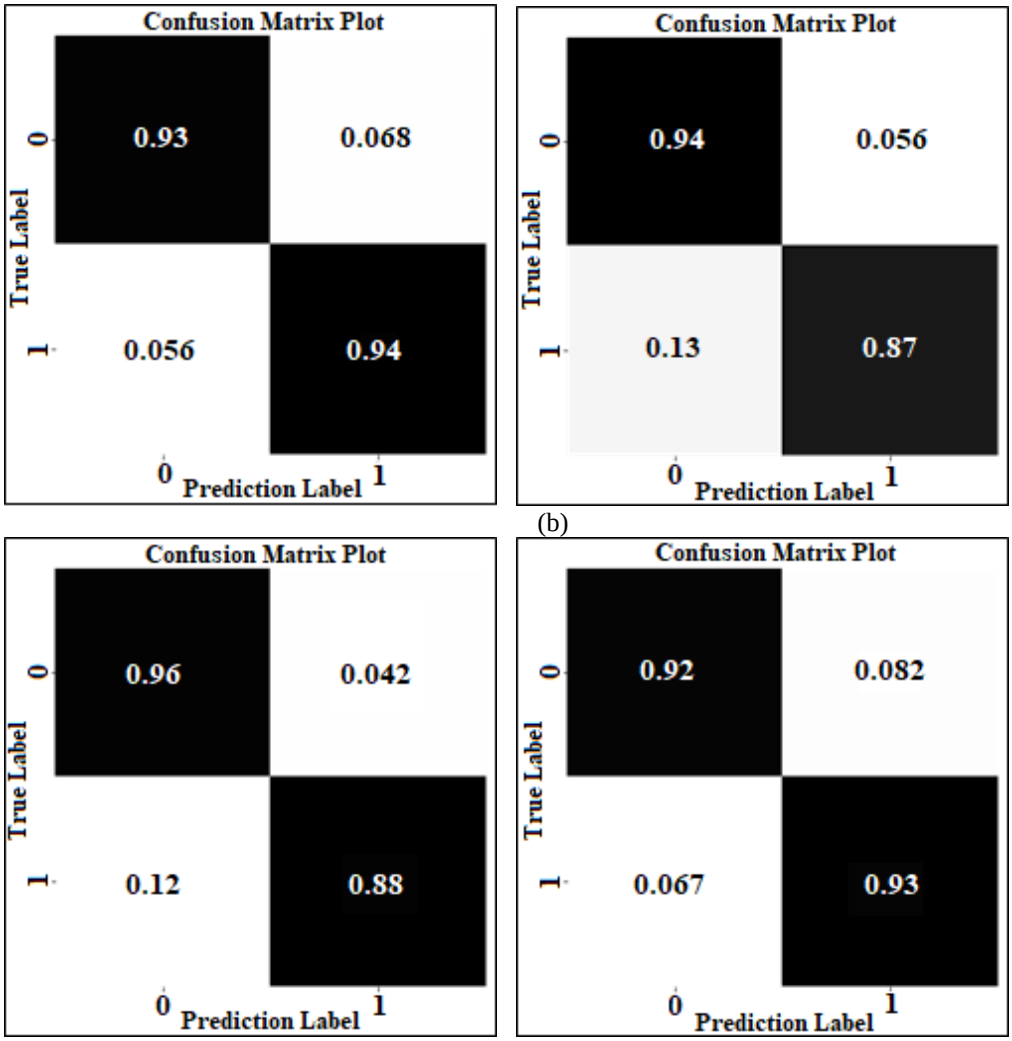

Figure 5. Confusion matrix obtained using the validation dataset in the best model (a) ResNet-50 v1 (left) – ResNet-50 v2 (right), (b) ResNet-101 v1 (left) – ResNet-101 v2 (right), (c) ResNet-152 v1 (left) – ResNet-152 v2 (right) (0: Parasitized, 1: Uninfected).

When Table 4, Table 5 and Figure 5 are examined, ResNet-50 v1 showed 93.07%, ResNet-101 v1 93.83%, ResNet-152 v1 91.91%, ResNet-50 v2 94.09%, ResNet-101 v2 90.75%, and ResNet-152 v2 92.53% success in classification of malaria parasite using the validation dataset. It was observed that the ResNet-50 v2 model with the least number of parameters reached the best success accuracy (94.09%).

4. CONCLUSIONS

In this study, ResNet-50 v1, ResNet-101 v1, ResNet-152 v1, ResNet-50 v2, ResNet-101 v2 and ResNet-152 v2 models from ResNet architectural structures were compared in classification of malaria parasite. The National Library of Medicine dataset consisting of 27558 red blood cell images was used to compare the models. 90% of the total number of images in the data set was used for training and testing the models and 10% for validation. The images separated for training and testing were trained separately using the 5 K-Fold cross-validation method.

The models were trained using the 5 K-Fold cross-validation method with the data in the training test dataset. The final test was conducted using the validation dataset on the best performing models from the trained models. It was seen that the best success accuracy among the models discussed in the study was obtained with the ResNet-50 v2 model with 94.09%. In conclusion, the results obtained with ResNet architectures are promising for the classification of malaria parasites in the field of medical imaging. In future studies, it is planned to carry out studies using different datasets and different model architectures in the field of health.

ACKNOWLEDGMENT

The authors thanks reviewers for their valuable comments and suggestions, which increased the clarity and the scope of the article.

REFERENCES

[1] Vijayalakshmi, A. And Rajesh, K.B., (2020), Deep learning approach to detect malaria from microscopic images, Multimedia Tools and Applications, 79(21), 15297-15317.

[2] Yang, F., Poostchi, M., Yu, H., Zhou, Z., Silamut, K., Yu, J., Maude, R.J., Jaeger, S. and Antani, S., (2019), Deep learning for smartphone-based malaria parasite detection in thick blood smears, IEEE journal of biomedical and health informatics, 24(5), 1427-1438.

[3] Diker, A.D., (2020), Sıtma Hastalığının Sınıflandırılmasında Evrişimsel Sinir Ağlarının Performanslarının Karşılaştırılması, Bitlis Eren Üniversitesi Fen Bilimleri Dergisi, 9(4), 1825-1835.

[4] Li, S., Du, Z., Meng, X. and Zhang, Y., (2021), Multi-stage malaria parasite recognition by deep learning, GigaScience, 10(6), giab040.

[5] Akılotu, B.N., Kadiroğlu, Z., Şengür, A. and Kayaoğlu, M., Evrişimsel Sinir Ağları ve Transfer Öğrenme Yöntemi Kullanılarak Sıtma Tespiti.

[6] Rahman, A., Zunair, H., Reme, T.R., Rahman, M.S. and Mahdy, M.R.C., (2021), A comparative analysis of deep learning architectures on high variation malaria parasite classification dataset, Tissue and Cell, 69, 101473.

[7] Chakradeo, K., Delves, M. and Titarenko, S., (2021), Malaria Parasite Detection Using Deep Learning Methods, International Journal of Computer and Information Engineering, 15(2), 175-182.

[8] Swastika, W., Widodo, R.B., Balqis, G.A. and Sitepu, R., (2021), The Effect of Regularization on Deep Learning Methods For Detection of Malaria Infection, In 2021 International Conference on Converging Technology in Electrical and Information Engineering (ICCTEIE), Bandar Lampung, 87-90.

[9] Yang, Z., Benhabiles, H., Hammoudi, K., Windal, F., He, R. and Collard, D., (2021), A generalized deep learning-based framework for assistance to the human malaria diagnosis from microscopic images, Neural Computing and Applications, 1-16.

[10] Swastika, W., Kristianti, G.M. and Widodo, R.B., (2021), Effective preprocessed thin blood smear images to improve malaria parasite detection using deep learning, In Journal of Physics: Conference Series, Malang, 1869(1), 012092.

[11] Imran, T., Sharif, M., Tariq, U., Zhang, Y.D., Nam, Y., Nam, Y. and Kang, B.G., (2021), Malaria Blood Smear Classification Using Deep Learning and Best Features Selection, Comput. Mater. Contin, 71, 1-15.

[12] Raj, M., Sharma, R. and Sain, D., (2021), A Deep Convolutional Neural Network for Detection of Malaria Parasite in Thin Blood Smear Images, In 2021 10th IEEE International Conference on Communication Systems and Network Technologies (CSNT), Bhopal, 510-514.

[13] Montalbo, F.J.P. and Alon, A.S., (2021), Empirical Analysis of a Fine-Tuned Deep Convolutional Model in Classifying and Detecting Malaria Parasites from Blood Smears, KSII Transactions on Internet and Information Systems (TIIS), 15(1), 147-165.

[14] Fuhad, K.M., Tuba, J.F., Sarker, M., Ali, R., Momen, S., Mohammed, N. and Rahman, T., (2020), Deep learning based automatic malaria parasite detection from blood smear and its smartphone based application, Diagnostics, 10(5), 329.

[15] Masud, M., Alhumyani, H., Alshamrani, S.S., Cheikhrouhou, O., Ibrahim, S., Muhammad, G., Hossain, M.S. and Shorfuzzaman, M., (2020) Leveraging deep learning techniques for malaria parasite detection using mobile application, Wireless Communications and Mobile Computing, 2020, 1-15.

[16] Pattanaik, P.A., Mittal, M. and Khan, M.Z., (2020), Unsupervised deep learning cad scheme for the detection of malaria in blood smear microscopic images, IEEE, 8, 94936-94946.

[17] Sriporn, K., Tsai, C.F., Tsai, C.E. and Wang, P., (2020), Analyzing Malaria Disease Using Effective Deep Learning Approach, Diagnostics, 10(10), 744.

[18] Shah, D., Kawale, K., Shah, M., Randive, S. and Mapari, R., (2020), Malaria Parasite Detection Using Deep Learning:(Beneficial to humankind), In 2020 4th International Conference on Intelligent Computing and Control Systems (ICICCS), Madurai, 984-988.

[19] Nakasi, R., Mwebaze, E., Zawedde, A., Tusubira, J., Akera, B. and Maiga, G., (2020), A new approach for microscopic diagnosis of malaria parasites in thick blood smears using pre-trained deep learning models, SN Applied Sciences, 2(7), 1-7.

[20] Sinha, S., Srivastava, U., Dhiman, V., Akhilan, P.S. and Mishra, S., (2021), Performance assessment of Deep Learning procedures on Malaria dataset, Journal of Robotics and Control (JRC), 2(1), 12-18.

[21] https://lhncbc.nlm.nih.gov/LHC-downloads/downloads.html#malaria-datasets

[22] He, K., Zhang, X., Ren, S. and Sun, J., (2016), Deep residual learning for image recognition. Proceedings of the IEEE Computer Society Conference on Computer Vision and Pattern Recognition, 2016-December, 770–778. https://doi.org/10.1109/CVPR.2016.90.

[23] Wu, H., Xin, M., Fang, W., Hu, H.M. and Hu, Z., (2019), Multi-level feature network with multi-loss for person re-identification, IEEE, 7, 91052-91062.

Kütahya Dumlupınar University
Institute of Graduate Studies

Journal of Scientific
Reports-A
E-ISSN: 2687-6167
Number 48, March 2022

RESEARCH ARTICLE

STUDYING the EFFECT of STIFFNESS VARIABILITY on SITE RESPONSE PREDICTION at LOTUNG SITE by EMPLOYING MODIFIED CAM-CLAY CONSTITUTIVE MODEL

Yusuf GÜZEL[1*]

[1]Necmettin Erbakan Üniversitesi, Mühendislik Fakültesi, İnşaat Mühendisliği Bölümü, 42500, Konya, yguzel@erbakan.edu.tr, ORCID: 0000-0003-2957-8060

Received Date:28.10.2021 *Accepted Date:22.02.2022*

ABSTRACT

Prediction of surface input motion is critical in seismic design of structures. Site response analysis through a Finite Element model can be useful in the prediction of surface input motion. The Finite Element modelling involves several uncertainties (e.g., shear wave velocity profile, shear strength, Standard penetration test values, friction angle) that will influence the predictions at the surface. This research considers the impact of shear wave velocity variability on the site response predictions under one strong and one weak input motions recorded at the Lotung site. The variability of shear wave velocity is characterized by means of Monte Carlo Simulations basing on the measured data at the site. Soil behavior is featured by Modified Cam-Clay model adapted in Finite element model, SWANDYNE. The results in terms of spectral acceleration, peak ground acceleration and shear strain profiles indicate that the stiffness variability can alter the predictions and level of this alteration depends strongly on the seismic intensity level of the input motion applied. The medians of Monte Carlo Simulation predictions are almost in line with the baseline predictions. In terms of spectral accelerations, the medians divert from the recorded data. In particular, when the strong input motion is applied, the predictions, at around the fundamental period of the soil deposit, are greater than the recorded ones. Nevertheless, the predictions express good indications to the actual values with respect to the peak ground acceleration and shear strain profiles and amplification factors.

Keywords: *Site response analysis, Stiffness variability, Monte Carlo Simulation, Spectral acceleration, Amplification factor*

JSR A
Journal of Scientific Reports

Güzel, Y., Journal of Scientific Reports-A, Number 48, 55-78, March 2022.

1. INTRODUCTION

Propagation of seismic waves through the soil deposits can greatly alter its characteristics at the surface (e.g. peak ground acceleration, PGA, peak ground displacement, PGD, peak ground velocity, PGV, bracket duration, fundamental period). This interaction between soil and seismic waves eventually influence the impact of earthquake events to the urban areas [1]. It is therefore in utmost importance to take into account main characteristics of earthquake events and soil deposits in seismic designs, in particular in seismically active regions.

One of the effective method to consider soil-seismic wave interaction is to simulate soil behaviour under earthquake input motions via analytical or numerical methods. While it is well-known that the analytical methods (e.g. EERA [2]) may lead to indicative predictions, they cannot be able to thoroughly replicate the real soil behaviours (i.e. capturing early soil nonlinearity, irreversibility, strain accumulations). In contrast, numerical methods (Swandyne [3], Plaxis [4], etc.) with soil models (Mohr-Coulomb, Modified Cam-Clay or some other advanced soil models) can be able to capture soil nonlinearity, permanent strain accumulations and built-up pore pressure. Besides, analytical methods require limited soil parameters, in use of numerical methods several sets of soil parameters may be needed, especially when advanced soil models are employed.

Main features of soil deposits, namely stiffness profile (maximum shear stiffness at minimal shear strain levels, G_{max} or shear wave velocity, V_s) and nonlinear curves or shear modulus degradation and related hysteretic damping (G/Go vs shear strain and D (%) vs shear strain) are two dominant factors in the alteration of seismic waves [5]. When the stiffness of soil deposits are measured via in-situ tests, such as cross-hole, down-hole, seismic cone, Spectral Aanalysis of Seimic Waves (SASW), suspension logging methods (e.g. [6, 7])). The nonlinear curves can be obtained up to a range of shear strains through laboratory testing of undisturbed soil samples (e.g. resonant column/torsional shear, cyclic triaxial and cyclic simple shear tests). The measured data from several studies shows that stiffness values and nonlinear curves for a site can indicate great variations, and therefore great uncertainty. For this reason, in the analysis of soil deposits these uncertainties should be taken into consideration in order to better assess the soil-seismic wave interaction. In this aspect, geotechnical arrays have become great tool in both obtaining the soil properties rigorously and analyzing the performance of the soil models by using the recorded data through the down-hole arrays. The sites instrumented by geotechnical arrays, as Gilroy, Treasure Island, Lotung and KiK-net down-hole arrays [8-12], have been focus of many studies in verification of the models and in better understanding the interaction between soil and the seismic input motions.

One way to include the variabilities is to conduct Monte-Carlo Simulation (MCS), by changing the stiffness values and nonlinear curves at each simulation within the level of variations. Li and Assimaki [13] conduct MCS at three well-investigated down-hole array sites located in the Los Angeles Basin. They use the synthetic earthquake records produced by Assimaki et.al. [14]. The results indicate that the influence of nonlinear curves variability shows huge dependency to the seismic intensity of the applied input motion, particularly in the case of soft soil profiles. In contrast, the uncertainty in stiffness demonstrates less dependency to the seismic intensity but more related to the stiffness contrast especially

at the near surface. Rathje et. al. [15] also perform MCS in equivalent linear site response analysis. In the study, along with the stiffness and nonlinear curve variabilities, the variability in the bedrock motion is considered as well. The variations of shear wave velocity profile and nonlinear curves are achieved by using the statistical model developed by Toro [16] and the model of Darendeli and Stokoe [17]. It is found that the inclusion of shear wave velocity variability causes the reduction in the median surface motions and amplification factors, pronounced strongly at periods less than the site period. Furthermore, variability of nonlinear curves has lesser impact on the surface motions. The study conducted by Guzel et. al. [18] also operates MCS for the geotechnical array site in Lotung by utilizing FE code with an advanced kinematic hardening clay model (Rouainia and Wood model [19]. The results point out that the influence of stiffness and nonlinear curve variabilities on the seismic motions depends strongly on the level of seismic motions applied. The importance of stiffness contrast near the surface on the prediction of spectral accelerations emphasized, too.

In this study, geotechnical array site in Lotung is taken into consideration. The well-documented soil deposit is modelled in a Finite Element (FE) code, Swandyne [3]. Modified Cam-Clay soil model [20] is used and only the variability of stiffness is considered via MCS with the same methodology applied in the study of Guzel et.al. [18]. One weak and one strong motions recorded along the geotechnical array at the site are simulated. Different level of stiffness variability (i.e., different level of standard deviation) is considered and their impact on the spectral accelerations, shear strain and PGA is plotted. The detail of the site and considered seismic input motions is given in the next section, followed by the introduction of stiffness variability and the result sections.

2. LOTUNG SITE AND INPUT MOTIONS

The geotechnical array formed in 1985 is located in Lotung, Taiwan. From 1985 to 1990, 30 input motions with low, moderate and high seismic intensities are recorded by accelerometers positioned at different depth of the array. The site consist of soil layers until the depth of around 47 m, sit on top of a Miocene basement. The soil deposit includes different sublayers; 17 m thick silty sand layer above a 6 m thick layer of sand with gravel resting on a stratum of silty clay interlayered by an inclusion of sand with gravel between 29 m and 36 m, as indicated by the SPT log profile reported in Fig. 1b. The level of water table is assumed to be 1 m depth below the ground surface [21].

One strong (LSST7) and one weak (LSST11) input motions are employed in order to study the effect of interaction between seismic intensity and the stiffness profile on the surface input motions. For brevity, only the East-West (EW) components of the earthquake recordings at 47 m depth are considered. Main characteristics of the earthquake events including magnitude, epicentral distance, and PGAs at the 47 m depth and at the ground surface are presented in Table 1 [6]. Corrected acceleration-time histories and corresponding spectral accelerations are plotted in Figure 2. As clearly seen, strong motion has seismic energy at long durations and thus at high periods while weak motion has relatively low energy and duration. This is typical features of strong and weak input motions. The frequency contents of earthquake input motions reflects the seismic waves within various frequencies and amplitudes. The strong input motion can have high amplitudes at lower frequencies when the weak input motion can have high amplitudes at lower frequency levels.

JSR A
Journal of Scientific Reports

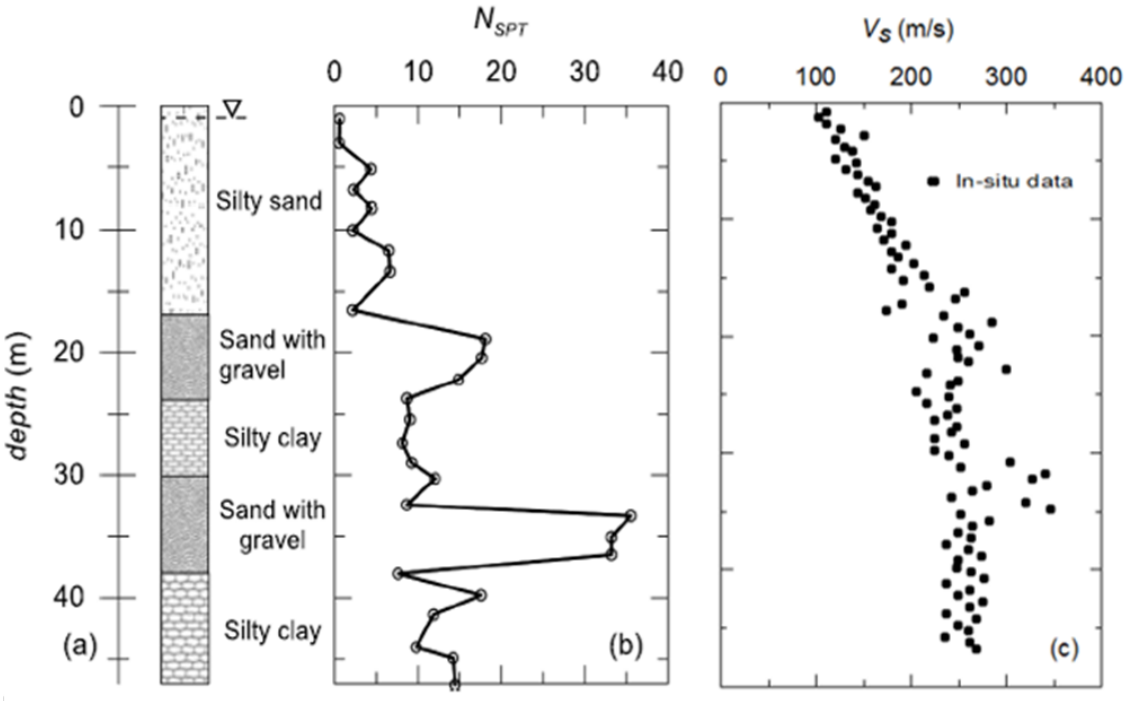

Figure 1. (a) Stratigraphy, (b) SPT log at the LSST site and c) measured shear wave velocity (V_s) profile along the depth of 47 m.

Table 1. Earthquakes recorded by the LSST array and simulated in the analyses [18].

Event	**Date**	**M_L**	**Epicentral distance (km)**	**Focal depth (km)**	**PGA (g) at 47 m depth**			**PGA (g) at the surface**		
					E-W	**N-S**	**V**	**E-W**	**N-S**	**V**
LSST07	20.5.1986	6.2	66.0	15.8	0.080	0.093	0.030	0.160	0.210	0.040
LSST11	17.7.1986	4.3	6.0	2.0	0.046	0.060	0.015	0.070	0.100	0.040

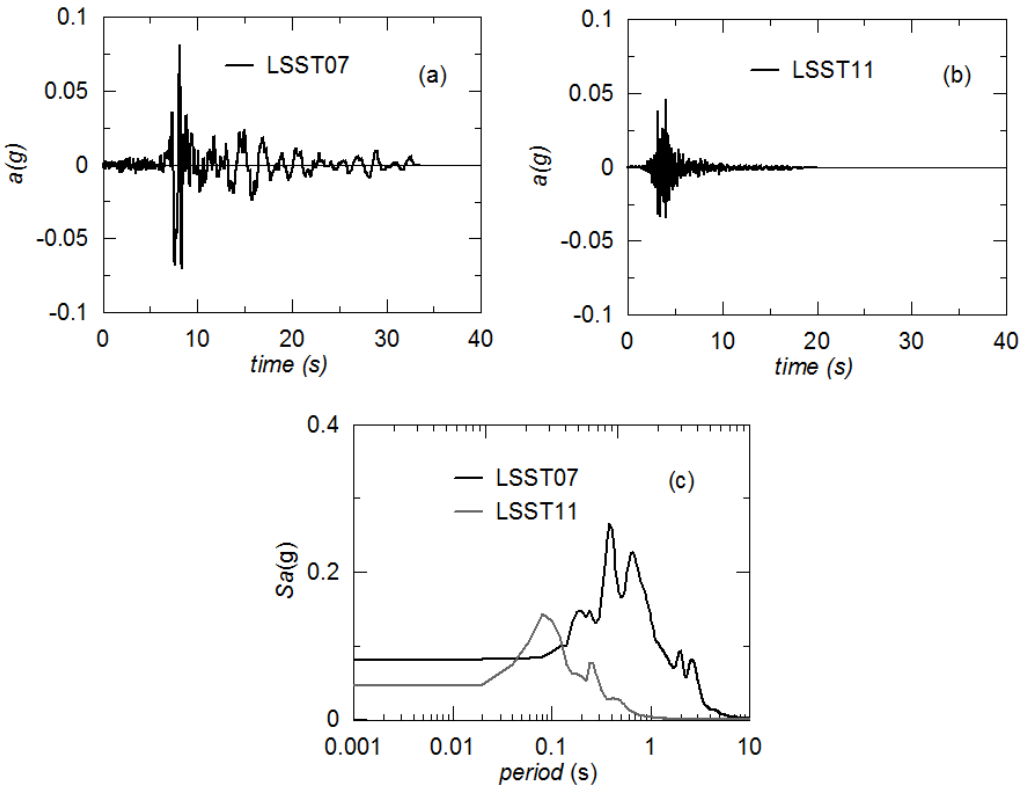

Figure 2. Recorded input motions at the Lotung site in the East-West (E-W) direction: (a) strong earthquake event (LSST7), (b) weak earthquake event (LSST11) and corresponding spectral accelerations.

3. SOIL PARAMETERS

The Modified Cam-Clay (MCC) model has been implemented in SWANDYNE II, which is a full-coupled finite element code solving the wave propagation problem in the time domain and enabling to model the soil deposit in two or three-dimensional spaces. Linear or nonlinear dynamic analyses can be performed, using the Generalised Newmark method [22] for time integration. Compression and swelling index parameters of the soil model, λ and κ, are obtained from odometer test results [6] as presented in Table 2. The value of Poisson's ratio is taken equal to 0.46 constant with depth due to the $K0$ value of 0.85, which is adjusted with respect to the predictions of the recorded pore water pressure during November 15, 1986 earthquake event (proposed by Li *et al.* [23] and Berger *et al.* [24]).. M, the slope of the critical state line, is calculated from friction angle predictions obtained from measured SPT-N values by using the following empirical formulation [25]:

$\emptyset_d=(20N)^{0.5}+18$ (1)

$M=6(\sin\emptyset-3)/\sin\emptyset$ (2)

In this study, the well-known equation proposed by Viggiani and Atkinson [26] for the small-strain shear modulus has been used to reproduce the dependency of G_0 on the mean effective stress and over-consolidation ratio:

$$\frac{G_o}{p_r} = A\left(\frac{p'}{p_r}\right)^n OCR^m \quad (3)$$

where p_r is a reference stress taken as 1 kPa, p' is mean effective stress, OCR is the over-consolidation ratio defined in terms of mean effective stress, A, m and n are the soil plasticity index (PI) dependent stiffness parameters. The best-fit G_0 profile in Figure 3a is achieved with A, m and n parameters shown in Table 2. In addition, OCR is considered 4 from 0 to 6 m depth and for the remaining soil profile a constant value of 2 is defined. These OCR values ensures that the calculated G_0 profile fits well with the G_0 values depicted from measured V_s values. 3% of Rayleigh damping is introduced in order to dissipate energy at the small strain levels as suggested by Kwok et.al. [26].

Table 2. Soil model parameters for different soil layers.

Depth	λ	κ	M	υ	A	m	n
0-17 m	0.0066	0.0015	0.922	0.46	1000	0.36	0.82
17-23 m	0.0066	0.0015	1.096	0.46	1900	0.36	0.82
23-29 m	0.0066	0.0015	0.814	0.46	1350	0.36	0.82
29-36 m	0.0066	0.0015	0.941	0.46	1900	0.36	0.82
36-47 m	0.0066	0.0015	0.730	0.46	1150	0.36	0.82

4. VARIATION IN THE INITIAL STIFFNESS PROFILE

The shear wave velocity values along the 47 m depth of the LSST site are attained from the in-situ test results (i.e. seismic cross-hole and up-hole tests) and presented in Figure 3. Recalling the Eq 3 adopted in the FE procedure for the small-strain shear modulus (G_0) profile of the Lotung site:

$$\frac{G_o}{p_r} = A\left(\frac{p'}{p_r}\right)^n OCR^m$$

For a soil layer, p', p_r and OCR are regarded as constant, only the A, m and n parameters are options for the variation of the stiffness. In this respect, m and n parameters are costumed as determinant with values of 0.36 and 0.82, respectively, given the reason that they have relatively narrow scale of values and, thus, has minor effect on the stiffness computation. Therefore, only the randomisation of A parameter is considered in producing stiffness profiles for the MCSs. In particular, a point variability is considered here, i.e. the initial stiffness profile is truncated from the baseline profile with the specified levels of standard deviation. Assuming the A parameter (and so the G_0 values) is lognormally distributed, reasonable fit with the measured values are attained for different soil layers, as shown in Figure 3a. Moreover, by using the lognormal distribution, stiffness values to being positive is assured [27]. The average G_0 profile with depth presented in Figure 3 represents the baseline profile used in the baseline predictions. It is important to note here that the formulation in randomization of the stiffness profile is the same with the one applied in the study of Guzel et.al. [18].

When only the A parameter is random, the mean and standard deviation of G_0 are:

$$\mu_{G_o} = \mu_A\left(\frac{p'}{p_r}\right)^n OCR^m$$

$$\sigma_{G_o} = \mu_A COV_A\left(\frac{p'}{p_r}\right)^n OCR^m \quad (4)$$

Since the stress and overconsolidation ratio dependency of G_0 is sustained in the calculation of the mean and standard deviation, the coefficient of variance (*COV*) of G_0 can be computed as:

$$COV_{G_o} = \frac{\sigma_{G_o}}{\mu_{G_o}} = COV_A \quad (5)$$

meaning that the *COV* is kept constant in the transformation of *A* into G_0.

After ensuring the consistency in the *COV*, it is necessary to calculate the statistical parameters of the lognormal distribution, e.g. the mean and standard deviation. The calculation of these parameters, along with the probability density function (PDF) of *A*, is given as:

$$A: \ln(\mu_{lnA}, \sigma_{lnA}) = exp(\mu_{lnA} + \sigma_{lnA} \times \xi) \quad (6)$$

where, $\xi \sim N(0,1)$ is a normally distributed random variable.

$$\mu_{lnA} = ln\left(\frac{\mu_A}{\sqrt{1+COV_A^2}}\right) \tag{7}$$

$$\sigma_{lnA} = \sqrt{ln(1+COV_A^2)}$$

Once the PDF expression of A (i.e. Eqç 6) is substituted into Eqç 3, G_0 can be written as follows:

$$G_o = exp(\mu_{lnA} + \sigma_{lnA}\xi)p'\left(\frac{p'}{p_r}\right)^n OCR^m \tag{8}$$

Reforming the expression given above:

$$G_o = \exp(\mu_{lnA} + (1-n)p_r + nln(p') + mln(OCR) + \sigma_{lnA}\xi) \tag{9}$$

From this formulation, the transformation of variability from A to G_0 only affects the mean of lnG_0 when a certain desired variability is given by the standard deviation [28]. Then, the log-normally distributed G_0 can be given as:

$$G_o : \ln\left(\mu_{lnG_o}, \sigma_{lnG_o}\right) \tag{10}$$

and:

$$\mu_{lnG_o} = \mu_{lnA} + (1-n)p_r + nln(p') + mln(OCR) \tag{11a}$$

$$\sigma_{lnG_o} = \sigma_{lnA} \tag{11b}$$

When, at the end of these steps, the G_0 profile is randomized, the variation in the associated V_s profile with depth is ensured with the assumption of a total unit weight of 20 kN/m^3 (as proposed by Borja *et al.* [29]). One single realisation of shear wave velocity profiles adapted in this research is demonstrated in Figure 3.

JSR A
Journal of Scientific Reports

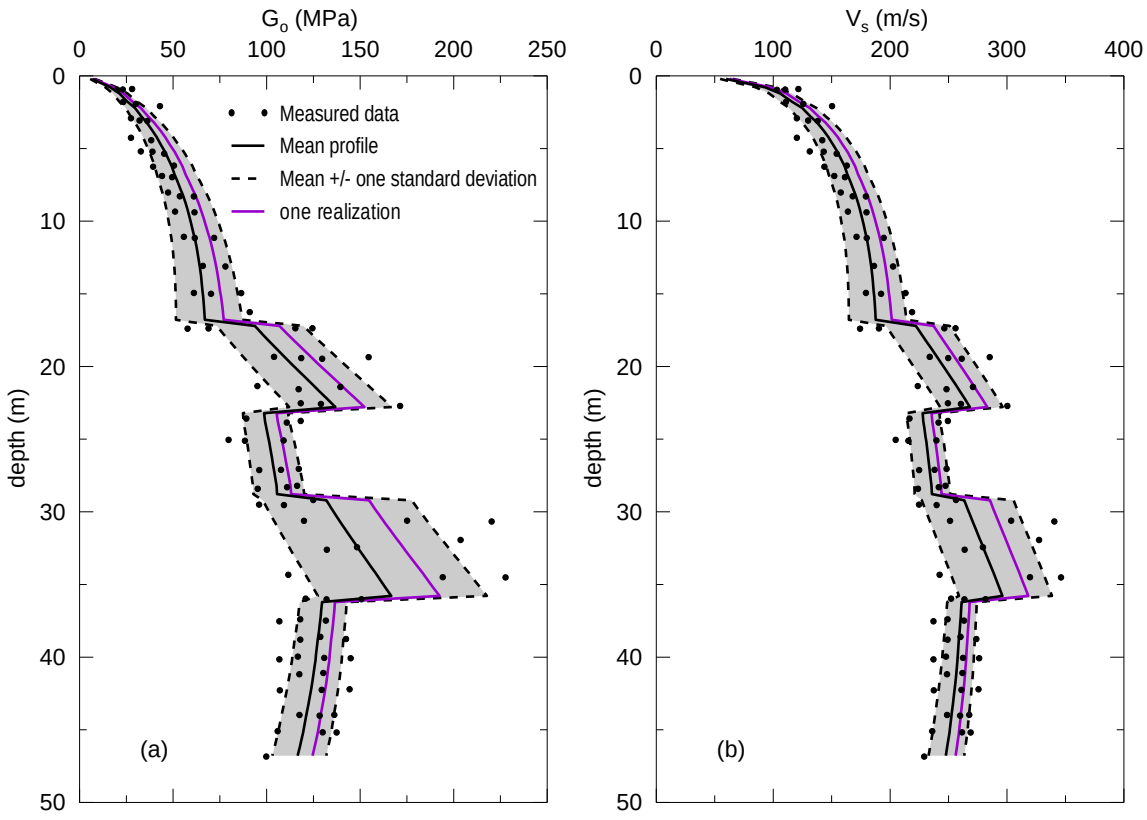

Figure 3. Point variability of stiffness: (a) shear modulus (G_0) profile and (b) shear wave velocity profile (V_s).

5. RESULTS

5.1. Influence of Stiffness Variability under Weak Input Motion

The spectral accelerations of recorded input motions at bedrock and ground level are plotted in Figure 4 along with the MCS their median and baseline responses. The presented baseline response is obtained by using the mean stiffness profile. 1_std, 2_std and 3_std truncations imply the results for V_s profiles produced within plus/minus one, two and three levels of standard deviation from the median profile.

It is clear that the actual bedrock input motion experience great amplification and period elongation due to soil nonlinearity when it travels through the surface. MCS results also exhibit considerable increase of

spectral accelerations at 1std, 2std and 3std truncation levels (Figure 4a, b, and c, respectively). While the first peak is reasonably well captured, the main peak occurring around the fundamental period of the soil deposit (i.e., T_1, equals to 0.85 second) is taken place at earlier periods. Nevertheless, in all cases predicted Sa between 0 and 0.12 period ranges overlaps almost fully with the recorded values. At medium period ranges (between 0.12 s and 1 s), baseline prediction and MCS predictions are bigger than the recorded ones. Over 1 s, predictions are always smaller than the actual spectral accelerations.

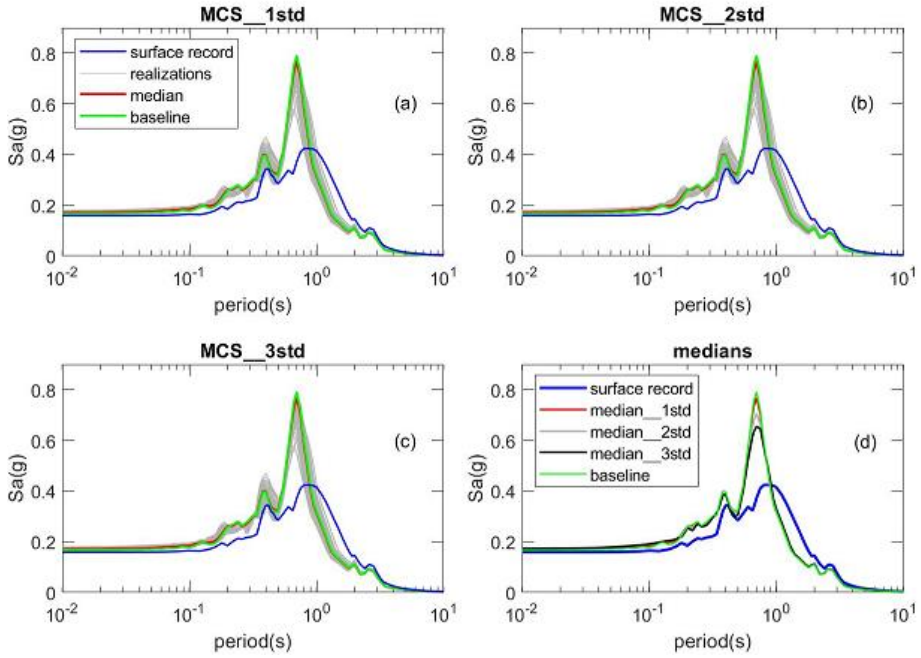

Figure 4. Spectral acceleration predictions from MCSs, under LSST7EW earthquake input motion, along with median, baseline and surface and bedrock input motions with; (a) 1std level of truncation, (b) 2std level of truncation and (c) 3std truncations and (d) comparison of medians from three cases of truncation.

Variation in the spectral acceleration predictions are mainly happen at 0.12 s and 2.5 s period interval, while at lower and higher periods seems to be insignificant in all truncation levels observed. Introduction of stiffness variability causes inconsiderable changes in the median spectral response when 1std level of truncation is considered (Figure 4d). In contrast, when 2 or 3std levels of truncation are utilized, predicted median spectral response reduces, in particular at around T_1. This can be attributed to the fact that the impact of soil behaviour on the input motion is pronounced more at T_1. Because, the soil deposit tends to oscillate more at its period ranges, therefore the stiffness variability leads to more changes within that period ranges in spectral acceleration predictions than at other periods. This can be seen in the lognormal standard deviation levels of MCS predictions (the reason in considering lognormal standard deviation is

spectral acceleration at a single period is considered to be lognormally distributed as stated by Assimaki et.al. [5].

As can be seen in Figure 7, the levels of standard deviation at around T_1 are higher than at other periods in all three cases. Besides, increasing the level of truncation from 1 to 3std, as expected, introduces more uncertainty, since the standard deviation at all periods become higher with the increment of truncation level (Figure 7a). The maximum standard deviation is 0.14 when the stiffness is varied at 1std level of truncation while it is 0.22 and 0.29 in 2std and 3std levels of truncation, respectively. Figure 5 and 6 values. demonstrate the PGA and shear strain profiles of MCSs along 47 m depth, respectively). It is clear that the predicted PGA values are bigger than the recorded ones at 17 and 11 m depths. At 6 m and at the surface they are relatively matched well in all three truncation levels. Increasing the level of truncation from 1std to 2std and 3std has small effect on the predicted median profiles of PGA (Figure 5d and Figure 6d) and shear strain but only introduce more variability as it leads to increase in the level of standard deviations (Figure 7b and 7c). In addition, median profiles of PGA and shear strain are in good agreement with the baseline predictions, especially at the near surface. From both PGA and shear strain profiles, different soil layers, characterised by different stiffness values, can easily be recognised. As the sand layers with gravel include relatively greater shear wave velocity, higher level of PGA and shear strains are developed. However, within these soil layers greater level of uncertainty is observed, in particular at the borders of the layers exhibiting dramatic changes of PGA and shear strain values. This may be attributed to the level of stiffness contrast between soil layers. While within a soil layer there is a tendency in both PGA and shear strain profiles showing smooth increments, the transition from one oil layer to another express large changes of PGA and strain. This becomes more explicit with the increment of the truncation levels.

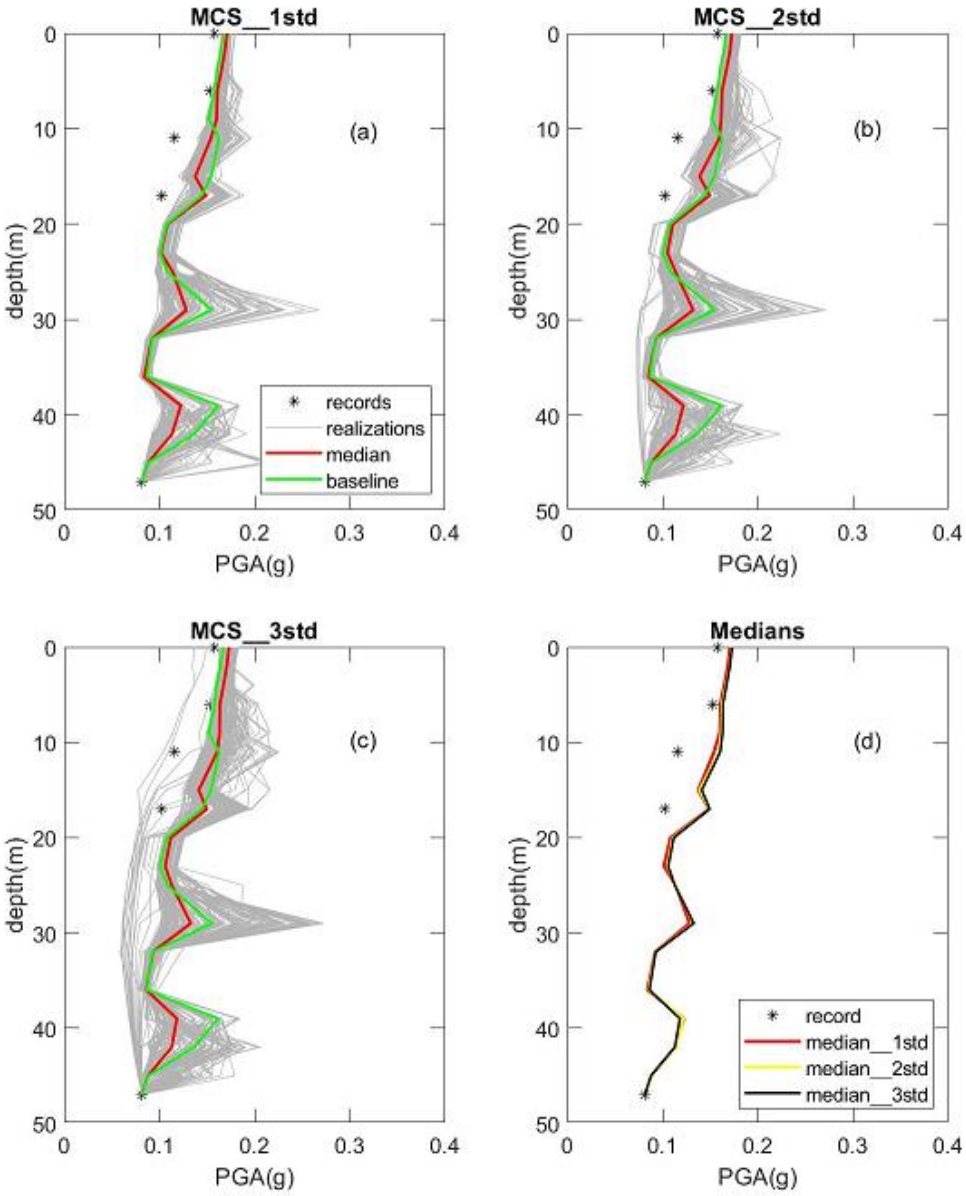

Figure 5. PGA profiles from MCSs, under LSST7EW earthquake input motion, along with median, baseline and recordings with ; (a) 1std level of truncation, (b) 2std level of truncation and (c) 3std truncations and (d) comparison of medians from three cases of truncation.

JSR A
Journal of Scientific Reports

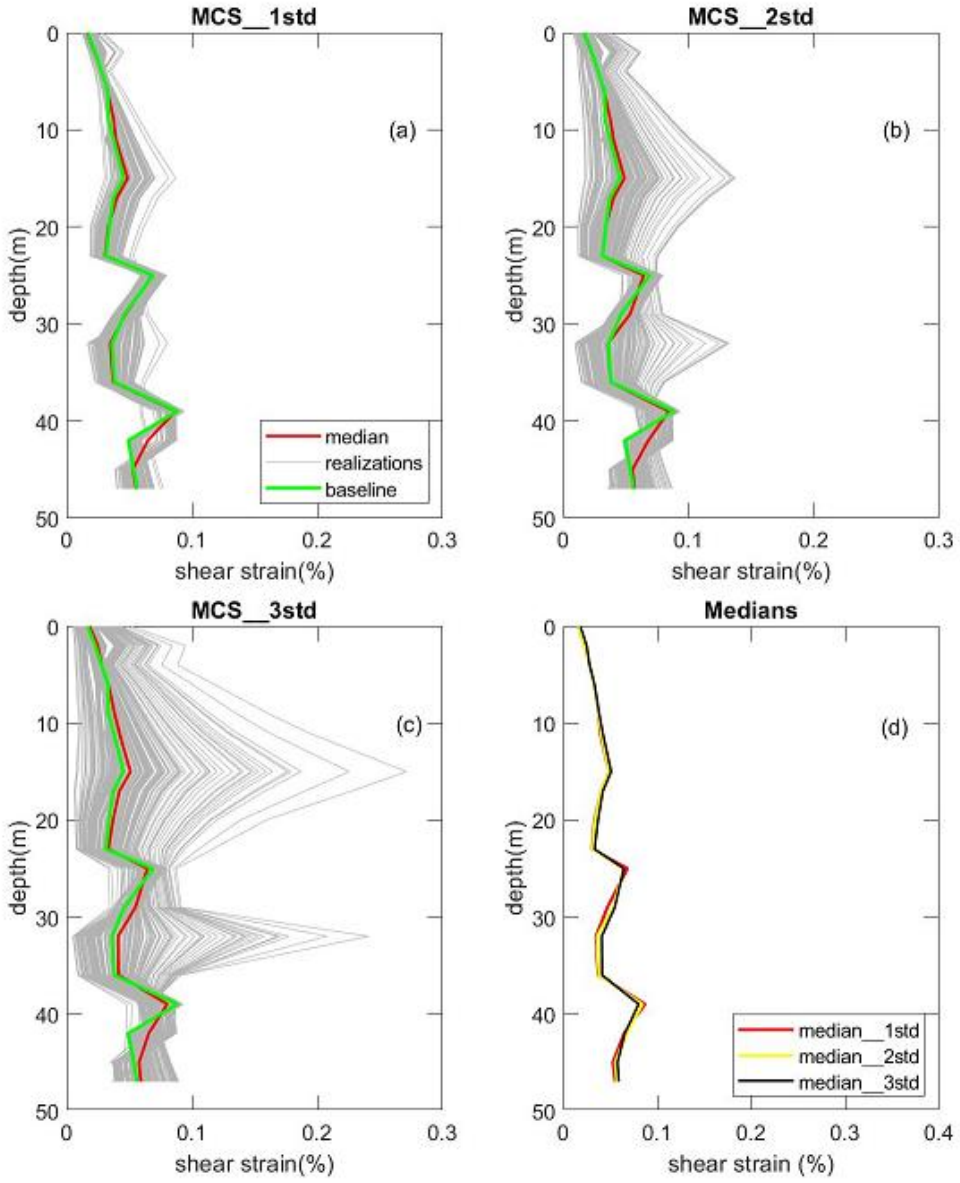

Figure 6. Shear strain profiles from MCSs, under LSST7EW earthquake input motion, along with median and baseline with ; (a) 1std level of truncation, (b) 2std level of truncation and (c) 3std truncations and (d) comparison of medians from three cases of truncation.

JSR A
Journal of Scientific Reports

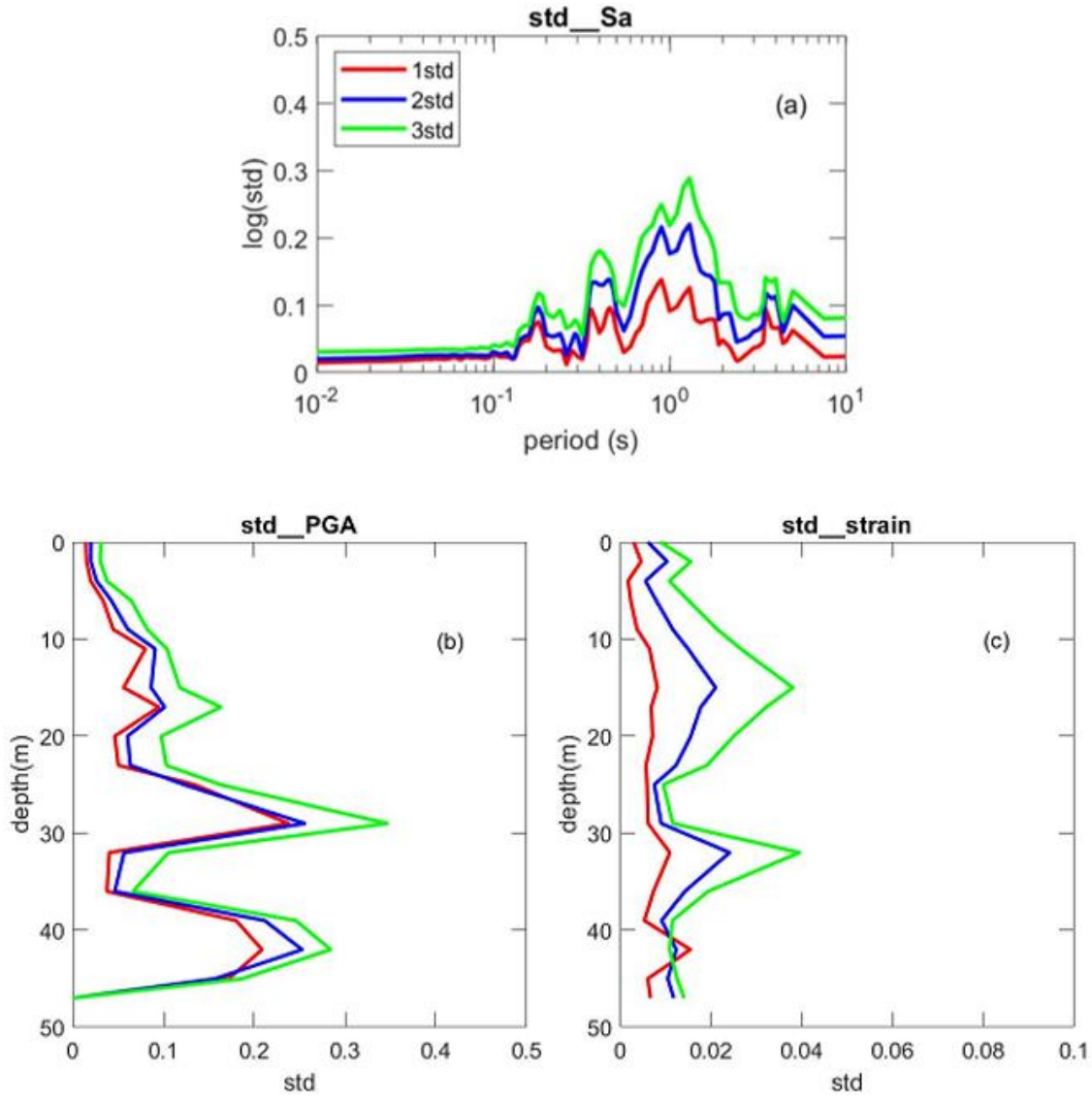

Figure 7. Level of standard deviations in three different truncation levels for; (a) spectral acceleration, (b) PGA profile and (c) shear strain profile predictions, under LSST7EW earthquake input motion.

5.2. Influence of Stiffness Variability under Weak Input Motion

In contrast to the strong input motion cases, where small effect of stiffness variability is observed at periods other than the 0.12 s and 0.25 s ranges, the stiffness variability tends to affect considerably the spectral accelerations at periods from 0 s to 1.6 s (Figure 8). Introduction of higher level of std (or truncation), leads to trivial changes in the median spectral accelerations until 0.2 s, where predicted values are always below the baseline and actual spectral accelerations, as can be seen in Figure 8d. From 0.2 s to 1.6 s, medians at three different truncation levels are always greater than the baseline and real spectral accelerations.

Increase of truncation levels from 1std to 2std and 3std, at this period range, causes medians to be closer to the real spectral accelerations while baseline prediction suits well with the actual ones. Again, the increase of truncation levels tends to raise the level of standard deviations of MCSs up to 1.6 s and above 2 s (see Figure 11a), between these two periods, the level of standard deviations induced by the level of truncation become mostly identical. In respect to the PGA and shear strain profiles, the medians of MCSs, presented in Figure 9 and 10, are almost the same at all three truncation levels and they are also in good agreement with the recorded PGA values at 17 m, 11 m, 6 m and at the surface level (Figure 9d and 10d). The rise in the level of standard deviations over the soil profile exhibit, similarly, rising trend of standard deviations for PGA, especially at the near surface as can be observed in Figure 9. This is due to the fact that the soil induces relatively greater nonlinearity at the near surface, hence the PGA values tends to show more sensitivity to the level of stiffness uncertainty. This is not valid for the shear strain profile as the standard deviation levels are similar from bottom to the 17 m depth (Figure 11c). At the top 17 m, 2std level of truncation expresses the least standard deviation; while it is lesser in case of 3std level of truncation than in case of 2std level of truncation.

It is important to note here that the soil layers are clearly differentiated between each other when the shear strain profiles are seen in Figure 10a-b-c, similar to the case under the strong input motion. However, the PGA profiles do not particularly show such trend as the PGA values along the soil deposit are smoothly transmitted from one layer to the other. This might be the indication of lesser effect of stiffness contrast on the PGA values when the weak input motion is involved.

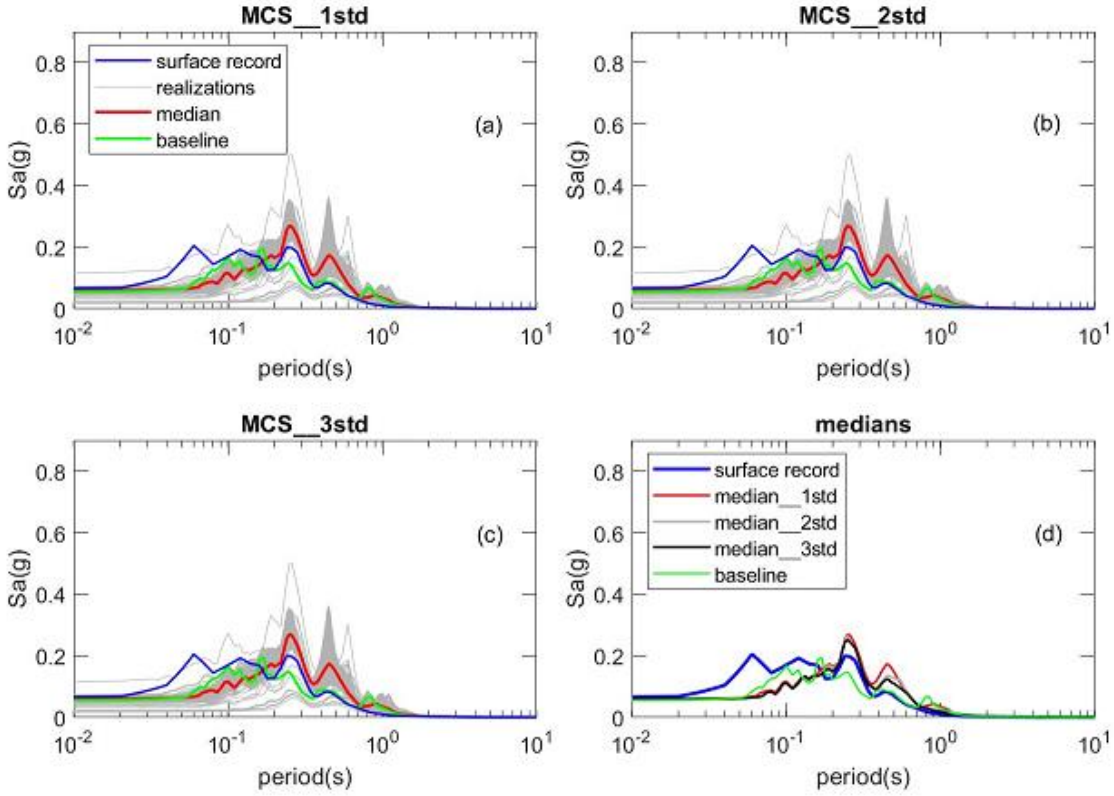

Figure 8. Spectral acceleration predictions from MCSs, under LSST11EW earthquake input motion, along with median, baseline and surface and bedrock input motions with; (a) 1std level of truncation, (b) 2std level of truncation and (c) 3std truncations and (d) comparison of medians from three cases of truncation.

JSR A
Journal of Scientific Reports

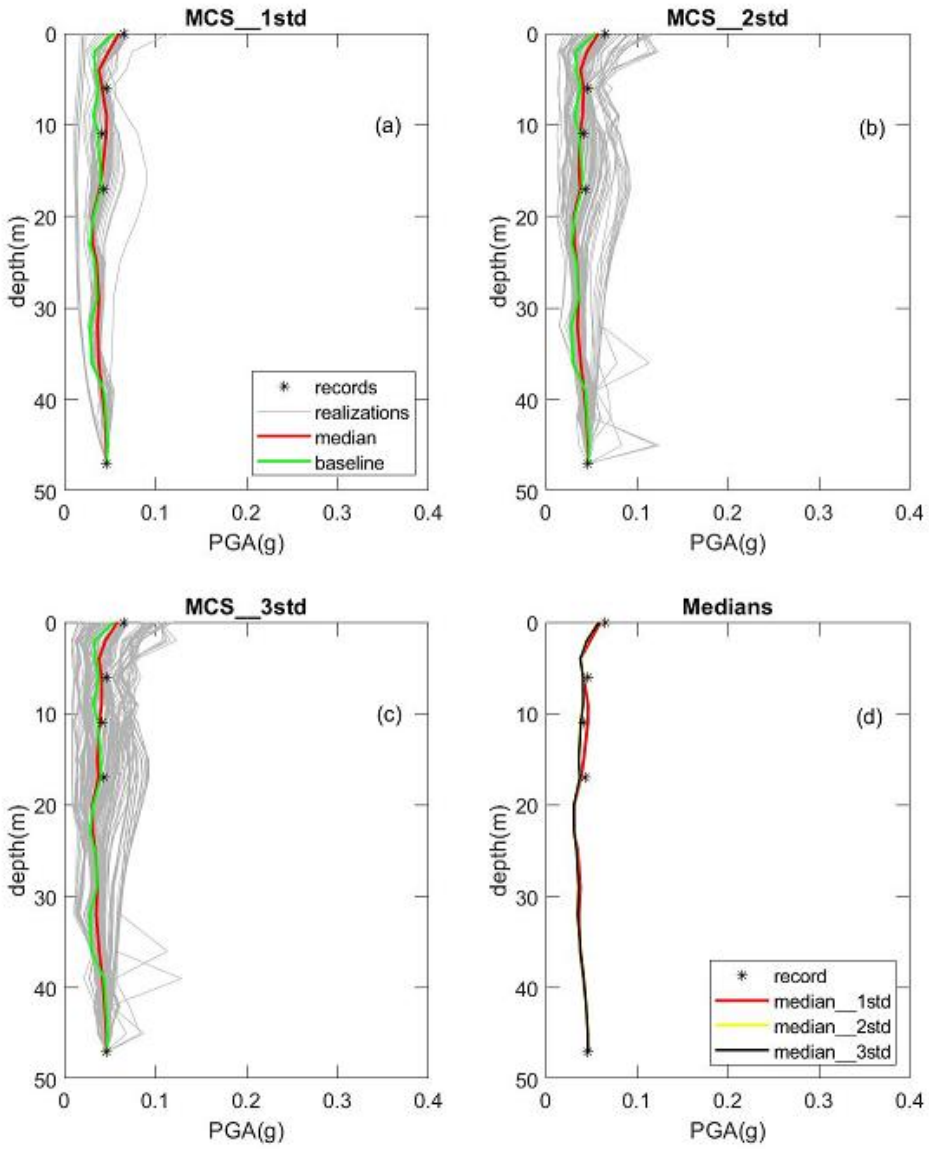

Figure 9. PGA profiles from MCSs, under LSST11EW earthquake input motion, along with median, baseline and recordings with ; (a) 1std level of truncation, (b) 2std level of truncation and (c) 3std truncations and (d) comparison of medians from three cases of truncation.

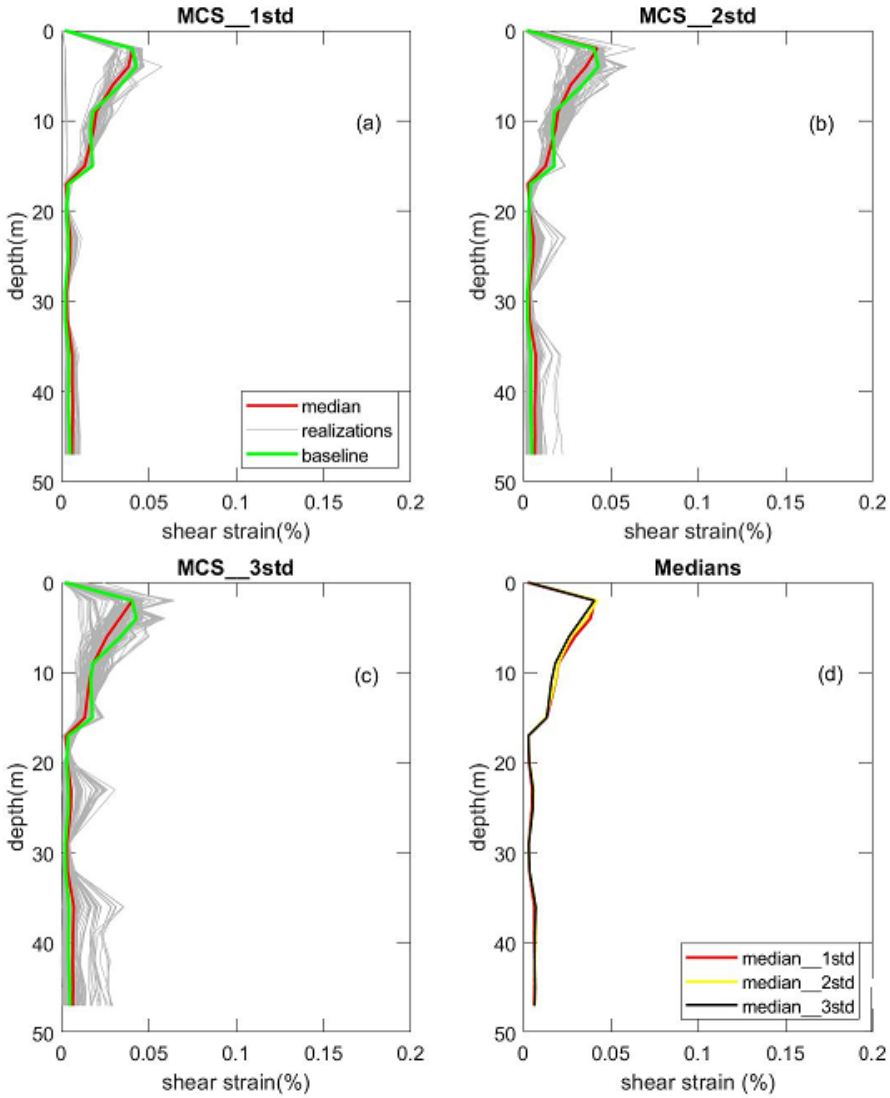

Figure 10. Shear strain profiles from MCSs, under LSST11EW earthquake input motion, along with median and baseline with ; (a) 1std level of truncation, (b) 2std level of truncation and (c) 3std truncations and (d) comparison of medians from three cases of truncation.

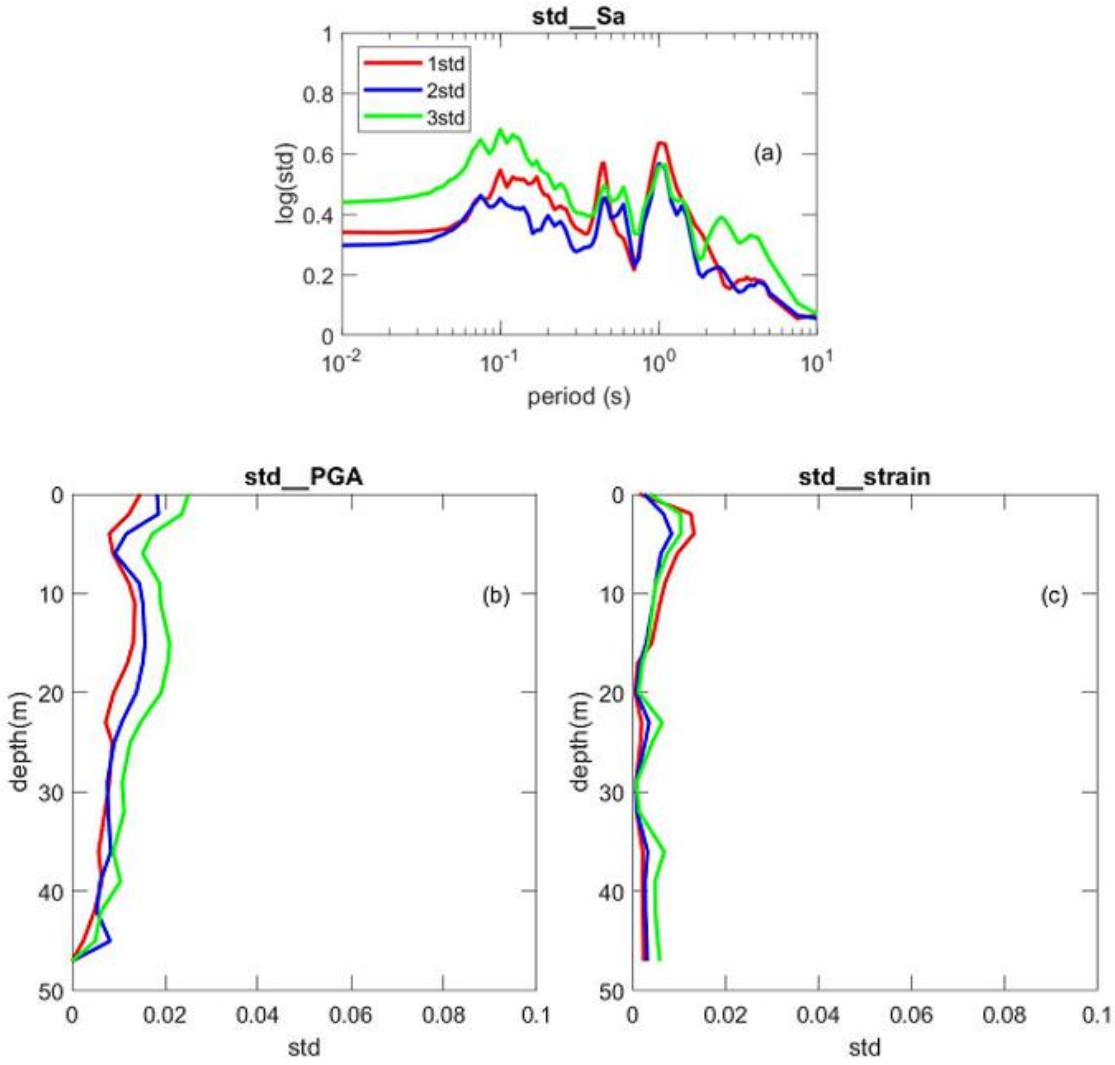

Figure 11. Level of standard deviations in three different truncation levels for; (a) spectral acceleration, (b) PGA profile and (c) shear strain profile predictions, under LSST7EW earthquake input motion.

5.3. Amplification Factors for Strong and Weak Input Motions

Amplification factor plots for medians of MCSs, baseline and actual one (under strong input motion) shows good agreement from 0 s to 0.18s while between 0.18s and 0.9s predicted values are almost

identical and higher than the actual values (see Figure 12a). Above 0.9 s, the trend inverses by predicted values becoming smaller than the actual ones. Amplification factors presented in Figure 12a for medians of MCSs and baseline profile cannot be able to capture the time of the spectral peak of strong input motion as it is previously observed in their spectral acceleration plots (i.e., Figure 4). Nevertheless, the magnitude of maximum amplification factors, from baseline profile, 1std and 2std truncation levels, agree well with the actual one, which is around 3.5 (Figure 12a). In the case of 3std truncation level, the value of maximum amplification factor is only 3.15.

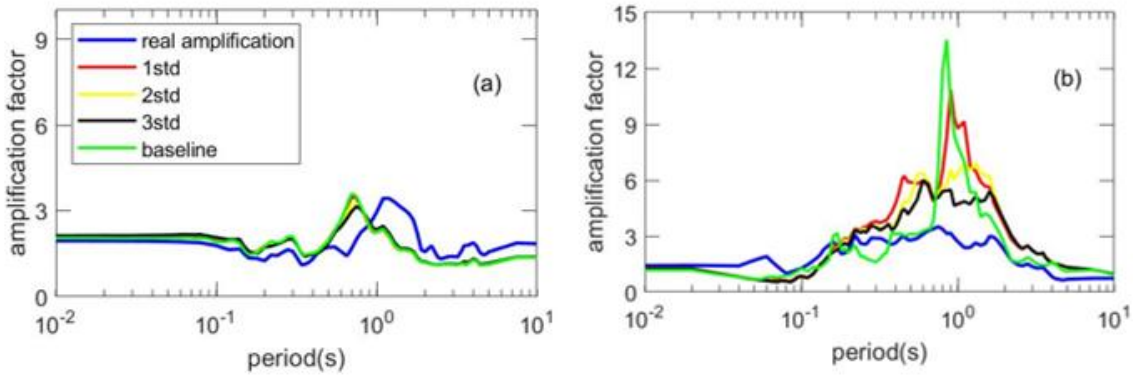

Figure 12. Comparison of amplification factors for medians of MCSs at three different level of truncations along with baseline and real amplifications over the period of interest under; (a) strong input motion (b) weak input motion.

Figure 12b represents the same plots under the weak input motion. When the real amplification factor plot is relatively smooth (due to characteristics of a weak motion carrying seismic energy at high frequencies), the ones for baseline and 1std truncation level have sharp spectral peaks with greater level of overestimations, precisely 3.51 for actual maximum amplification followed by 13.5 and 10.1, respectively. In case of 2 and 3std truncation levels, figures become smoother with the maximum magnitudes of 6.9 and 6, and get closer to the actual value of 3.51. Hence, it can be said that the increment in the level of truncation leads to better estimation of the spectral amplification, but still two times greater than the actual value.

6. CONCLUSIONS

This study focuses on the impact of stiffness (i.e., shear wave velocity) variability on site response predictions at the downhole array site in Lotung, Taiwan. Well-documented site is modelled within the FE model (SWANDYNE) by employing Modified Cam-Clay model. One strong and one weak input motions recorded at the bedrock level of the site are considered. Stiffness variability is introduced through the Monte Carlo Simulations based on the shear wave velocity data measured at the site. The spectral

accelerations and amplification factors at the surface, PGA and shear strain profiles are the interested results of discussions. The results can be outlined as followings;

- Stiffness variability shows considerable effect on the spectral acceleration predictions at around T_1 when the strong input motion is applied. In case of the weak input motion, such effect is observed over the ranges of periods. Therefore, the impact is dependent of the level of the input motion.

- Secondly, medians of MCSs under strong input motion does not clearly distinguish from each other and from baseline prediction, apart from around T_1. In addition, predicted spectral peaks occur at around T_1 and are greater than the actual peak. When the weak motion is in place, the medians are also closely matched.

- Increasing the level of truncation leads to more uncertainty but does not necessarily improves the results of spectral accelerations and PGA and shear strain profiles.

- While the effect of stiffness contrast between the soil layers are obvious in the case of strong input motion, such impact is not observed under the weak input motion.

- Predicted amplification factors indicate sufficient proxy to the actual one for the strong input motion. While this is not valid for the weak input motion, increasing the truncation level improves such prediction, though still not good enough.

Overall, the performance of MCC model is satisfying in the sense that it leads to good indication of spectral accelerations and, particularly, amplification factors. Involvement of stiffness variability through the MCSs is not necessary. Based on this study, further research is needed to characterize stiffness contrast between soil layers leading to better understanding of transformation of the input motions towards the surface.

ACKNOWLEDGEMENT

There is no funding body the author could acknowledge.

REFERENCES

[1] Ramos-Sepúlveda, M. E., & Cabas, A. (2021). Site Effects on Ground Motion Directionality: Lessons from Case Studies in Japan. Soil Dynamics and Earthquake Engineering, 147, 106755.

[2] Bardet, J.P., Ichii, K. and Lin, C.H. (2000). EERA: a computer program for equivalent-linear earthquake site response analyses of layered soil deposits. University of Southern California, Department of Civil Engineering.

[3] Chan, A.H.C. (1995). 'User's Manual for DIANA-SWANDYNE II. University of Birmingham, UK.

[4] Brinkgreve, R.B.J., Kumarswamy, S., Swolfs, W.M., Waterman, D., Chesaru, A. and Bonnier, P.G., 2016. PLAXIS 2016. *PLAXIS* bv, the Netherlands.

[5] Assimaki, D., Li, W., Steidl, J. and Schmedes, J. (2008). Quantifying nonlinearity susceptibility via site-response modeling uncertainty at three sites in the Los Angeles Basin. Bulletin of the Seismological Society of America, 98(5), 2364-2390.

[6] EPRI (1993). Guidelines for determining design basis ground motions-Volume 1: method and guidelines for estimating for estimating earthquake ground motion in Eastern North America. Rep. No. TR-102293. Palo Alto, California: Electric Power Research Institute.

[7] Kramer, L.S. (2014) *Geotechnical Earthquake Engineering*. Essex, England: Pearson Education Limited.

[8] Kaklamanos, J., Baise, L.G., Thompson, E.M. and Dorfmann, L. (2015). Comparison of 1D linear, equivalent-linear, and nonlinear site response models at six KiK-net validation sites. Soil Dynamics and Earthquake Engineering, 69, 207-219.

[9] Elia, G., Rouainia, M., Karofyllakis, D. and Guzel, Y. (2017). Modelling the non-linear site response at the LSST down-hole accelerometer array in Lotung. Soil Dynamics and Earthquake Engineering, 102, 1-14.

[10] Amorosi, A., Boldini, D. and di Lernia, A. (2016). Seismic ground response at Lotung: Hysteretic elasto-plastic-based 3D analyses. Soil Dynamics and Earthquake Engineering, 85, 44-61.

[11] Park, D., & Hashash, Y. M. (2004). Soil damping formulation in nonlinear time domain site response analysis. Journal of Earthquake Engineering, 8(02), 249-274.

[12] Darragh, R. B., & Idriss, I. M. (1997). A Tale of Two Sites: Gilroy# 2 and Treasure Island: Site Response Using an Equivalent-linear Technique. Earthquake Engineering Research Institute.

[13] Li, W., & Assimaki, D. (2010). Site-and motion-dependent parametric uncertainty of site-response analyses in earthquake simulations. Bulletin of the Seismological Society of America, 100(3), 954-968.

[14] Assimaki, D., Li, W., Steidl, J. and Schmedes, J. (2008). Quantifying nonlinearity susceptibility via site-response modeling uncertainty at three sites in the Los Angeles Basin. Bulletin of the Seismological Society of America, 98(5), 2364-2390.

[15] Rathje, E.M., Kottke, A.R. and Trent, W.L. (2010). Influence of input motion and site property variabilities on seismic site response analysis. Journal of Geotechnical and Geoenvironmental Engineering, 136(4), 607-619.

[16] Toro, G. R. (1995). Probabilistic models of site velocity profiles for generic and site-specific ground-motion amplification studies. Technical Rep. No. 779574. Brookhaven National Laboratory, Upton, New York.

[17] Darendeli, M.B., Stokoe, K.H. (2001). Development of a new family of normalized modulus reduction and material damping curves. Geotech. Engrg. Rpt. GD01-1. Austin: University of Texas.

[18] Guzel, Y., Rouainia, M. and Elia, G. (2020). Effect of soil variability on nonlinear site response predictions: Application to the Lotung site. Computers and Geotechnics, 121, 103444.

[19] Rouainia, M., & Muir Wood, D. (2000). A kinematic hardening constitutive model for natural clays with loss of structure. Géotechnique, 50(2), 153-164.

[20] Roscoe, K. and Burland, J.B. (1968). On the generalized stress-strain behaviour of wet clay.

[21] Anderson, D.G. and Tang, Y.K. (1989). Summary of soil characterization program for the Lotung large-scale seismic experiment. Proc. EPRI/NRC/TPC workshop on seismic soil-structure interaction analysis techniques using data from Lotung, Taiwan, EPRI NP-6154, 1, 4.1, 4.20. Palo Alto: Electric Power Research Institute.

[22] Katona, M.C. and Zienkiewicz, O.C. (1985). A unified set of single step algorithms part 3: The beta-m method, a generalization of the Newmark scheme. International Journal for Numerical Methods in Engineering, 21(7), 1345-1359.

[23] Li, X.S., Shen, C.K. and Wang, Z.L. (1998). Fully coupled inelastic site response analysis for 1986 Lotung earthquake. Journal of Geotechnical and Geoenvironmental Engineering, 124(7), 560-573.

[24] Berger E., Fierz H., Kluge D. (1989). Predictive response computations for vibration tests and earthquake of May 20, 1986 using an axisymmetric finite element formulation based on the complex response method and comparison with measurements-a Swiss contribution. In: Proceedings of the EPRI/NRC/TPC workshop on seismic soil-structure interaction analysis techniques using data from Lotung, Taiwan, EPRI NP-6154, vol 2, 15.1–15.47. Palo Alto: Electric Power Research Institute.

[25] Hatanaka, M. and Uchida, A. (1996). Empirical Correlation between Penetration Resistance and Internal Friction Angle of Sandy Soils. Soils and Foundations, 36(4), 1-9.

[26] Kwok, A.O., Stewart, J.P., Hashash, Y.M., Matasovic, N., Pyke, R., Wang, Z. and Yang, Z. (2007) Use of exact solutions of wave propagation problems to guide implementation of nonlinear seismic ground response analysis procedures. Journal of Geotechnical and Geoenvironmental Engineering, 133(11), 1385-1398.

[27] Andrade, J.E. and Borja, R.I. (2006). Quantifying sensitivity of local site response models to statistical variations in soil properties, Acta Geotechnica, 1(1), 3-14.

[28] Depina, I., Le, T.M.H., Eiksund, G. and Benz, T. (2015). Behavior of cyclically loaded monopile foundations for offshore wind turbines in heterogeneous sands. Computers and Geotechnics, 65, 266-277.

[29] Borja, R.I., Chao, H.-Y., Montáns, F.J. and Lin, C.-H. (1999). Nonlinear ground response at Lotung LSST site', Journal of Geotechnical and Geoenvironmental Engineering, 125(3), 187-197.

Kütahya Dumlupınar University
Institute of Graduate Studies

Journal of Scientific
Reports-A
E-ISSN: 2687-6167
Number 48, March 2022

RESEARCH ARTICLE

COLOR CHANGE of TURQUOISE-COLORED COPPER SILICATE MINERALS EXAMINED by CHEMICAL, PHASE and MICROSTRUCTURE ANALYSIS

Pelin Cağım Tokat-Birgin[1,*], Veli Uz[2]

[1]Kütahya Dumlupınar University, Faculty of Engineering, Department of Metallurgical and Material Engineering, pelincagim.tokat@dpu.edu.tr, ORCID: 0000-0001-9806-3381
[2]Kütahya Dumlupınar University, Faculty of Engineering, Department of Metallurgical and Material Engineering, veli.uz@dpu.edu.tr , ORCID: 0000-0003-2511-9326

Received Date:28.02.2022 *Accepted Date:23.03.2022*

ABSTRACT

In nature, copper silicate minerals generally have a turquoise color between the blue and green color spectrum. Turquoise color tones may vary depending on the stoichiometry and crystal structure in these minerals. In this study, the variation of color tones in copper silicate mineral with different turquoise colors was investigated. The causes of color change were investigated by chemical and mineralogical analyzes of copper silicate mineral in four different tones. Turquoise color becomes more vivid visually with increasing CuO and decreasing SiO_2 ratios. With changing stoichiometry, the crystal lattice parameters also change. The turquoise color of the minerals containing the highest (~16%) CuO and the lowest (~70%) SiO_2 has the best visual appearance compared to the others. For the same sample, the crystallite size was observed as 171 Å, which is the smallest crystallite size among the samples. In addition, SEM images and EDX analyzes of these samples were made and they were found to be consistent with mineralogical analyzes.

Keywords : *Copper Silicate, Turquoise, Color, Mineral.*

1. INTRODUCTION

Turquoise in copper silicate minerals can be considered as ornamental stones with their aesthetic structures. Turquoise color corresponds to different wavelengths between the blue and green spectrum [1]. The color tones of the turquoise copper silicate minerals found in nature also differ. Natural turquoise is a precious mineral known and used since early times with its unique color. The colors of the natural turquoise mineral can vary according to the elements it contains and their ratios. It is generally turquoise blue and bluish green in nature. Turquoise has a distinctive color. Its general formula is $CuAl_6(PO_4)_4(OH)_8.4(H_2O)$. It contains about 10% CuO and 35% P_2O_5, 38% Al_2O_3 [2].

Some minerals with similar color but with a totally different chemical composition are often mistaken for turquoises. This is the case of chrysocolla ($Cu_2.Alx(H_2xSi_2O_5)(OH)_4.nH_2O$ with $x < 1$), a hydrated copper silicate and, more recently, faustite ($((Zn,Cu)Al_6(PO_4)_4(OH)_8.4H_2O$) and blue prosopite ($(Cu, Al_2)(F,OH)_8$ [3-4].

Chrysocolla, a turquoise- like mineral, is harder than turquoise. The general formula of Chrysocolla can be defined as $(Cu, Al)_2 H_2 Si_2O_5 (OH)_4 \bullet n(H_2O)$ [5].
In turquoise structure, iron ions show antiferromagnetic behavior at low temperatures and copper ions show paramagnetic behavior. In many turquoise structures, Fe^{2+} instead of Cu^{2+} and Fe^{3+} instead of Al^{3+} occur at varying rates. The characteristic spectrum and basic color (light blue) of turquoise is related to the presence of octahedral iron [6].

Crespo-Feo et al. determined the cathodoluminescence and thermoluminescence properties of turquoise. They stated that they gave weaker band emission between 260-650 nm and 750 nm in dense wide scattering in bulk samples. At the same time, they determined that there are apatite, monazite and xenotime minerals in the turquoise matrix [7].

Huifen et al. studied the magnetic properties, characteristic spectrum and color tones of turquoise. The basis of the studies is based on chemical data, magnetic susceptibility, absorption and Mössbauer spectrum. In their studies, it has been determined that the basic color of turquoise (light blue) is due to the presence of octahedral iron [8].

Three types of mechanisms work in the color change of minerals. These, molecular orbital transitions, crystal area and atomic point faults called color center are the main reasons for the formation of mineral colors. There are color changes during the production of turquoise colored ornamental stones produced synthetically, which spoils the aesthetic feature. For this purpose, turquoise colored copper silicate minerals found in Turkey were selected and separated according to different tonal colors and the factors causing color differences were investigated. In this study, natural turquoise was characterized as a preliminary research on the use of naturally occurring turquoise mineral as an alternative to synthetic pigment.

2. MATERIALS AND METHOD

The raw materials used in the study, copper silicate minerals, were obtained from Malatya Region in Turkey. Samples were separated by color and characterized. In order to determine the oxide content of the samples, chemical analyzes were carried out with PANalytical Brand AXIOS Model XRF device. Mineralogical content and phase analysis of the samples were made on the Rigaku X-ray Diffractometer model Rint 2000 device. Phase analysis was carried out at 30 kV and 15mA (Cu-Kα, λ=1,541 A^0, 2θ 5-70º, 2º/min.) conditions. In the analysis of XRD data for mineralogical and phase analysis, the JADE 6 software used with the device was scanned through PDF databases. For color measurements, measurements were made with the CIE system, which can quantitatively detect the differences in the material. Color analyzes of the samples were obtained by measuring L*, a*, b* values with a Konika Minolta 3600d spectrophotometer. The microstructural observations and qualitative chemical properties of samples were carried out using a field emission gun SEM (Zeiss Supra 50 VP) equipped with EDX system (Inca software), operated at 0-20 kV acceleration voltage under variable pressure without coating by using secondary and Back scattered electron imaging (SEI/BSEI) techniques.

3. RESULTS AND DISCUSSION

Photographs were taken to examine the color differences of the samples. The images of copper silicate minerals separated according to their colors are given in Figure 1. The samples are given in color

JSR A
Journal of Scientific Reports

order from dark turquoise to light turquoise in Figure 1a (sample name T1) and in Figure 1d (sample name T4), respectively.

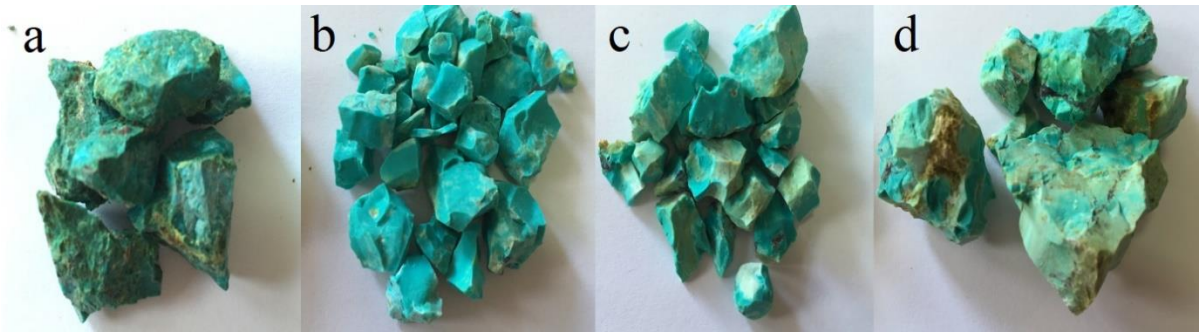

Figure 1. Copper silicate minerals listed according to their colors a) T1, b) T2, c) T3 and d) T4 sample.

Chemical analyzes of the samples were carried out in order to investigate the effect of chemical content on color change. The XRF analysis results of the samples are given according to their weight percent composition in Table1. SiO_2, CuO, MgO, CaO, Al_2O_3, Fe_2O_3 and PbO oxides were found in different proportions in all of the analyzed samples. From dark to light turquoise, the CuO ratios of the samples increased and SiO_2 decreased. Turquoise color changed according to copper oxide and silicon dioxide ratios. Turquoise colored samples vary between 6% and 16% CuO and 70% and 87% SiO_2 as the major oxide. The copper silicate mineral containing approximately 16% CuO and 70% SiO_2 has the most visually vivid turquoise color.

In the XRF analysis, it is seen that the Loss on ignition (LOI) in the samples have a very important in the content of the materials. This indicates that one or more of the minerals in the raw material contain water. The amount of LOI is lowest in T1, higher in T2, T3, and highest in T4 sample, respectively. This situation indicates that the mineral content of the T4 coded sample is the highest and the mineral content of the T1 sample is the lowest.

Table 1. Chemical analysis of turquoise colored minerals.

Sample No.	Oxide Ratios by Weight (%)							
	SiO_2	CuO	MgO	CaO	Al_2O_3	Fe_2O_3	PbO	LOI
T1	86.73	5.62	0.32	0.42	0.20	1.33	0.10	5.28
T2	80.06	11.40	0.28	0.22	0.23	0.60	0.04	7.17
T3	75.85	14.59	0.22	0.23	0.13	0.43	0.03	8.52
T4	69.49	15.60	0.34	0.57	0.14	0.50	0.10	14.01

L.O.I: Lost on ignition

X-Ray analysis was performed and the Rietveld method was used to determine the crystal parameters of copper silicate minerals. X-ray diffractograms of the samples are given in Figure 2. In X-Ray diffractograms of copper silicate minerals from dark color to light color, broadening peaks in the form of amorphization and humpback were observed. It has been determined that the XRD peaks of T4, which has the best turquoise color vividness, are in the amorphous phase formation, and its 2Θ value

JSR A
Journal of Scientific Reports

is determined to widen the peaks between 20-27°. The peaks of T4 with turquoise color vividness are widened in the formation of amorphous phase and the peaks with two-theta value between 20-27°. The fact that the color of the same sample is more vivid is due to the higher ratio of dioptase and chrysocolla phases, which have amorphous-glassy structure. When the XRD diagram of T4 sample is examined, it is seen that the ratio of copper silicate phases is higher than the other 3 samples. It can be interpreted that the peak intensity of these minerals is high, and the amount of phase is high. In addition, the high amount of LOI in the XRF data also showed that the amount of copper silicate phase was high. These datas overlap with XRF, spectrophotometer and other analyses.

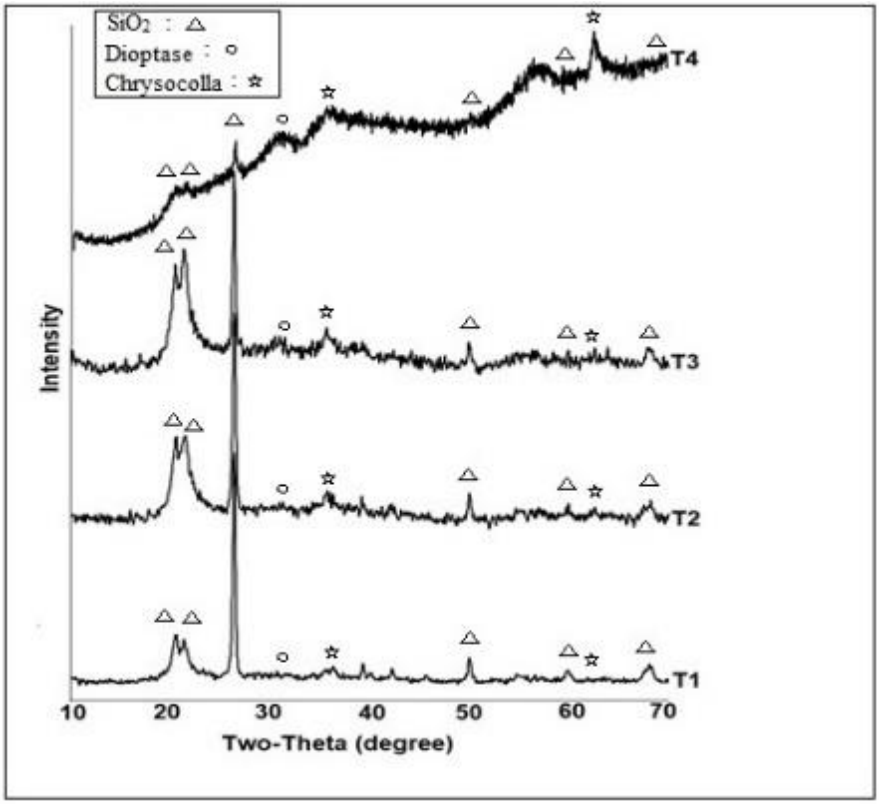

Figure 2. X-Ray diffractograms of minerals by color.

The lattice parameters calculated according to the Rietveld method are given in Table 2. The change rates of the smallest and largest axis values of the crystal parameters of the copper silicate minerals separated according to their colors were determined as 3.74% for the a-axis, 0.85% for the b-axis and 6.46% for the c-axis. The crystal parameters of T4, where the turquoise color is the most vivid, are at the highest values compared to the others. However, the crystallite sizes are the smallest with 170.76Å. The crystallite sizes decrease from about 746 Å to 171 Å from dark turquoise to light vivid turquoise. The color values of the samples were measured using a spectrophotometer and the obtained values are given in the same table (Table 2). In the system, which is defined as a three-dimensional coordinate axis, three values consisting of L* (brightness axis), a* (red-green) and b* (yellow-blue axis) were measured. The purpose of this analysis is to show by numerical measurement of color

JSR A
Journal of Scientific Reports

values that minerals have effective mechanisms such as absorbing certain energies of light or exposing them to direct emission, based on Kurt Nassau's work in 1978. In this way, it guides the determination of the change in the color values of atoms excited to high energy levels by the incoming light energy [9,10]. The crystal parameters of the T4, which have more vivid colors compared to the others, are larger than the others, and their color coordinates are at the highest values. The color differences of the samples, as well as shown in Figure 1, were also confirmed by spectrophotometer measurement.

Table 2. Lattice parameters and color values according to colors.

Sample No.	Crystal Parameters				Color Coordinates		
	a-axis	b-axis	c-axis	Crystallite Size	L*	a*	b*
T1	21.887	21.193	16.036	745.895	-76.19	-19.46	1.03
T2	21.936	21.144	15.962	415.827	-69.48	-16.76	5.40
T3	21.897	21.131	16.047	388.289	-67.65	-15.45	3.22
T4	22.705	21.310	16.993	170.76	-54.88	-14.79	6.77

In the chemical analyzes of copper silicate minerals in four different turquoise tones, CuO increases while SiO_2 decreases. Microstructure examinations of the same samples were made and their images are given in Figure 3. In the analysis, it was determined that the SiO_2 ratio was higher in morphological crystals with large grains (Figure 3a and b). It was determined that small crystallite particles were collected on the large particles and that the small particles were dioptase and chrysocolla copper-silicate based particles. Average values of EDX analyzes taken from selected areas 1, 2, 3 and 4 areas in Figure 3 are given in Table 3. Likewise, SiO_2 decreased and CuO ratios increased in the EDX analyzes of the samples in which the turquoise color changed from dark to light. Crystal particles are not in micrometer size, but rather in nanometric size.

JSR A
Journal of Scientific Reports

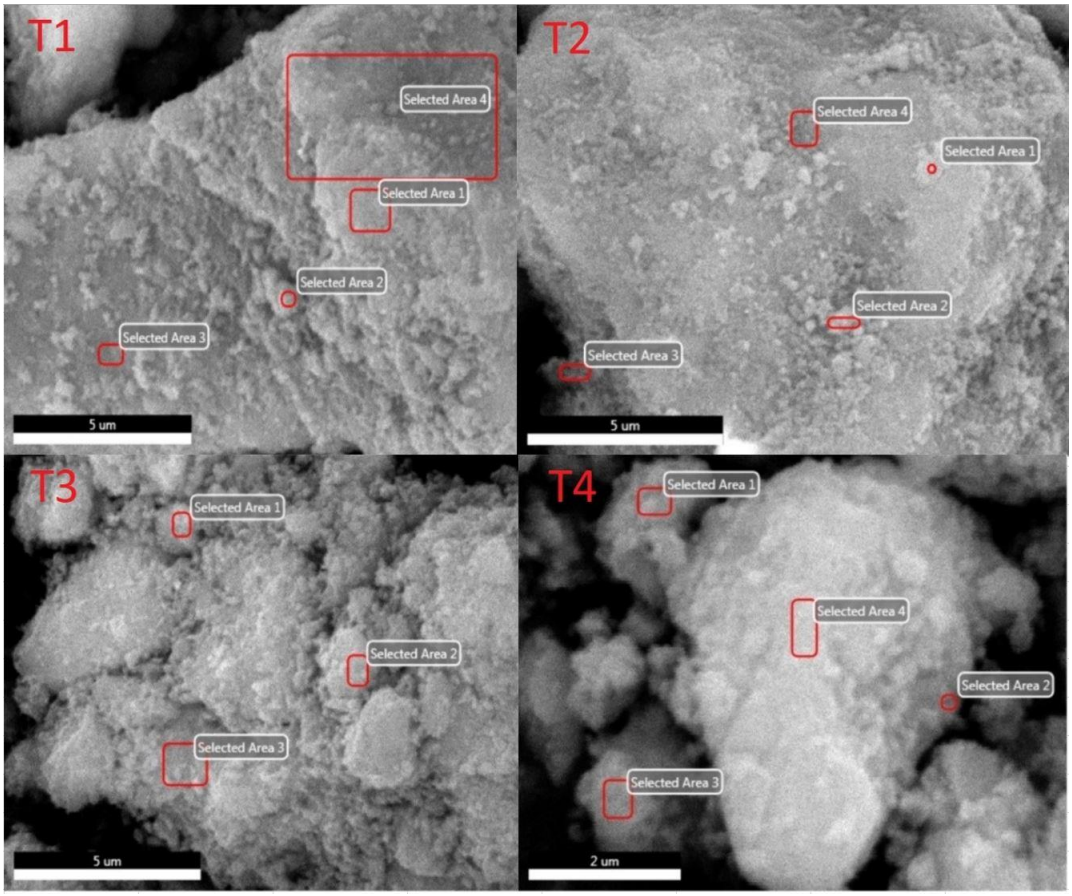

Figure 3. Microstructure images of samples in different colors

EDX analyzes from the surfaces of copper silicate minerals showed that SiO_2 was higher in dark colored minerals and CuO was higher in light colored minerals (Table 3). It was determined that the turquoise color would be more vivid with the increase in the CuO/SiO_2 ratio. Accordingly, the CuO/SiO_2 ratio of copper silicate minerals in the range of 1.4 to 2.7 is important in the visuality of the turquoise color. The chemical content of the samples obtained as a result of XRF analysis coincides with the data obtained as a result of EDX analysis.

Table 3. EDX analyzes of copper silicate minerals in four different colors.

Oxides	**T1 (%wt)**	**T2 (%wt)**	**T3 (%wt)**	**T4 (%wt)**
SiO_2	92.64	80.23	70.37	53.65
Fe_2O_3	2.31	-	-	-
CuO	6.04	19.78	29.63	46.35

4. CONCLUSION

The results obtained in the study can be listed as follows:

- ✓ Samples were separated by color and characterized.
- ✓ Turquoise colored copper silicate minerals are more vivid in color with increasing CuO and decreasing SiO_2 ratios. In addition, it was determined that the change of turquoise color from light to dark tones in turquoise pigments depends on CuO and SiO_2 changes.
- ✓ The crystal lattice parameters of the copper silicate mineral changed with the change of oxide ratios. With increasing CuO ratio, the lattice parameters were the highest at a-axis 22.705 Å, b-axis 21.310 Å and c-axis 16.993 Å.
- ✓ The crystallite sizes decreased with increasing CuO ratio and decreasing SiO_2 ratio. Turquoise color appearance has a more vivid appearance with decreasing crystallite size.
- ✓ The smallest crystallite size was determined as 171 Å in the most vivid turquoise colored copper silicate mineral. As the crystallite size decreased, the turquoise color appearance was visually better.
- ✓ The starting raw material used is not the copper silicate sample turquoise mineral. The samples contain predominantly SiO_2 and less dioptase and chrysocalla minerals. Because turquoise is a semi-precious stone, it is costly. Since copper silicate-based specimens are less costly to extract and process, they can be used to make ornamental stones or tiles.

ACKNOWLEDGMENT

We would like to thank the Kütahya Dumlupınar University Advanced Technologies Research Center (DPU-ILTEM) for SEM analysis.

REFERENCES

[1] Qiu, J.T., Qi, H. And Duan, J.L., (2017), Reflectance spectroscopy characteristics of Turquoise, Minerals, 7 (1), 3.

[2] Foord E. And Taggart Jr. J.E., (1998), A Reexamination of theTurquoiseGroup: the Mineral Aheylite, Planerite (redefined), Turquoise and Coeruleolactite, Mineralogical Magazine, 62(1), 93-111.

[3] Bernardino, N. D. E., Izumi, C. M. and de Faria, D. L., (2016), Fake turquoises investigated by Raman microscopy, Forensic science international, 262, 196-200.

[4] Dunn, P. J., and C. W., F.. (1976), Prosopıte, An effectıve turquoıse substıtute.

[5] Frost, R. L.; Xi, Y.F., (2013), Is chrysocolla $(Cu,Al)_2H_2Si_2O_5(OH)_4 \cdot nH_2O$ related to spertiniite $Cu(OH)_2$, Avibrational spectroscopic study. Vib. Spectrosc, 64, 33–38.

[6] Clark O. C., PooleJr. C. P., Farach H. A., (1979), Variable-temperatureElectron Spin Resonance of Turquoise, American Mineralogist, Volume 64, p.449-451.

[7] Crespo-Feo E., Garcia-Guinea J., Correcher V., Prado-Herrero P., (2010), Luminescence Behavior of Turquoise, RadiationMeasurements 45, 749-752.

[8] Huifen Z., Chuanyi L., Zhongwei M., Zhenguo Y., Enlin Z., (1984), Magnetic Properties, Characteristic Spectra and Colors of Turquoise, Geochemistry, 3, 4.

[9] Nassau, K., (2001), The physics and chemistry of color: the fiften causes of color, John Wiley & Sons, Inc. USA.

[10] Derin Coşkun , N. (2017). The development and thermoelectric efficiency depend on the temperature of P-type Ca3Co4O9 structure in energy conversion, Doktora Tezi, Kütahya Dumlupınar Üniversitesi Fen Bilimleri Enstitüsü, Kütahya, 244p.

Kütahya Dumlupınar University
Institute of Graduate Studies

Journal of Scientific
Reports-A
E-ISSN: 2687-6167
Number 48, March 2022

RESEARCH ARTICLE

PREPARATION of BLACK COLORANTS for STONEWARE GLAZES with USING Ni-Co COMPOSITE, CHROMITE and IRON OXIDE MIXTURES

Hale YILDIZAY [1*], Fikret AYDOĞDU[2]

[1]Kütahya Dumlupınar University, Kütahya Fine Arts Vocational School, Department of Tile Art and Design, hale.yildizay@dpu.edu.tr, ORCID: 0000-0002-3896-9912
[2]Kütahya Dumlupınar University, Kütahya Fine Arts Vocational School, Department of Tile Art and Design, fikret.aydogdu@dpu.edu.tr, ORCID:0000-0001-8514-0405

Received Date:09.03.2022 *Accepted Date:30.03.2022*

ABSTRACT

Black ceramic colorants were prepared from mixing Ni-Co composite, chromite and magnetite mineral as raw materials. The colorant mixture prepared for this purpose was added to stoneware ceramic glazes at 10%,15% and 20% respectively. The prepared colorant added glazes were ground in the jet mill for 15 minutes and sieves. Glazes applied to the stoneware bodies and then fired at 1200 °C in an industrial ceramic kiln. Color values of colorants and colored glazes were measured L*a*b* with a spectrophotometer device. It has been observed that this prepared colorant has similar properties with the color values of the black colorants used in the sector. As a result, it has been shown that the black colorant obtained can be used as a colorant in Stoneware glaze recipes without causing any problems or defects in the final product.

Keywords: *Stoneware, Glaze, Materials, Characterization, Colorant*

1. INTRODUCTION

Stoneware tableware has a wide range of uses today because it has a wide range of colored glazes and is durable. Pure metal oxides can be used in the production of stoneware glazes with different colors, as well as in colorants obtained by mixing raw materials containing appropriate elements in certain proportions and passing them through standard color preparation processes [1,2].

Black colorant is the most preferred color among the colorants used in ceramics. Black colorants have a use of approximately 25% in the ceramic industry [3]. The black color used in ceramics is obtained with two kinds of colorants. First, escolaite—hematite solids $(Cr, Fe)_2O_3$ and secondly, Fe—Cr—Ni—Co—Mn—(Cu—V) system complexes appear as spinel compositions. [4,5]. Eskolait—hematite colorants used in glazes for black color are less stable [6,7]. Therefore, black colorants used in ceramic glazes are mostly preferred in spinel structure [8, 9].

Pure oxides are used to obtain valuable elements such as iron, cobalt, chromium, magnesium, nickel and copper in the spinel structure of black colorants. This increases the final product cost considerably. While the first consideration in colorant production is the selection of suitable raw materials, current trends are towards alternative and cheaper raw materials. In the ceramic industry,

there are studies on the use of different raw materials and wastes to reduce the cost of black color production [10-16].
The aim of this study is to synthesize black color for stoneware ceramic glazes from relatively cheaper raw materials, to determine the color properties and to reveal possible interactions between colorant and stoneware glazes using various ratios of Ni-Co composite, chromite and magnetite mixtures.

2. EXPERIMENTAL METHOD

2.1. Raw Materials

In the production of colorants; Chromite mineral as chromium oxide source was provided from Hayri Ogelman mining company in Bursa Harmancik. Magnetite mineral as iron oxide source was provided from Ferromad mining company in Kütahya Hisarcık district. In addition, the Ni-Co composite, which guides the study differently; it was used as source of nickel and cobalt oxide and supplied as raw material from Meta Nickel Cobalt company in the Manisa Gördes.

Ni-Co composite is preferred in the study because it contains valuable elements for black color production such as high amounts of nickel, mangan and cobalt oxide. The Ni-Co composite used in the study is produced by acid dissolving (HPAL) method under high pressure, which is the state-of-the-art application of the most efficient hydrometallurgical acquisition method [17].

Stoneware glazes and their bodies used for colorant trials were obtained from Tulu porcelain company. The commercial black pigments CK13074 (Ferro Corporation), CP 30 (Itaca S.A.) used in stoneware ceramic coloring are chosen as a reference colorant in this study.

The samples of the raw materials used, was melted out in panalytical Wagon 2 model device and XRF (chemical analysis) was carried out on Panalytical brand Axios MAX model device (Table 1).

Table 1. Chemical composition of raw materials.

Oxides (%)	Chromite	Ni-Co composite	Magnetite
SiO_2	10.61	0.6	2.98
Al_2O_3	5.22	0.34	0.95
Fe_2O_3	20.57	0.3	89.93
CaO	0.23		1.51
MgO	20.64	3.91	3.91
Co_3O_4	-	3.97	-
CuO	-	0.34	-
Na_2O	-	0.07	-
TiO_2	0.14	-	0.03
Cr_2O_3	39.56	-	-
As_2O_3		-	0.43
V_2O_5		-	0.27
P_2O_5	-	-	0.09

ZnO	0.12	0.76	-
MnO	0.26	7.21	-
NiO	0.17	82.5	-
SO_3	0.02	-	0.11
L.O.I*	0.98	-	0.57

L.O.I*: Loss on ignition

2.2. Preparation of Black Colorants

For the study, black colorant synthesis was made mixing Ni-Co composite, magnetite, chromite and as raw materials. The colorant raw materials used in the study was subjected to wet milled and then dried. In the study, it was determined that 40% chromite, 40% magnetite and 20% Ni-Co composite mixtures.

3. RESULTS and DISCUSSION

3.1. Color Analysis

Black colorant made for this study, were added to the stoneware glazes proportions of 10%, 15 and 20% and mixed and homogenized for 15 minutes using alumina balls in the jet mill. The results obtained by adding 10%, 15%, 20% colorant to the stoneware glaze composition are given in Figure 1. Stoneware glaze is taken from Tulu Porcelain company.

The color characteristics of all stoneware glazes were measured. Color measurements of colorants in stoneware glaze were made with Konica Minolta–Spectrophotometer CM-700d device. The results obtained are shown in Table 2 as L* a * b* parameters. Table 2 is included commercial black pigment of stoneware glaze, Ferro CK13074, for compare colorants.

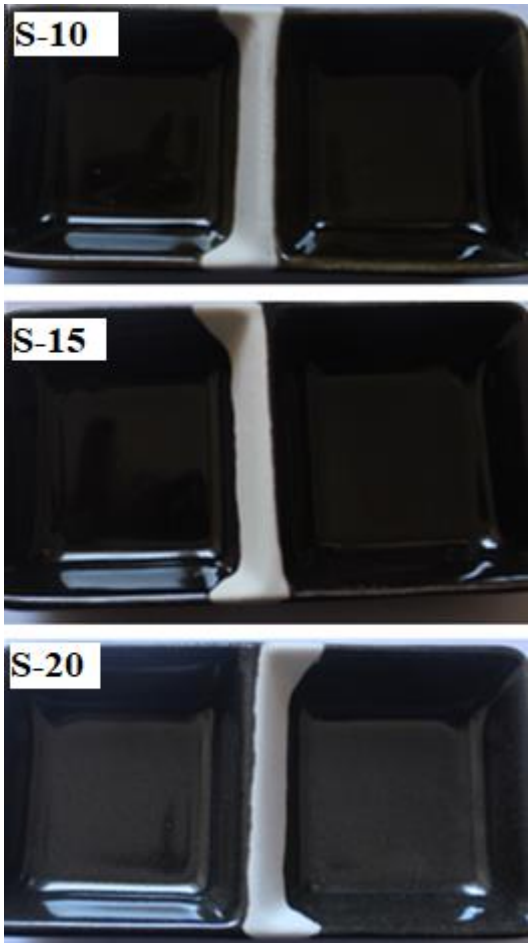

Figure 1. Color effects of 10%, 15% and 20% non-calcinated colorants addition on stoneware glaze, respectively

The results obtained are shown in Table 2 as L* a * b* parameters. Based on the L*, a*, b* values of commercial black pigments, it is seen in Table 2 that the black colorant in stoneware glazes to be produced must have L*<30, a* <1, b* <1 values.

In the Table 2. L a, b values of black colorants in stoneware glazes were measured. It can be seen from the images at the Figure 1, (S-20) that the color turns gray with the addition of 20% colorant in stoneware glaze and the L value increases from (28.18) to (31.54) towards white. The appearance of black color in 15% colorant addition was determined visually and with L,a,b values. Therefore, it is thought that 15% mixture is sufficient. Since it is thought that the use of excess colorants will lead to a cost increase, in the study were continued with the addition of 15% colorant.

Table 2. L a, b values of black colorants in stoneware glazes.

Colorants in stoneware glaze	**L**	**a**	**b**
Ferro-CK13074	29.9	0.11	-0.23
S-10	28.03	0.11	2.39
S-15	28.18	0.46	0.25
S-20	31.54	0.09	0.82

In the Figure 2, there are images of the pressed samples of black colorant powders that were not heat treated (without calcination), calcined at 1100 and 1200 ºC. L a, b values of black colorant, colorants calcined at 1100°C and 1200°C are given in Table 3.

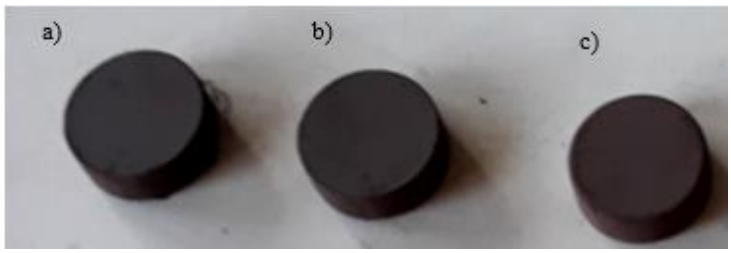

Figure 2. Pressed form of the prepared black colorant powders a) colorant (non-calcinated) b) Colorant calcined at 1100 ˚C for 1 hour c) colorant calcined at 1200 ˚C for 1 hour.

The colorant used in this study was calcined in the electric kiln for 1 hour at a temperature of 1100 ºC and 1200ºC respectively. Porcelain crucibles were used for the calcination process and wet grinding was applied again to the colorants that solidified after calcination. The colorants were sieved and dried.

The colorant was stabilized by applying heat treatment (calcination) to the colorant, which has a certain chemical composition and crystal structure. When heat is applied, the materials used in the formation of colorants react with each other, forming new chemical compounds and structures. Sometimes the resulting unstable color table is due to the inability to adequately complete of the reactions required for color formation. This instability is completed by the calcination process.

Table 3. L a, b values of Ferro-CK13074, produced black colorant and black colorants calcined at 1100°C and 1200°C .

Colorants	**L**	**a**	**b**
Ferro-CK13074	25.54	-2.75	-4.85
Produced black colorant	28.58	2.05	3.99
Calcinated black colorant 1 hour at 1100°C	29.39	2.13	1.73
Calcinated black colorant 1 hour at 1200°C	24.18	0.63	-0.80

The viscosity of the glazes was determined with using the ford cup viscometer. The viscosity of the prepared glazes is set to 15 sec and litre weights to 1450 g/l. These glazes were then applied on the ceramic bodies by dipping method and fired in the industrial kiln at 1200 ºC. Figure 3 shows the calcinated colorants applied to stoneware glazes and their effect on the bodies and L,a,b values are given in Table 4.

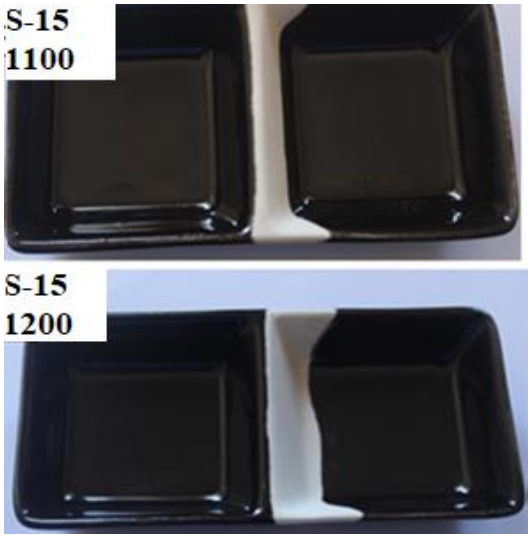

Figure 3. Color effect of the calcined colorants at 1100 ºC and 1200 ºC on the stoneware ceramic glaze respectively.

Table 4. L,a,b values of stoneware ceramic glazes containing Ferro- CK13074 pigment, black colorants calcined at 1100 ºC and 1200 ºC.

	L	**a**	**b**
Ferro-CK13074	29.90	0.11	-0.23
S-15 (calcinated 1100 ºC)	26.71	0.61	-0.24
S-15 (calcinated 1200 ºC)	25.94	0.59	0.45

The whiteness value of L was measured as (29.90) in stoneware glazes using commercial black pigments. This whiteness value was measured as (26.71) and (25.94) respectively, by using black colorants calcined at 1100°C and 1200°C in stoneware glazes. The L* value of the black colorants produced by the calcination process decreased compared to the commercial black pigments. This shows us the success of the colorants obtained as a result.

3.2. Microstructure Analysis

The microstructure analysis resulting use of in the glaze the produced colorants was determined with the FEI NANO SEM 650. EDS analysis was performed with the EDAX-EDS device connected to a scanning electron microscope. In the S-15-1100 glaze the occurring crystals and the microstructural appearance are given in Figure 4. In the Figure 5. EDS analysis of crystals in S-15-1100 glaze.

Microstructural appearance of the distribution of S-15 (calcinated 1100 ºC) crystals in stoneware glaze are given in Figure 4a and b. In the microstructure images have detected crystals similar to pine leaf. Image of pine leaf shaped of crystal and EDS analysis of crystal is given in Figure 5 and an average oxide composition of the crystals according to EDS in Table 5.

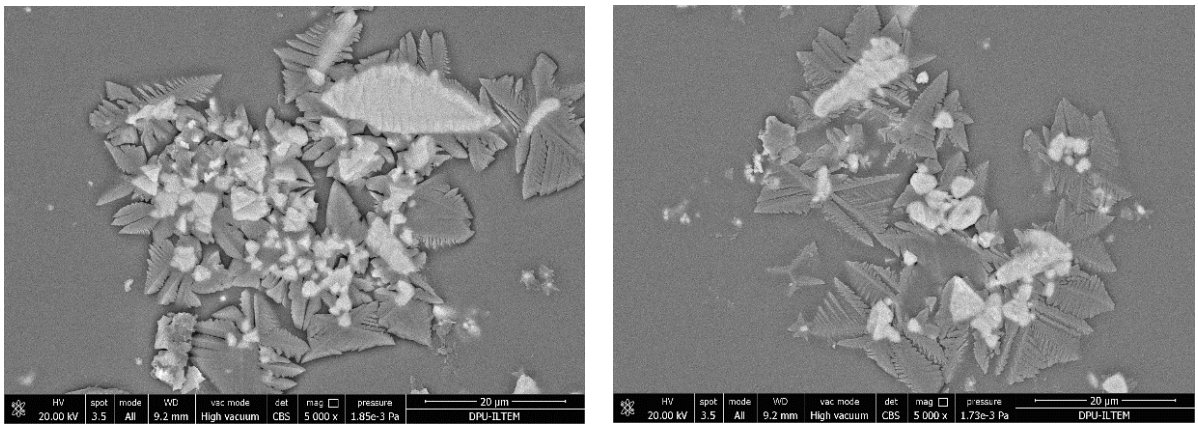

(a) **(b)**

Figure 4. SEM microstructure image and distribution of crystals in stoneware ceramic glaze of S-15-1100. (5000X magnification).

S-15 EDS patterns taken from the glaze crystals of the colorant calcined at 1100 ºC, Fe, Cr, Ni, Co amounts on the glaze surface.

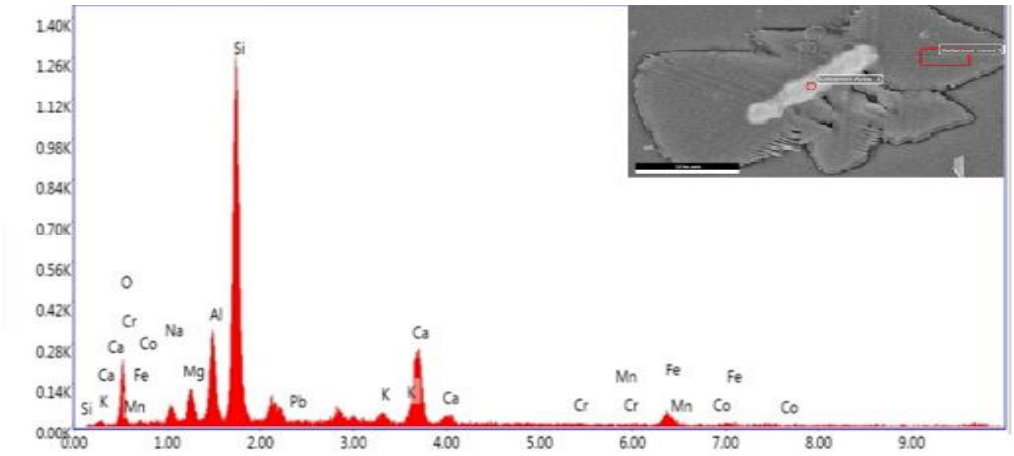

Figure 5. EDS analysis of S-15 (calcinated 1100 ºC) crystals in stoneware glaze at 8000X (Fe, B, Na, Cr, Ni, Si and Mn quantities on the glaze surface).

Table 5. Average oxide composition of the crystals according to EDS in Figure 5.

Element	Weight (%)
B_2O_3	17.42
Na_2O	5.02
MgO	0.61
Al_2O_3	1.61
SiO_2	38.61
K_2O	0.51
CaO	6.34
Cr_2O_3	5.74
MnO	0.66
Fe_2O_3	10.56
NiO	12.91

Microstructural appearance of the distribution of S-15 (calcinated 1200 ºC) crystals in stoneware glaze are given in Figure 6a. In the microstructure images have detected crystals similar to pine leaf. Image of pine leaf shaped of crystal in Figure 6a and 6b. EDS analysis of crystals in glaze is given in Figure 7.

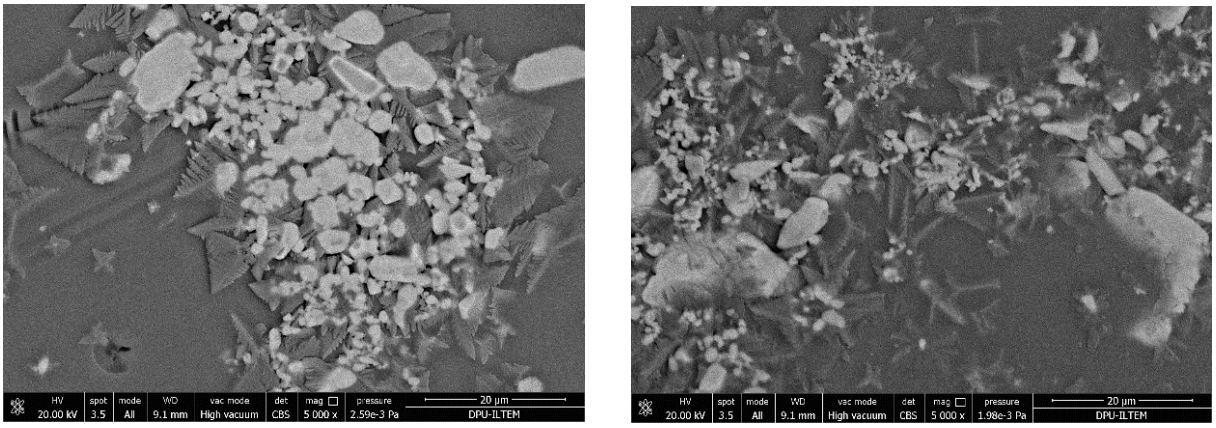

(a) **(b)**

Figure 6. SEM microstructure image and distribution of crystals in stoneware ceramic glaze of S-15-1200. (5000X magnification).

JSR A
Journal of Scientific Reports

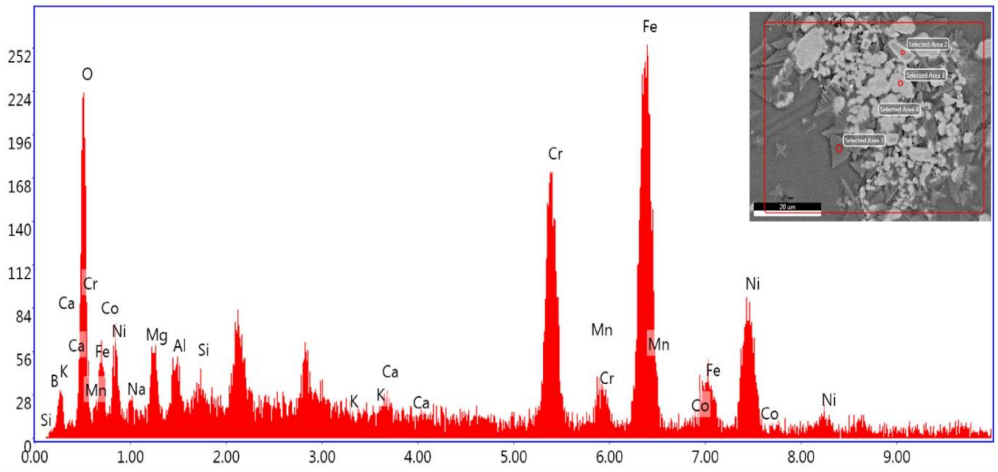

Figure 7. EDS analysis of S-15 (calcinated 1200 ºC) crystals in stoneware glaze at 8000X (Fe, B, Na, Cr, Ni, Co, Si and Mn quantities on the glaze surface).

Table 6. Average oxide composition of the crystals according to EDS in Figure 7.

Element	Weight (%)
B_2O_3	6.99
Na_2O	0.16
MgO	1.04
Al_2O_3	1.04
SiO_2	1.55
K_2O	0.28
CaO	1.04
Cr_2O_3	41.88
MnO	1.53
Fe_2O_3	28.42
CoO	1.34
NiO	14.72

4. DISCUSSION

As a result of this study, it has been determined that using industrial products such as a mixture of Ni-Co composite, magnetite and chromite as a colorant in glazes in which black tones are used in the production of ceramic stoneware glazes, stoneware glazes can be produced without deteriorating their properties and it will contribute economically. The improvement of black tones when the colorant is subjected to heat treatment at different temperatures (1100℃- 1200℃), has created an advantage in the use of this mixture as black color. The obtained colorant and calcination applied to this colorant positively affected the color parameters in the glaze compositions where the colorants were used. The color parameters similar to commercial black pigments were found. The colorants added to the glazes

covered the body surface perfectly. As seen in the SEM-EDX results; the presence of chromium, iron, nickel and cobalt oxide ensured the acquisition of very good black tones in stoneware glazes.

ACKNOWLEGMENTS
This study was financially supported by Kutahya Dumlupinar University Scientific Research Projects Co-operative Center with project no. 2017 – 69. We would like to thank our Scientific Research Projects Co-operator Ship Center, which provided financial support to the project.

REFERENCES

[1] Arcasoy, A., (1983)., Seramik Teknolojisi. M.Ü.G.S.F. Seramik İstanbul., ASD Yay., No:2, 13-14.

[2] Yıldızay H., Taşçı E., (2019). Lateritik Nikel Cevherinden Elde Edilen Nikel-Kobalt Oksit Kompozitinin Stoneware Sırındaki Renk Etkileri. Akü Femübid, Özel Sayı (204-211).

[3] Costa, G., Della, V.P., Ribeiro, M.J., Oliveria, A.P.N., Monros, G., and Labrincha, J.A. (2008). Synthesis of black ceramic pigments from secondary raw materials. Dyes and Pigments, Vol.77, pp.137–144.

[4] Escribano, P., Carda, J.B., Cordoncillo, E., (2001). Esmaltes y pigmentos cerámicos, Faenza Editrice Iberica, Castellon,

[5] Italian Ceramic Society, (2003). Colour, Pigments and Colouring in Ceramics, SALA, Modena,

[6] Eppler, R.A., (1987). Selecting ceramic pigments. Am. Ceram. Soc. Bull. 66 1600-1604.

[7] Ozel, E., and Turan, S., (2003), Production and characterisation of iron-chromium pigments and their interactions with transparent glazes. J. Eur. Ceram. Soc. 23, 2097–2104.

[8] Eppler, R.A., (1998). "Colorants for Ceramics"; pp. 877–92 in Encyclopedia of Chemical Technology, Vol. 8, Edited by R.E. Kirk, and D.F. Othmer. Wiley, New York,

[9] Maslennikova, G.N., (2001). Pigments of the spinel type, Glass Ceram. 58 5-6.

[10] Tanisan, B., and Turan, S. (2011). Black ceramic pigments for porcelain tile bodies produced with chromite ores and iron oxide waste. Journal of Ceramic Processing Research, Vol.12, 462-467.

[11] Tanisan, B., and Turan, S. (2012). Synthesis of Fe-Mn black pigments by using hematite waste and manganese ore mixtures. Trans. Indian Ceram. Soc. Vol.71(1),17-22.

[12] Ozel, E., Turan, S., Çoruh S., and Ergun, O.N., (2006). Production of brown and black pigments by using flotation waste from copper slag. Waste Manage. Res., Vol. 24, pp.125–133.

[13] Costa, G., Della, V.P., Ribeiro, M.J., and Labrincha, J.A., (2008). Forming black spinel pigment from industrial sludge. Am. Ceram. Soc. Bull., Vol.87, No.7, 9101–9107.

[14] Yang, Y.G., Xu, J.H., Cai, B., Wang, Q.C., Xiu, D.P., Zhao, Z.B., Sun, Q. Z., and Cao, S. L. (2013). Synthesis and applications of black ceramic from recycled industrial wastes. Advances in Applied Ceramics, 112, 146-148.

[15] Ozturk, Z.B., Dal, S. (2022). "Characterization of industrial ceramic glazes containing chromite processing waste: Experimental factorial design effects on color parameters", Materials Chemistry and Physics, 282, 125928.

[16] Ozturk, Z.B., Ay, N., (2010). "The effect of ferrochromium fly ash as a pigment on wall tile glaze", Advances in Science and Technology, 88,213-218.

[17] http://www.metanikel.com.tr /mhp-uretiyoruz

Kütahya Dumlupınar University
Institute of Graduate Studies

Journal of Scientific
Reports-A
E-ISSN: 2687-6167
Number 48, March 2022

REVIEW ARTICLE

COMPUTER-AIDED DESIGN and VIRTUAL REALITY in ARCHITECTURE

Hacer MUTLU DANACI[1], Arzu ÇAKMAK[2*]

[1]Akdeniz University, Faculty of Sciences, Department of Architecture, hacermutlu@gmail.com, ORCID: 0000-0002-7325-6168
[2]Akdeniz University, Faculty of Sciences, Department of Architecture, cakmakarzu@gmail.com, ORCID: 0000-0002-4634-5923

Received Date:22.07.2021 *Accepted Date:03.01.2022*

ABSTRACT

The constant development of technology has resulted in virtual reality being included in almost every aspect of our lives. Today, the opportunities offered by technology have made many conventional methods redundant, which is especially the case in the field of architecture. The sophistication of software and hardware customised for architecture means that computer literacy and keeping a close eye on technological progress has become a prerequisite for actors in the profession. The undeniable role of computer skills in professional development also presents itself in academic environments. Virtual reality is now integrated into all areas of education while the share of computer-aided design in architecture is growing steadily. These developments bring on the need to introduce different perspectives in architectural education. Computers have made it possible for students to transform abstract thoughts in their designs into concrete data much more quickly and easily with the assistance of custom hardware and software. This study aims to bring a different perspective to architectural education by explaining how virtual reality can be employed in computer-aided designs in architectural education and the new potentials it offers. In this context, the situations created by the processes before and after the use of technology in architecture were examined in detail. As a result of the examinations, it is understood that it is necessary to follow and use the developing technology in architecture, but it should also be used in the traditional method.

Keywords: *Virtual Reality, Architecture, Architectural Education, Design, Computer*

1. INTRODUCTION

A retrospective examination confirms the continuous change and evolution of technology. The introduction of machines in our lives, especially in the post- industrial revolution period, has led to great changes in the field of architecture. During this process, in which the use of computers increased exponentially, architectural designs have rapidly migrated to digital platforms while many basic components such as the design process have gone through significant changes.

Information technologies have been used for the purpose of architectural education for more than 20 years. The use of digital design methods is on the rise around the world and in Turkey. Information technologies have been adopted by architecture schools in Turkey parallel to the rest of the world. The use of such technology has accelerated as greater numbers of academicians and architecture students

have got accustomed to using computers [1]. The development of architectural design software has also meant that these applications now have an important place in the field of education. Learning these programs during education also give students an advantage in their professional lives [2].

Currently, a combination of conventional methods and digital technologies is used in architectural education. Conventional methods in architectural education, which rely on paper, pencil and models, are still used extensively. Digital technologies are used as complimentary instruments to the former. However, this can be considered as a transition phase to digital technologies [3]. Architectural education programmes start with the conventional method and then move on to two-dimensional drawing with digital software before progressing to visualisations with three-dimensional models. Computers should be considered as a tool that provides architecture students the opportunity to experience different aspects of their designs. While conventional methods allow architecture students to get hands-on experience with tangible objects, computer programmes make it easier to access processes and resources related to design [2-4].

Computer technologies in architectural education originally started with two-dimensional drawings using CAD applications. Today, it is used for basic designs in applied projects. However, with the introduction of three-dimensional modelling techniques around the mid-1980s, the focus shifted towards visual expression [2-5]. Computer software helps designers evaluate spatial relations and develop their designs [6].

Visual communication improves dialogue between professionals and the general public, increases understanding and improves decisions, which explains why it has become an increasingly common practice in environmental decision making [7]. We perceive the world three-dimensionally, so there is a growing need for three-dimensional images generated by computers or similar implements [8].

In the face of technological progress, the development of societies relies on keeping up with changes and adopting new technology into their lives. To do so, modern societies carry out studies on the use and development of new techniques and methods in the field of academic teaching and learning. Known methods and techniques in education gradually become inadequate and even invalid as technology develops. As one of the many innovations introduced with new technology, virtual reality has brought a new perspective to education and training methods [9]. "It is claimed that the virtual educational environment model is an important tool for architectural education to adapt to current technological developments and ideational changes" [10].

The introduction of computer technologies in the field of architecture has also brought a new perspective to design. Computers have made it possible to realise design forms that would be considered difficult or uncalculatable with conventional methods. Architectural design has also evolved with the technology-based development of previously limited materials and construction methods. Collectively, these changes and developments have led to the emergence of a new design concept.

Considering the very broad topics of technology and virtual reality, this study has been limited to the investigation of computer-aided design processes in architecture and the introduction of virtual reality in architectural designs. The aim of the study is to identify the contributions of computer-aided design to architectural education.

JSR A
Journal of Scientific Reports

2. MATERIAL and METHOD

Conventional methods are quickly being replaced by computer technologies in architectural education. It is very likely that conventional methods will be abandoned completely in the near future. This study will first provide a brief overview of the evolution of architectural design education; second, evaluate changing phenomena and concepts in design following the introduction of computer-aided designs; and third make predictions on the future of architectural design. Subsequently, the existing academic system will be evaluated in conjunction with vocational experience before making forecasts about the nature of the education system in the future.

In order to make it easier to understand the place of virtual reality in computer-aided design in architectural education, the method of the study has focused on addressing the historical evolution from the origins of architectural design, especially the point where the concept of computer-aided design became adopted into the design process in the form of a literature review based on publications, theses and articles. In this context, changes in architectural designs were examined before, when and after computer technologies were included in this process. The positive and negative effects of each new method introduced to design education in architecture have been examined and evaluated periodically in terms of students, academicians, architects and customers. The data and experiences acquired during this research have been presented in the conclusion in order to shed light on future architectural education and training.

3. THE HISTORIC DEVELOPMENT ARCHITECTURAL EDUCATION and DESIGN

Architecture is structurally complex, contradictory and intertwined with abstract concepts. Architecture involves tangible elements such as material, structure, building; quantifiable elements such as mechanics, static and topography; as well as unpredictable factors such as nature, experience, existence, and human beings. According to Cook (1996), these quantifiable and unquantifiable factors are both the most enjoyable and most daunting aspect of architecture [11]. The numerous, constantly evolving variables of architecture have forced changes in architectural design education. Design education is based on lectures and conventional teaching. It also aims to build on student creativity and provide the knowledge which allows non-verbal expression as the source of actions based on capabilities [12-13]. Design studios and basic design courses complement students' aesthetic and artistic talents by building on their sensory, perceptual, critical, mental and visual aspects. Certain courses such as concepts, theory, and design knowledge aim to improve the design theory foundations of students. Courses like technical drawing, structural knowledge, and narrative techniques, support the expressive style and technical design knowledge [13].

Architecture requires making designs that consider predictions about the future. Thus, approaches to design must be based on an inquisitive perspective rather than stereotyping. The most important transformation in architectural education is introducing architecture students a perspective that embraces change. The architectural education system must be open to new methods [11]. Unquestioned knowledge hinders imagination. This is why, conventional rote education must be avoided at schools. There is a need to provide environments that give students hands-on experience; a setting where they can question freely, learn from practice and even from mistakes [14]. Unlike many other degrees, architectural education is based on learning by practice and gaining experience [13-15]. The studio tradition in architectural education provides students with the main design experience and can be regarded as the core of the education programme. Architecture must keep a close eye on the

JSR A
Journal of Scientific Reports

changes and developments of the time. Architectural education and design studio curricula must keep up with the changes taking place in the world. Design studios have constantly evolved from the past to the present and will continue to do so. Historically, architecture education and studios can be examined in three periods [13-16]. In the first period there was no structured architectural education, design education or studios. During this period, knowledge was transferred in context of a master-apprentice relation. An apprentice would learn architecture by observing and helping his master at work [17]. The unconditional superiority of the master was emphasised [13]. The master-apprentice relation continued into the second period of architectural education however, the theoretical aspect of education was provided in a school setting while the applied side took place in offices [17]. The beginning of the second period corresponds to the establishment of the French School, the first independent architectural school, which was followed by a turning point which saw the discipline of architecture breaking away from the traditional architectural education practice. The second period triggered a new era in architectural education. In the third period the Ecole des Beaux-Arts education system was adopted which led to the integration of practical work in the academic curriculum and the studio concept being an integral part of architectural education. This is also when the first studio system was implemented [15-18]. During this period, students also experienced an intensive design process, investigating problems with their peers and instructors [19]. Bauhaus brought another perspective in this period. In contrast to the Beaux-Arts model, the Bauhaus system focused on freeing students from conditionings, allowing them to expresses creativity and imagination individually [18]. Although the Beaux-Arts model had existed in architectural education for a long time, its prominence was weakened with the emergence of the modernist movement. Architectural education was influenced by Bauhaus throughout the first half of the 20th century and the number of design schools increased [13]. In the master-apprenticeship method, the master simultaneously transferred all his theoretical design and application knowledge to the apprentice. However, this system became

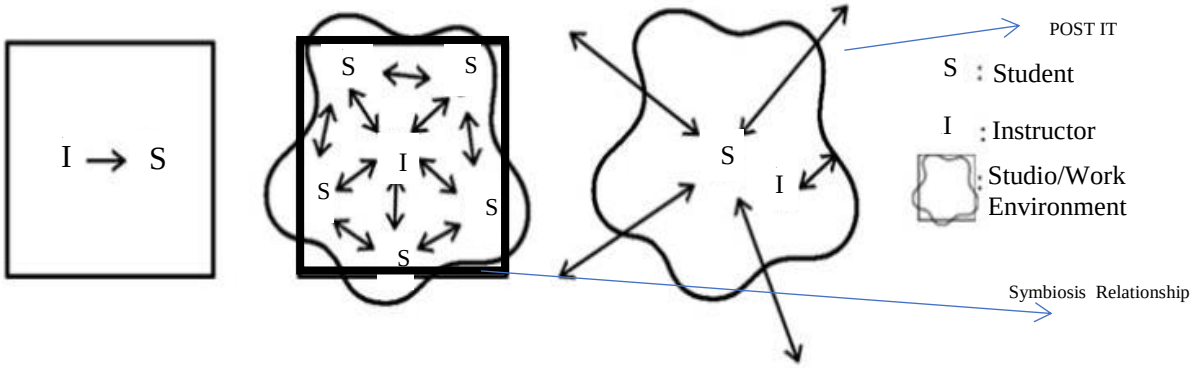

inadequate as demand for architectural solutions increased. Academies started to provide theoretical education. The applied part of the education continued in architecture offices outside the school [17].

As shown in Figure 1, considering the evolution of the approach to architectural education and its modern version practiced today, design in architectural education can be examined in three different ways. The first is the approach dominated by the master-apprentice relation. This approach is instructor-centred and information transfer is one-way, from instructor to student. This method does not allow students to ask questions and the instructor's knowledge is undisputed. The environment, the problem and the finished product are completely physical in this approach. The second approach is the empathic student-teacher relation. There are more students and the transfer of information is two-ways. This method practiced in design studios. The studio and problem are physical. The student

develops the design problem in the studio and works with the contributions of fellow students and instructors. During this process students learn design education. The student has more say in this method compared to the master-apprentice relation. The third is the post-IT approach. In this method, the architecture studio puts the student in the centre. Students can interact with peers in another studio through electronic communication. The virtual network provided by computer technology makes it possible for students to collaborate with users from all over the world. In addition to physical problems, hybrid and virtual problems are in the forefront and emerge as the subject of the architectural design studio. The virtual environment has also altered the limitations on accessing information. In this context, schools should follow developments and constantly revise curricula in order to keep up-to-date and provide a sound education [17]. In an age where designs concepts are changing constantly, it is extremely important to effectively benefit from new media and technologies to ensure the continuation of a design discipline [20].

4. COMPUTER AIDED DESIGN and VIRTUAL REALITY in ARCHITECTURE

The first computer drawing was made in the 1960's. This was also when designers were introduced to computer technologies. The hardware and software made available by technological progress has meant that computers have become important auxiliary tools in architecture. Computers are mostly used to present the stages of architecture and interior architecture. Such presentations often use a large number of computer-generated perspective images and animations based on the designs. The use of hand-drawn perspective sketches is now mostly limited to traditional presentations. Today, images from different angles of the modelled image are used in the presentations [21].

Today, technology makes it possible to reflect everything that can be physically perceived in a different medium. Real environments can be created with three-dimensional imaging and simulation techniques [21]. As shown in Figure 2, the virtual space designed with computer-aided design systems is first drawn in two dimensions before a three-dimensional model is created. It is a process that requires simultaneously considering two and three dimensions. In some software, the space is initially drawn in two dimensions after which it progresses to three dimensions. Some software creates two and three dimensions simultaneously.

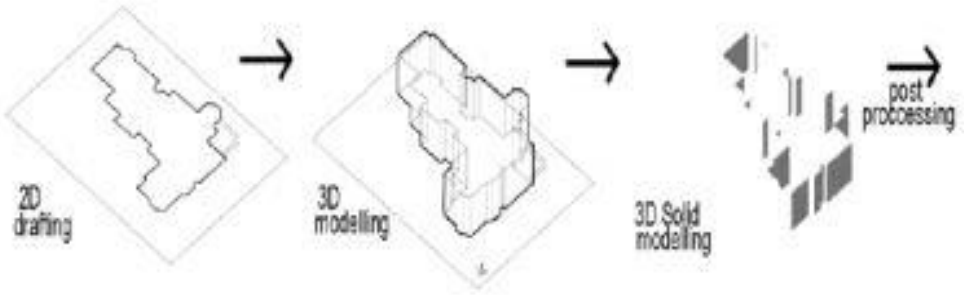

Figure 2. Visualisation of architectural design in CAD software [22].

As shown in Figure 3, models based on computer-aided designs can deliver the appearance of a real image with the help of other software. Material and lighting are assigned to the model in the last stage. These settings are the most important details that make the model give the impression of a real image.

Life-like images can be created by superimposing the model with a particular environment using template objects or created objects.

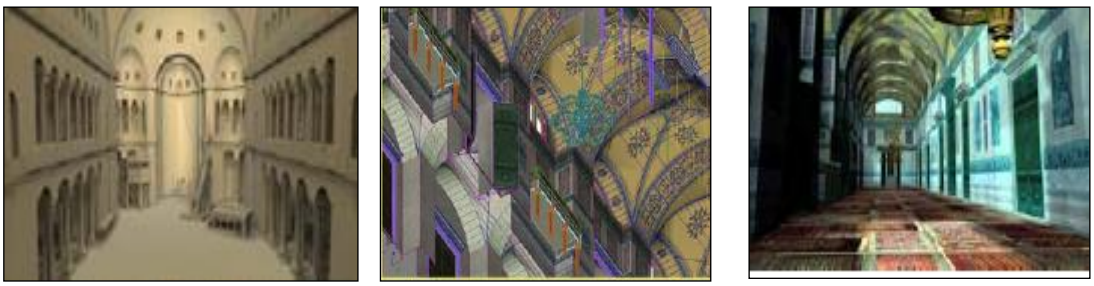

(a)modelling (b) material (c) lighting

Figure 3. Visualisation of the Ayasofya Model [23].

Virtual environments created with three-dimensional models can be used for virtual reality simulations. This allows the user to move freely inside the model. Stimulating our audio-visual senses, it is possible to create spaces that can be experienced and interacted. Virtual spaces can become spaces that can be experienced with multiple senses [23]. Users can move around within the simulated models. The nature of mutual interaction comforts the users [21].

Figure 4. A Virtual Reality Museum [23].

Architecture is the visual realisation of human imagination. These ideas are functionally made real with computer technology. Following the emergence of the "immateriality" concept, the foundation has been laid for merging the relation between the physical material dependence of architecture and computer technologies. Immateriality is replacing the physical material required for architecture with images and interactions provided by computer technology [24].

According to Anders (1999) all architectural projects in the future will be designed virtually. Cybrid is the physical and cyberspace community. Cybrid can involve virtual additions to real buildings or real spaces incorporated in cyberspace [25]. It appears that the future will be about cybrid (hybrid) designs using a combination of immateriality, physical space and virtual spaces [21].

"Virtual Reality can be defined as computer-generated 3D simulations in which users can physically interact with virtual environments and objects by means of custom electronic equipment such as headsets equipped with screens and various sensors, gloves and remote controllers. The most important feature of these simulations is that it creates real feeling of being there. This is made possible by interaction with immersive images that stimulate audio-visual senses, as well as giving users the ability to interact with virtual formations using various physical movements" [10].

According to Franck (2002), the concept of virtuality is not the opposite of reality, it is rather one of the layers of reality. Franck argued that the concept of virtual is real and refers to the intangible. Franck claimed that virtuality is "the ability of revealing the essence of something that actually exists inherently - that is, without transforming it into an object" [26]. The author noted that virtual architecture is "real and potential architecture and finds application in the digital world's laboratory and sheltered living spaces. Architects are also cyber architects" [26-27]. Önder believes that designers of virtual spaces do not have artificial intelligence, and that they may be dreams based on people's experiences. This is why the author thinks that images of the physical world will find a place in a virtual space setup [28]. Önder states that virtual spaces actually create images of the real world. In virtual architecture, real events, time and space are presented with the help of digital technologies, whereas traditional architecture relies more on fixed forms and precise geometries [17].

Virtual education applications of universities in the fields of architecture are very diverse. Özlem Ünkap (2006) examined virtual reality applications applied with different methods in architectural design studios. Studio studies have been made in cyberspace where the object is a physical or physical concept. In his other study, studies in which the entire environment of the design is cyberspace and the object is virtual were examined. In another study, workshops using cyberspace as a tool were examined. As a result of all these studies, it has been observed that a person can participate in the design and application method in different disciplines. It has been observed that the design process feeds on itself and new creative opportunities are provided to the designer. The application area of virtual architecture is cyberspace. Cyberspace is a universe consisting of communication networks and computers and supported, in which global information is transformed into form [17].

Virtual reality technology allows architecture students to observe every stage of space design from a critical and different perspective. Proficiency in using virtual reality and effective time management are important. This technology might also improve student motivation for design. Students can create a social atmosphere and also bring different and new approaches to designs. Since virtual reality can be remotely accessed, physical locations are irrelevant. This technology has become extremely important for students to be able to acquire a more realistic perspective to their designs [29]. In a sense, virtual reality technology has made it easier to perceive. Thus, the solution to previously complex concepts has become easier. In this context, architecture students develop on their design motivation and creativity. In the course follow-up, students who were independent of place and time were seen to gain flexibility in design [21]. It would be positive to include virtual reality in architectural design environments as it develops 3D thinking, allows existence in the design process, and provides different perspectives [20].

JSR A
Journal of Scientific Reports

5. APPROACHES to DESIGN EDUCATION in CONTEMPORARY ARCHITECTURE

A finely designed product is no longer adequate in the current approach to architectural design. It is important to create a behaviour on how design can be done. In this context, questions such as "What is design education? How is it given and how should it be given?" are becoming increasingly important in design schools [18]. In this evolving process, the question of "How can we teach better?" has changed to "How do people learn" [13]. Regarding the design process, it is of great importance in terms of architectural design education that the student tries and fails the design during education and is actively involved in all stages of the process.

The biggest problem of students starting architectural education is to interpret and visualise the spatial relations of the products they create with the abstract sketches of their imagination. Students initially visualise these abstract sketches with tangible tools such as pencil, paper and model [30]. In architecture, all products designed from the equipment inside the building to the structural and urban scales should be defined with technical expressions and according to architectural standards. These expressive techniques are two-dimensional drawings. The technique of expressing design idea by drawing is regarded as the main method of visualisation since the Renaissance [31]. The perspective and models created facilitate the presentation and perception. This is why, it will be more effective to use conventional methods in the early stages of an architecture student's development when they lack concepts and cannot establish a relation with objects. It is thought that this will help create better design awareness.

In the traditional method, the student is seen to have a passive role limited to receiving information; an empty object that needs to be loaded with information. During some aspects of architectural education, students can become more involved, especially in applied courses and field studies. Occasions that activate the student can be diversified with hyper-media tools. Considering technological developments and the requirements of the age, hyper-media must take a leading role in abandoning passive practices that merely load students with information. Most of the problems related to architectural education can be solved with the help of computer technologies [14]. However, while it is necessary to expose students to these technological processes, it is equally important to rely on the conventional method in which abstract ideas are rendered tangible with touch and feel in the initial stages of design in architectural education.

Computers were first used to carry out analytical calculations in engineering designs. "Computer-aided design (CAD) began with the development of the SKETCHPAD system in 1962-1963 by Ivan E. Sutherland in the laboratory of the Massachusetts Institute of Technology (MIT)." With the help of light and pencil (ligh-pen), designers using SKETCHPAD were able to design directly on a screen for the first time. The system developed by T. E. Johnson in 1963 made three-dimensional modelling possible [32-21]. The CNC (Computerized Numerical Control) system was introduced in the late 1960s to use in the production of designed objects [33]. Due to economic constraints, computer-aided design was not used widely in architecture until the 1970s. In 1970, only 50 companies in the world were using CNC machines in the design and production of complex surfaces [33-34]. AUTOCAD 1.0 was launched in 1980, and software witnessed a rapid development, making it possible to make most of the drawings of conventional architecture. AUTOCAD R9 and Autoshade 1.0, allowing CAD versions, curved 3D visualisation, wiremesh technique, and shading, were released in 1987. The unbelievable software development between 1990 and 2000 was made computer modelling possible to common users. The first version of 3d studio max was released in 1990 and its use became widespread

in a short time. In 1991, the Adobe Photoshop suite was released bringing success in computers-aided visualisations. 1992 saw the release of the Form-Z programme which has been crucial in creating free curves in modelling [35]. Collectively, these developments demonstrate that there has been a shift in the concept of design which now relies significantly on computers. Computers became widespread in architectural offices in 2000 and CAD software was used for different stages of design. With the development of computer-aided design, computers are now used as the primary drawing tool in architectural design. Computers also serve different functions such as presentation, communication, quantification, simulation and engineering calculations [21].

With the help of computers, architectural design has abandoned the traditional paper, pen and model and embraced a new, digital medium. The digital age has shortened the time needed for the design processes and made it possible to collaborate and work simultaneously. The internet provides a global working environment and the opportunity to gather on a common ground. Creating a digital space that does not exist physically has enabled the building or object to be formed and experienced in three-dimensional space [36].

Studies carried out by Işık have revealed the importance of using architectural drawing software in architectural education. Students are aware effective use of architectural drawing programs will also be an advantage in their professional lives. However, although design software abilities are important in professional life and architectural education, students need to make hand-drawn sketches and improve their skills. In this context, it seems more appropriate for four-year undergraduate degrees in Turkey to start education with conventional methods [2].

6. DISCUSSION

It is important to evaluate the dimensions of a place in architectural designs, as is to select the assessment approach for design technique. Each architect employs different techniques in developing designs. However, the development and dissemination of computer-aided design techniques also offers new opportunities. Modelling the space in three dimensions considering space limitations and experiencing virtual tours quickens the decision-making process during the construction phase of the building. Virtual reality has been criticised by many circles based on concerns that VR disconnects humans from reality, that the experience is socially insufficient, and that architects are losing a battle against technologies. These expectations have not materialised yet. On the contrary, it is important to understand that computer technology has enabled architecture to establish new relations with different disciplines. In modern architecture, interdisciplinary interaction is inevitable in creating an environment that is in harmony with social, economic and technological forces [37].

The fact that current computer-aided architectural modelling and presentation techniques create realistic images has led to a perception that architecture is a virtual image. This technology is now used extensively by investment and real estate companies as a major marketing tool. For this reason, the current market expectations are more in favour of quickly completing a design that is visually appealing. Today's market has made the use of computer technology compulsory. Computer technology has emerged as a design method rather than being an auxiliary tool in the design process.

Providing visually stimulating three-dimensional objects in two-dimensional planes have largely removed tactile stimulation from the process. Pallasmaa expresses his concerns about computer technologies: Computers are often seen as a useful invention, as they liberate human thought and offer

efficient design possibilities. Computers create distance between the designer and the object. Whereas Designers have a tactile contact when they draw and model by hand. The imagined design is physically modeled. You can be inside and outside the object at the same time. Creative design is formed by physical and mental identification and empathy. Computers turn this design process into a visual manipulation [38-39].

As one of the leading theoreticians and important architects of our time, Steven Holl, creates his designs by drawing numerous sketches in the design process, and relies on the model-making technique for three-dimensional expression. Holl experiences the tactile properties of the materials that make up his designs, the use of light as a material, and the relation between design and place. The architect turns to computer technology in the final stage of the design. Conventional methods play an important role in Holl's design process [39].

As technology made a stronger presence in the field of architecture, digital programmes and software gained significance in architectural education mainly due to market conditions and the ease of tackling labour-intensive, difficult projects. In this respect, architectural education must be open to progressive design programmes and students should be informed about such developments [2].

Schoon (1992) and Moloney (2001) reported that creative architectural design solutions often come from students who repeatedly work on their sketches and who critically examine designs. Computers provide easy access to sketches stored on the system as well as a wide range of solutions which expands student interest in architectural drawing programs. It appears that the three-dimensional thinking abilities and model-making skills of students have increased with the growing use of three-dimensional drawing programmes [2]. However, the current tendency is to introduce computer aided design training after the student has acquired a theoretical foundation in architecture and gained a certain degree of experience in conventional architectural design methods.

Sketching is very important in the architectural design process. However, the computer is a very powerful tool, which is very effective in modeling sketches, making models, making fine calculations, realizing details, starting production and most importantly, expressing designs. In today's conditions, it becomes impossible to stay away from computer technology, which enables the design and implementation process to work together in a very short time, with minimum error and maximum efficiency [40]. With the development of computers as well as technology, architecture has begun to exist even before it is built [41]. . Leach stated that the success in architectural designs affects the dominance of the tools used. Thus, he stated that computers are the most powerful tool in designs [42]. In terms of design contribution, parametric designs using computers can be one of the most successful design methods. Parametric design is a computer aided (CAD) design method using parameters. In architectural designs where parametric design is used, environmental data such as density in human flow, wind intensity, and sea salinity can be defined as parameters used in the design process. These data cause the form, detail and structure of the design to change. Changing one parameter affects all parameters. Thus, designers will be able to easily identify the source of the problems, their relationship and interaction with other elements [43]. Although parametric designs are mostly used to create forms, they provide great convenience in giving the details of the building units during the application phase of the form. Thus, interdisciplinary work will be facilitated and the construction process will be carried out with minimum error and important details [44]. It would be very wrong to prepare architecture students for the profession with only traditional methods in a time when designs are rapidly made with these methods.

Today, there is a clear shift from conventional design studios towards digital and open source design studios that rely on two- and three-dimensional expression techniques, electronic libraries, online video supported collaborations, and web archives. It is very likely that information technologies will contribute to a global common virtual design studio and joint project teams in an environment of intercultural interaction [17].

Considering the information provided, challengers of architectural education agree that architectural education should not be limited to studios and schools. The real world is a place of observation for architecture students that becomes a part of the environment in education [11].

7. CONCLISIONS

Research results suggest that computer technologies contribute significantly to the fields of architecture and interior architecture. Architecture does not rely on verbal expression, so it is crucial to present the created product before the application. In this context, many design problems can be solved efficiently with computer technologies. Computers make it possible to quickly and cheaply prepare presentations. It is easy to capture images and details from the relevant parts of the designs. Once created, these objects can be used in other designs, too. Users can virtually wander around the model for a full experience of the design. Computer-aided modelling is much easier than physical model-making. In addition, current computer technology creates very realistic images that feature different material options and lighting configurations to provide the user a realistic impression of the end result.

Advanced computer technology has found applications in various sectors. Students gaining professional experience in these sectors have also introduced technological developments to architectural education. In an age where time and efficiency are priorities, it is necessary to migrate from conventional methods to computer technology. Hand-drawing plans, sections, views and perspectives, calculations followed by model-making previously took days to complete using conventional methods but computers allow the simultaneous progress of all these aspects. A change made on a computer design will modify and/or correct all related drawings and plans, a problem that would require complete re-drawing in the conventional method as well as delays and additional costs.

Modern technology also makes it possible to use a combination of conventional methods and computer technology. Designers can also integrate different handmade components of the design with computers. At the same time, traditional methods can be used on computers. The best example is graphic tablets. Digital drawings can be made with the special pen that come with the tablets; stored on the system, changes in designs can be made when necessary. However, sometimes these methods can be misleading in designs. A product that is visually appealing in the model may not give the same result in real life. This is mainly associated with poor design awareness and the resulting inadequate use of technological means. In the initial stage, design awareness can be improved by touching and feeling after which, it could be developed with auxiliary tools. This is why it seems more feasible to practice traditional methods in the first years of architectural design education. Computer technologies could be more beneficial while still using some conventional methods in design.

Many of today's architectural designs are realized with virtual reality and parametric design methods due to the many advantages it provides. It is observed that its works related to this continue rapidly. In practice, it is very important to use tools that provide solutions with the least time, the most

economical way and the least error. For this reason, the use of technology in architectural designs becomes mandatory. The advancement of technology, which is constantly renewed and developed according to the needs, simultaneously affects the architectural design methods. These advances in architectural designs should be given to students who will become architects at the education stage.

The access to the endless opportunities offered by computer technology has affected all sectors including architecture. Architecture students should also be educated outside school settings. Students must follow global developments to provide critical and inquisitive thinking. This necessitates changes in the existing education systems. Traditional methods should be given at the beginning of architectural education. immediately afterwards, the most preferred methods in designs, where technology can be used, should be included in the training. Students should be introduced to virtual reality and parametric design methods during the architectural design education process. Designers design something that is known only vaguely. Designing the unknown based on predictions is only possible by questioning knowledge. Instead of being confined to current knowledge, transforming knowledge in line with the predictions will provide to a more accurate results in the making of an unknown design.

ACKNOWLEDGMENT

The authors thanks reviewers for their valuable comments and suggestions, which increased the clarity and the scope of the article.

REFERENCES

[1] Uzun, K. (2011, 2-4 Şubat). Mimarlık eğitiminde kullanılan dijital tasarım programlarının bellek ve tasarım sürecine katkıları. Akademik Bilim'11-XIII. Akademik Bilişim Konferansı Bildirileri, İnönü Üniversitesi, Ankara.

[2] Işık, Ö. B. (2017). Bilgisayar destekli tasarım programlarının mimarlık eitimine katkısı. Uluslararası Sosyal Araştırmalar Dergisi, 10(51), 778-784.

[3] Yıldırım, T., Yavuz, Ö.A. ve İnan, N. (2010). Mimari tasarım eğitiminde geleneksel ve dijital görselleştirme teknolojilerinin karşılaştırılması, Bilişim Teknlojileri Dergisi, 3(3), 17-26.

[4] Asanowicz, A. (1998). Approach the computer implementation in architecture curriculum, 16th ECAADE, Ecole d'Architecture de Paris Val de Marne, Paris, Frabsa, 4-8.

[5] Bilalis, N. (2000). Computer aided design cAD, INNOREGIO Project, 26.

[6] Ervin, S. and Hasbrouck, H. (2001). Landscape modelling digital techniques for landscape visualization, McGraw Hill Companies, U.S.A.

[7] Tiede, D. and Blaschke, T. (2005). A two-way workflow for integrating CAD, 3D visualization and spatial analysis in a GIS environment, Bringing CAD and GIS together: A workflow for integrating CAD, 3D visualization and spatial analysis in a GIS environment.

[8] Işık, Ö. B., Bayramoğlu, E.ve Demirel, Ö. (2013). Peyzaj mimarlığında modelleme çalışmalarının kullanıcılar üzerinde etkisinin araştırılması. Kastamonu Ünv., Orman Fakültesi Dergisi, 13(1), 15-23.

[9] Çavaş, B., Huyugüzel, P. ve Can, T. B. (2004). Eğitimde sanal gerçeklik. The Turkish Online Journal of Educational Technology, 3(4), 15.

[10] Yücel, V. (2018). Vric: Mimarlıkta yapı bilgisi öğreniminde kullanılabilecek bir sanal ortam önerisi, Yüksek Lisans Tezi, İstanbul Teknik Üniversitesi Fen Bilimleri Üniversitesi, İstanbul.

[11] Yürekli, İ., Yürekli H. (2004). Mimari tasarım eğitiminde enformellik. Mimarlık, planlama, tasarım itü dergisi/a, 3(1), 53-62.

[12] Hodgkin, Robin.A. (1985). Playing and Exploring: Education Through the Discovery of Order, Methuen, London, p. 146.

[13] Onur, D. Ve Zorlu, T. (2017). Tasarım stüdyolarında uygulanan eğitim metodları ve yaratıcılık ilişkisi, The Turkish Online Journal of Design, Art and Communication – TOJDAC, 7(4).

[14] Şahbaz, E. (2018). Mimarlık eğitiminde tarihi yapıların öğretilmesi için hiper ortam araçlarının algısal bir yöntem olarak kullanılması, Doktara Tezi, Karabük Üniversitesi Fen Bilimleri Enstitüsü, Karabük.

[15] Schön, Donald, A. (1985). The Design Studio. An Exploration of Its Traditions and Potentials, London: Rıba Publication Ltd. p.89.

[16] Uluoğlu, B. (1990). Mimari Tasarım Eğitimi:Tasarım Bilgisi Bağlamında Stüdyo Eleştirileri, Doktora Tezi, İTÜ, Fen Bilimleri Enstitüsü, İstanbul.

[17] Ünkap, Ö. (2006). Yüksek Lisans Tezi, Sanal mimarlık stüdyosu uygulamaları üzerine bir değerlendirme, İstanbul Teknik Üniversitesi Fen Bilimleri Enstitüsü, İstanbul.

[18] Arıdağ, L.ve Aslan, A. E. (2012). Tasarım Çalışmları-1 Stüdyosunda Uygulanan Yaratıcı Drama Etkinliklerinin Mimarlık Öğrencilerinin Yaratıcı Düşünce Becerilerinin Gelişimine Etkisi, Megaron, 7, 1, s.49-66.

[19] Tschimmel, K. (2010). Design as a Perception-in-Action Process, ICDC2010 International Conference on Design Creativity, Editor. Taura, T.; Nagai, Y, 223-230, Springer Verlag, London.

[20] Yıldan, İ. (2018). Mimari tasarım eğitiminde sarmal sanal gerçeklik ortamının mekansal ilişkilerin algısına etkisi, Yüksek Lisans Tezi, İstanbul Teknik Üniversitesi Fen Bilimleri Enstitüsü, İstanbul.

[21] Topçu, M. (2012). Bilgisayar teknolojilerinin mimari tasarım üzerindeki etkileri, Yüksek Lisans Tezi, Yakındoğu Üniversitesi, Lefkoşa.

[22] Yıldırım, T. (2004). Mimari Tasarımda Biçimlendirme Yaklaşımları ile Bilgisayar Yazılımları İlişkisi, Gazi Üniv. Müh. Mim. Fak. Der. Syf:67. Cilt 19, No 1, 59-71, 2004

[23] Özen, A. (2006). Mimari Sanal Gerçeklik Ortamlarında Algı Psikolojisi, G.Ü.

[24] Altın, A. (2005). İç Mekan Tasarımında Bilgisayar Teknolojilerinin Araç ve Malzeme olarak Kullanımı, Yüksek Lisans Tezi, E.A.Ü. Syf: 76, 77.

[25] Baykan, C. (2002). Mimarlık ve Sanallık. Arredomento Mimarlık, Çağdaş Mimarlık sorunları dizisi, Boyut yayıncılık. Syf:59.

[26] Franck, O. A. (2002). Düşünce İçin Mimarlık: Sanallığın Gerçekliği, Çağdaş Mimarlık Sorunları Dizisi: Mimarlık ve Sanallık içinde, s. 27-30, Boyut Yayıncılık, İstanbul.

[27] Koca, K, S. (2005). Çağdaş mimarlıkta yersizlik,Yüksek Lisans Tezi, İstanbul Teknik Üniversitesi Fen Bilimleri Enstitüsü, İstanbul.

[28] Önder, A. (2002). Siber Uzayda Mimarlık Sanal Dünyada Gerçek Mimarlar, Çağdaş Mimarlık Sorunları Dizisi: Mimarlık ve Sanallık içinde, s. 45-54, Boyut Yayıncılık, İstanbul.

[29] Şekerci, C. (2017). Sanal gerçekliğin iç mimarlık eğitimine etkisi, Yüksek Lisans Tezi, Hacettepe Üniversiteri Güzel Sanatlar Enstitüsü, Ankara.

[30] Ateş, G. (1999). Görsel etki analizinde simülasyonun kullanımı, Yüksek Lisans Tezi, Yıldız Teknik Üniversitesi, Fen Bilimleri Enstitüsü.

[31] Yıldırım, T., Yavuz, Ö.A. ve İnan, N. (2010). Mimari tasarım eğitiminde geleneksel ve dijital görselleştirme teknolojilerinin karşılaştırılması, Bilişim Teknlojileri Dergisi, 3(3), 17-26

[32] [32] Joe, R, Steadman, P. (1997). Principles of Computer-Aided Design, UCL pres in assocation with University, Syf:1, 2.

[33] Uslu, D. (2008). İç Mimarlık Tasarımlarının Sunum Aşamasında, El Çizimi ve Bilgisayar Destekli Çizimin Kullanımı, Yüksek Lisans Tezi, M.S.G.Ü, Syf: 107-111, 140, 149, 152- 154, 171.

[34] Çolakoğlu, B, Yazar, T. (2007). Mimarlık Eğitiminde Algoritma: Stüdyo Uygulamaları" Gazi Üniv. Müh. Mim. Fak. Der. Cilt 22, No 3, Syf: 380.

[35] Özen, A. (2006). Mimari Sanal Gerçeklik Ortamlarında Algı Psikolojisi, G.Ü.

[36] Toyran, T. (2008). İnsan Davranışlarının Sayısal Ortamda İncelenmesi ve Tasarım Sürecine Etkisi, Yüksek Lisans Tezi, Y.T.Ü, Syf:39.

[37] [37] Deviren, S. (2001). Mimaride Yer: Yapının Araziyle ilişkisinin kavramsallaştırılması, Doktora Tezi, İstanbul Teknik Üniversitesi Fen Bilimleri Üniversitesi, İstanbul.

[38] Pallasmaa, J. (2005). Tenin Gözleri, 2.Basım, 2014. (A. U. Kılıç, Çev.) İstanbul: YEM Yayın.

[39] Akkavak, K. K. (2017). Yüksek Lisans Tezi, Mekan Tasarımında Fenomenolojik Yaklaşımlar, Hacettepe Üniversitesi Güzel Sanatlar Enstitüsü, Ankara.

[40] Köksal, T.A. (2018). Sketchup herkes için 3 boyutlu tasarım.(3. Baskı). Pusula Yayınevi, Syf: 1-2.

[41] Sarıgül, A. İ. (2008). Yüksek Lisans Tezi, Mimarlıkta Gelecekçilik, Dokuz Eylül Üniversitesi, Fen Bilimleri Enstitüsü, İzmir.

[42] Leach N. (2009). Swarm Urbanism. Architectural Design, Vol 79, No 4.

[43] Baykara, M. (2011). Yüksek Lisans Tezi, Mimarlıkta Parametrik Tasarım ve Arazide Kütle Yerleşimi İçin Bir Model Önerisi , İstanbul Teknik Üniversitesi, Fen Bilimleri Enstitüsü, İstanbul.

[44] Kaçmaz, Ş. (2019). Parametrik Tasarım ve BIM . Yapı Bilgi Modelleme , 1 (1) , 3-9 . Retrieved from https://dergipark.org.tr/en/pub/ybm/issue/44342/477698